Electron Magnetic Circular Dichroism of Epitaxial Magnetic Thin Films at Nanoscale

A Thesis Submitted for the Degree of

Doctor of Philosophy

in the Faculty of Science

by

B. Loukya Chowdary

CHEMISTRY AND PHYSICS OF MATERIALS UNIT
INTERNATIONAL CENTRE FOR MATERIALS SCIENCE
JAWAHARLAL NEHRU CENTRE FOR ADVANCED SCIENTIFIC RESEARCH
(A Deemed University)
Bangalore – 560064, INDIA.
JUNE 2015

Dedicated to

My Family

DECLARATION

I hereby declare that the thesis entitled "**Electron Magnetic Circular Dichroism of Epitaxial Magnetic Thin Films at Nanoscale"** is an authentic record of research work carried out by me at the Chemistry and Physics of Materials Unit, International Centre for Materials Science, Jawaharlal Nehru Centre for Advanced Scientific Research, Bangalore, India under the supervision of **Dr. Ranjan Datta** and that it has not been submitted elsewhere for the award of any degree or diploma.

In keeping with the general practice in reporting scientific observations, due acknowledgment has been made whenever the work described is based on the findings of other investigators. Any omission that might have occurred due to oversight or error in judgment is regretted.

_____

B. Loukya Chowdary

CERTIFICATE

Certified that the work described in this thesis titled "**Electron Magnetic Circular Dichroism of Epitaxial Magnetic Thin Films at Nanoscale**" has been carried out by Ms. **B. Loukya Chowdary** at the Chemistry and Physics of Materials Unit, International Centre for Materials Science, Jawaharlal Nehru Centre for Advanced Scientific Research, Bangalore, India under my supervision and that it has not been submitted elsewhere for the award of any degree or diploma.

_____

Dr. Ranjan Datta

(Research Supervisor)

Acknowledgements

I take this opportunity to sincerely thank my research supervisor Dr. Ranjan Datta for his constant motivation, excellent guidance and encouragement throughout my Ph.D. His valuable instructions, comments and suggestions in preparing for seminars have helped me immensely. His endless enthusiasm for science and hard working nature has inspired and motivated me at various times.

I sincerely thank Prof. C. N. R. Rao for creating world class facilities at International Centre for Materials Science (ICMS). I specially thank him for providing aberration corrected transmission electron microscope facility at this centre that gave me an excellent opportunity to learn and carry out research on advanced microscopy techniques.

I would like to express my gratitude to Prof. Arunava Gupta for enthusiastic scientific collaborations and providing us high quality epitaxial magnetic thin films that greatly helped my research. I also thank Prof. Rajeev Ranjan, Prof. P. S. Anil Kumar, Dr. Ujjal Gautam and Dr. Sebastian Peter for fruitful collaborations and interesting research problems that helped me in learning a lot during the process.

I would like to specially thank all the researchers, Dr. Shipra, Dr. Nitesh, Dr. Ajay Kalyani, Dr. P. Silwal, N. Pachauri, Dr. M. Kesaria, R. Moumita, C. Manjeet, U. Subbarao, Dr. Ning Li, X. Zhang, Dr. L. S. Panchakarla, M. N. Iliev, D. H. Kim, N. D. Todorov, K. K. Nagaraja, Dr. S. Shetty, L. Shen, Dr. M. Althammer, N. Bao, A. Roy, P. Pramod, D. Khatua, A. N. Fitch, A. Senyshyn, B. Khodadadi, A. Singh, T. Mewes, M. K. Amshumali, Dr. K. Ramasamy for collaborating, helping us during various experiments and for their valuable discussions.

I would like to take this opportunity to specially thank Prof. S. Balasubramanian for the FORTRAN programming course, Prof. Umesh V. Waghmare for Computational Materials Science course and Prof. N. Ravishankar for the course on electron microscopy that helped me a lot during my Ph.D. I also would like to thank Prof. Shobhana Narasimhan, Prof. M. S. Hegde, Prof. T. N. Guru Row, and Prof. Amitabh Joshi for their excellent teaching and the courses they have offered.

I thank the past and present chairman of Chemistry and Physics of Materials Unit, Prof. G. U. Kulkarni and Prof. S. Balasubramanian for all their invaluable support.

I would like to thank the entire faculty at JNCASR for being a constant source of inspiration with their advanced research. I take this opportunity to thank all my past teachers at school and college level for sharing their knowledge, providing their support and encouragement without which it is impossible for me to be here.

I extend my gratitude to Dr. Jay Ghatak, for useful discussions and invaluable assistance during TEM experiments and data analysis. I also would like to thank Dr. Karthick Bala for assistance during TEM experiments.

I take this opportunity to thank my past and present labmates, Mr. Dileep, Ms. Sowjanya, Ms. Sireesha, Mr. Devendra, Mr. Rajib and Mr. Badri for their useful discussions and creating a cheerful environment.

I would like to thank Department of Science and Technology, India for the International Travel Grant to attend '2014 MRS Fall Meeting' at Boston, USA that gave me a new scientific exposure. I also thank the JNCASR centre for providing me JRF/SRF fellowship for carrying out my Ph.D research and also for funding me to attend various national/international conferences.

I extend my gratitude to all the efficient staff at the Library, Academic and Administration sections for their timely help and cooperation.

I would like to thank the Hostel staff, Mess workers, staff at Chandraiah canteen, for the homely environment and tasty food during my stay at JNCASR.

I acknowledge and thank all my friends inside and outside JNCASR for their immense support and being with me at all the times. I am lucky to have friends like Manjusha Namburi, Lavanya Kunduru, Sandeep Kumar, Ritapa Ghatak, Prasoona Sai, Chaitanya Sharma, and many more for being more than friends, and for all the joyous moments.

I finally acknowledge and thank all my family members for their unconditional love, support and encouragement. I am lucky to have wonderful mom who is also my ultimate friend. I specially thank my sister Lavanya Boddapati for being an inspiration, for her kindness and generosity. I dedicate this thesis to my family.

Last but not the least; I thank God Almighty for showering all his blessings upon me at every point of life and helping me in completing this thesis work. It is impossible for me to be here today without His blessings.

Synopsis

Transmission Electron Microscopy (TEM) and Electron Energy Loss Spectroscopy (EELS) are one of the most powerful and successful imaging and analytical tools available in materials science. Owing to the much smaller wavelength of electrons e.g., 0.0273 Å at 200 kV and strong interaction compared to visible light and X-ray based techniques, TEM is capable of providing information from materials not only at nanoscale but also at the atomic scale. TEM has long been used for structural and chemical composition analysis of materials by imaging and spectroscopy. Element specific orbital and spin magnetic information characterization by electron magnetic circular dichroism (EMCD) in a TEM is a recent development in the field of transmission electron microscopy. EMCD is an EELS based technique and is equivalent to X-ray Magnetic Circular Dichroism (XMCD) which is routinely performed in a synchrotron. EMCD in a TEM not only offers higher spatial resolution compared to XMCD but also bulk sensitive. However, EMCD was not possible in a TEM due to unavailability of spin polarized electron source till it was shown both by theoretically and experimentally to obtain such signal in the absence of a spin polarized source [C. Hébert *et al*., Ultramicroscopy 96 (2003) 46; P. Schattschneider *et al*., Nature 441 (2006) 486]. The technique so far has been limited to the moment ratio evaluation only and the extraction of individual orbital and spin moment values remained elusive. Moreover, the technique suffers from the poor signal to noise ratio in the experimental spectra. In the first major contribution to this technique we have demonstrated a method to improve the signal to noise ratio significantly at the nanometer length scale exploiting the gun monochromator excitation available in a FEI-TITAN 80-300 kV aberration corrected microscope. Our first experimentation was on CrO_2 epitaxial thin films grown on TiO_2 substrate with two different growth orientations and the results are compared with the previously performed XMCD data and first principle based calculations. In the subsequent work, we have quantitatively evaluated the site specific orbital and spin magnetic moment values from $NiFe_2O_4$ and $CoFe_2O_4$ epitaxial thin films exploiting a simple model developed by us which is based on site specific absorption of Bloch waves for the inverse spinel structure. We also have explained the experimentally observed low dichroic signal and the imbalance in dichroic signal observed between L_3 and L_2 absorption edges in terms of detection of EMCD signal along a particular momentum transfer direction. Besides this, we have applied EMCD technique to understand the

observed ferromagnetism in Co doped ZnO epitaxial thin films where composition dependent coercivity was reported. First principle based calculations were performed in order to understand the observed weak ferromagnetism associated with the Co atoms.

List of Publications

1. **B. Loukya**, D. S. Negi, K. Dileep, and R. Datta, Effect of Bloch wave electron propagation and momentum resolved signal detection on the quantitative and site specific EMCD of spinel oxide thin films, *Physical Review B 91, 134412 (2015).*
2. A. K. Kalyani, D. Khatua, **B. Loukya**, R. Datta, A. N. Fitch, A. Senyshyn, and R. Ranjan, Metastable monoclinic and orthorhombic phases and electric field induced irreversible phase transformation at room temperature in the lead free classical ferroelectric $BaTiO_3$, *Physical Review B, 91 (2015) 104104.*
3. D. S. Negi, **B. Loukya**, A. Gupta, and R. Datta, Spatially resolved quantitative measurement of magnetic order in spinel CuCr2S_4 nanocrystals, *Applied Physics Letters, 106 (2015) 182402.*
4. M. Chhetri, M. Rana, **B. Loukya**, Pramod K. Patil, R. Datta, Ujjal K. Gautam, Mechanochemical Synthesis of Free-Standing Platinum Nanosheets and Their Electrocatalytic Properties, *Advanced Materials (2015), DOI:10.1002/adma.201501056.*
5. R. Moumita, C. Manjeet, **B. Loukya**, P. Pramod, R. Datta, and G. K. Ujjal, High-yield synthesis of sub-10 nm Pt nanotetrahedra with Bare <111> facets for efficient electrocatalytic applications, *ACS Applied Materials and Interfaces, 7 (2015) 4998.*
6. N. Pachauri, B. Khodadadi, M. Althammer, A. Singh, **B. Loukya**, R. Datta, M. Iliev, T. Mewes and A. Gupta, Study of Structural and Ferromagnetic Resonance Properties of Spinel Lithium Ferrite ($LiFe_5O_8$) Single Crystals, *Journal of Applied Physics, (2015).*
7. K. Dileep, **B. Loukya**, P. Silwal, A. Gupta, and R. Datta, Probing optical band gaps at nanoscale from tetrahedral cation vacancy defects and variation of cation ordering in NiCo2O4 epitaxial thin films, *Journal of Physics D: Applied Physics, 47 (2014) 405001.*
8. K. Dileep, **B. Loukya**, N. Pachauri, A. Gupta, and R. Datta, Probing optical band gaps at nanoscale in NiFe2O4 and CoFe2O4 epitaxial films by high resolution electron energy loss spectroscopy, *Journal of Applied Physics, 116 (2014) 103505.*
9. D. S. Negi, A. Roy, **B. Loukya**, K. Dileep, S. Shetty, N. Kumar, P. S. Anil Kumar, and R. Datta, Epitaxial Co metal thin film grown by Pulsed Laser Deposition using oxide target, *Journal of Crystal Growth, 394 (2014) 112.*

10. R. Sahu, K. Dileep, **B. Loukya**, and R. Datta, Native defects affecting the Li atom distribution tune the optical emission of ZnO:Li epitaxial thin film, *Applied Physics Letters, 104 (2014) 051908.*
11. L. Shen, M. Althammer, N. Pachauri, **B. Loukya**, R. Datta, M. Iliev, N. Bao, and A. Gupta, Epitaxial growth of spinel cobalt ferrite films on $MgAl_2O_4$ substrates by direct liquid injection chemical vapor deposition, *Journal of Crystal Growth, 390 (2014) 61.*
12. D. Negi, **B. Loukya**, K. Dileep, R. Sahu, S. Shetty, N. Kumar, J. Ghatak, N. Pachauri, A. Gupta, and R. Datta, Structural and magnetic characterization of mixed valence Co (II, III)$_x$Zn$_{1-x}$O epitaxial thin films, *Journal of Magnetism and Magnetic Materials, 354 (2014) 39.*
13. D. S. Negi, **B. Loukya**, K. Dileep, R. Sahu, K. K. Nagaraja, N. Kumar, and R. Datta, Robust room temperature ferromagnetism in epitaxial CoO thin film, *Applied Physics Letters, 103 (2013) 242407.*
14. M. N. Iliev, P. Silwal, **B. Loukya**, R. Datta, D. H. Kim, N. D. Todorov, N. Pachauri, and A. Gupta, Raman studies of cation distribution and thermal stability of epitaxial spinel NiCo2O4 films, *Journal of Applied Physics, 114 (2013) 0333514.*
15. D. S Negi, **B. Loukya**, K. Dileep, M. Kesaria, N. Kumar, and R. Datta, Characterization of structure and magnetism in $Zn_{1-x}(Co_x/Mn_x)O$ epitaxial thin films as a function of composition, *Superlattices and Microstructures, 63 (2013) 289.*
16. **B. Loukya**, D. S. Negi, K. Dileep, N. Kumar, J. Ghatak, and R. Datta, Giant anisotropy in ferromagnetic Co doped ZnO thin film, *Journal of Magnetism and Magnetic Materials, 325 (2013) 159-164.*
17. R. Datta, **B. Loukya**, N. Li, and A. Gupta, Structural features of epitaxial NiFe2O4 thin films grown on different substrates by direct liquid injection chemical vapor deposition, *Journal of Crystal Growth, 345 (2012) 44.*
18. **B. Loukya**, X. Zhang, A. Gupta, and R. Datta, Electron magnetic chiral dichroism in CrO2 thin films using monochromatic probe illumination in a transmission electron microscope, *Journal of Magnetism and Magnetic Materials, 324 (2012) 3754.*
19. **B. Loukya**, P. Sowjanya, K. Dileep, R. Shipra, S. Kanuri, L. S. Panchakarla, and R. Datta, Controlling structural quality of ZnO thin film on c-plane sapphire during pulsed laser deposition, *Journal of Crystal Growth, 329 (2011) 20.*

Contents

Chapter 1

Introduction

This chapter gives an introduction on Electron Magnetic Circular Dichroism (EMCD) in a Transmission Electron Microscope along with an overview of the thesis on using EMCD on various materials at nanoscale.

1.1 Electron Magnetic Circular Dichroism in a Transmission Electron Microscope

Transmission Electron Microscopy (TEM) has been a routine characterization tool for structural and chemical composition analysis of materials by imaging and spectroscopy, respectively. Quantitative magnetic information by electron magnetic circular dichroism technique (EMCD) in a TEM is an innovative idea and new addition based on electron diffraction [1-3]. EMCD is equivalent to X-ray Magnetic Circular Dichroism (XMCD), which is routinely performed in a synchrotron to characterize atom specific orbital and spin magnetic moments in materials [4-6]. Though there are reports on linear dichroism studies in TEM [7] circular dichroism was thought to be possible only with existence of spin-polarized electron source in TEM due to the similarities recognized between the X-ray Absorption Near Edge Structure (XANES) and Energy Loss Near Edge Structures (ELNES) [1,8]. Principle of EMCD is discussed in detail in Section 1.1.1. Schattschneider *et al*., first theoretically proposed the possibility of a dichroic experiment in TEM in the year 2003 [1], later the experimental feasibility of such proposal named as 'Electron Magnetic Circular Dichroism (EMCD)' was proved in the year 2006 [2].

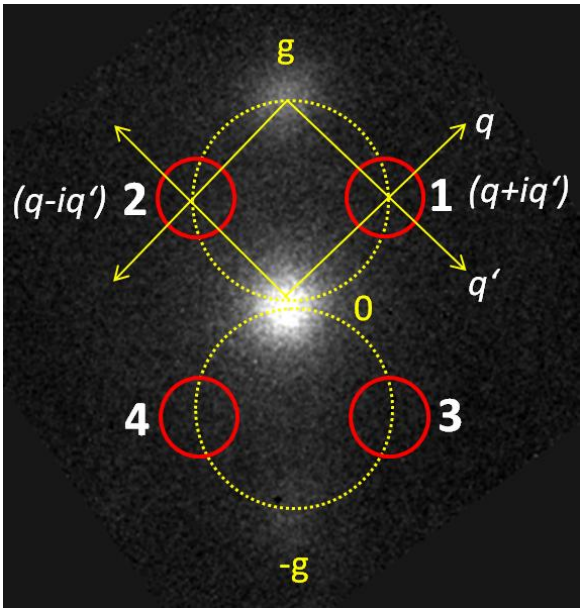

Figure 1.1. Showing three beam diffraction pattern marked with positions 1, 2, 3 and 4 at the symmetrically opposite positions on the Thales circle drawn connecting the direct and diffracted beams. The EMCD signal can be extracted from the difference of the signal from positions 1 and 2 or from positions 3 and 4 where the momentum transfer vectors (q & q') at these positions are perpendicular and opposite to each other.

It has been proposed that extracting electron energy loss spectra from such specified positions in the diffracting plane where the momentum transfer vectors from the direct and diffracted beams are phase shifted by (π/2) can give magnetic dichroic information as shown in Fig. 1.1. EMCD has been improved tremendously in the past few years both theoretically and experimentally [9-15]. Its experimental application has been tested on various materials [16-20]. There are several reports on the experimental related issues such as signal to noise ratio, instrument parameters and methods to overcome them [14,21,22]. Though there are several reports on the understanding of principles and experimentation on various materials with different techniques, still the technique is limited to evaluation of orbital to spin moment ratio [23-26]. This is because of the fact that EMCD sum rules are different than their XMCD counterpart and involves evaluation of '*K*' parameter [25]. This '*K*' parameter is highly sensitive to the experimental setup and needs precise evaluation of various experimental parameters. Theoretical proposals on atomic resolution EMCD are already made [27-32].

The present chapter emphasizes on the principle and importance of EMCD in studying magnetism at the nano and atomic scale justifying its uniqueness in comparison to other conventional techniques at this length scale. An overview of the thesis is also presented briefly mentioning our contributions on dichroic signal improvement at the nanoscale, first experimental results on CrO_2 epitaxial thin films, quantitative and site-specific EMCD in $NiFe_2O_4$ and $CoFe_2O_4$ epitaxial thin films with our approach in understanding dichroic signal from inverse spinels, and EMCD of Co doped ZnO epitaxial thin films where Co concentration dependent coercivity has already been reported.

1.1.1 Principle of EMCD

The principle of EMCD lies in the concept of establishing a mathematical equivalence between the theory of X-ray absorption and inelastic electron scattering [33] under dipole approximation at which $\vec{q}\cdot\vec{R}$ becomes equivalent to $\vec{\varepsilon}.\vec{R}$ (comparing Eq. 1.1 and Eq. 1.2) [1]. In both cases, the driving force is the electric field vector $\vec{E}$ and therefore the representation of circularly polarized photons in the case of X-ray absorption i.e., $\vec{\varepsilon}\pm i\cdot\vec{\varepsilon}'$ can be represented as $\vec{q}\pm i\cdot\vec{q}'$ in the case of inelastic electron scattering. Therefore, in EMCD experiment, one would require to have simultaneous momentum transfer by the direct ($\vec{q}$) and diffracted ($\vec{q}'$) beams in

the diffraction plane which are equal in magnitude but phase shifted by π/2. Experimentally, this is achieved in the diffraction space in a TEM where the crystal itself acts as an interferometer or beam splitter to produce direct and diffracted beams which are phase shifted by π/2 as shown in Fig. 1.1. The simultaneous and perpendicular momentum transfer by the direct and diffracted beams (see Fig. 1.1) at two opposite positions on a Thales circle drawn connecting the direct and diffracted beams would provide the necessary condition of momentum transfer for the EMCD experiment. The difference in the dichroic signal at these two positions results in the magnetic dichroic signal which is equivalent to the XMCD experiment. Double differential scattering cross-section for inelastic electron scattering is given by

$$\frac{\partial^2\sigma}{\partial E\partial\Omega}=\sum_{i,f}\frac{4\gamma^2}{a_0^2q^4}\frac{k_f}{k_i}\left|\left\langle f\left|\vec{q}\cdot\vec{R}\right|i\right\rangle\right|^2\delta\left(E_i-E_f+E\right) \quad \text{... (1.1)}$$

where, E is the energy loss, $|i\rangle,\langle f|$ are the initial and final states, a_o is the Bohr radius, $\vec{q}=\vec{k_i}-\vec{k_f}$ is the direction of momentum transfer, γ is the relativistic factor and $\vec{R}$ is the position vector of the target electron. In XANES, the absorption cross-section for a photon with energy E, under dipole approximation is given by

$$\sigma=\sum_{i,f}4\pi^2\hbar\alpha\omega\left|\left\langle f\left|\vec{\varepsilon}\cdot\vec{R}\right|i\right\rangle\right|^2\delta\left(E+E_i-E_f\right) \quad \text{... (1.2)}$$

where, α is the fine structure constant, $\vec{\varepsilon}$ is the polarization vector of the photon absorbed [34]. From Eq. (1.1) and Eq. (1.2) it is obvious that within dipole approximation, the polarization vector $\vec{\varepsilon}$ in XANES can be made equivalent to $\left(\frac{\vec{q}}{q}\right)$ in ELNES with electric field $\vec{E}$ as the driving force for in both the transitions [3]. Therefore, circularly polarized photons with polarization vector $(\vec{\varepsilon}\pm i\cdot\vec{\varepsilon}')$ with $\vec{\varepsilon}\perp\vec{\varepsilon}'$ is analogous to the momentum transfer vector $(\vec{q}\pm i\cdot\vec{q}')$ with $\vec{q}\perp\vec{q}'$ and $|\vec{q}|=|\vec{q}'|$ in the case of electron scattering. Now, by replacing the momentum transfer vector $\vec{q}$ by $(\vec{q}+i\cdot\vec{q}')$ in Eq. (1.1), the electron scattering cross-section equation transforms to Eq. (1.3).

$$\sigma_{\pm}(E)=\frac{\partial^2\sigma((q\pm iq'),E)}{\partial E\partial\Omega}=\frac{4\gamma^2k_f}{a_0^2k_i}\left\{\left|\langle f|q\cdot r|i\rangle\right|^2+\left|\langle f|q'\cdot r|i\rangle\right|^2\pm 2i\langle f|q\cdot r|i\rangle\langle f|q'\cdot r|i\rangle\right\}\delta\left(E_i-E_f+E\right)$$

$$=\frac{4\gamma^2k_f}{a_0^2k_i}\left\{\frac{S(\vec{q},\vec{q},E)}{\vec{q}^4}+\frac{S(\vec{q}',\vec{q}',E)}{\vec{q}'^4}\pm 2i\frac{S(\vec{q},\vec{q}',E)}{\vec{q}^2\vec{q}'^2}\right\}\delta\left(E_i-E_f+E\right) \quad \text{... (1.3)}$$

where γ is the relativistic factor, k_i and k_f are wave vectors before and after the interaction, respectively. $\sigma_{\pm}(E)$ is the differential scattering cross-sections for two different momentum transfer directions, $\frac{\partial^2\sigma}{\partial E\partial\Omega}$ double differential scattering cross section, $\vec{q}$ and $\vec{q}'$ are the $\frac{\pi}{2}$ dephased momentum transfer vectors, r the position vector, $\delta\left(E_i-E_f+E\right)$ is the Delta function that ensures the selected transition probability. The first two terms in Eq. (1.3), $S(\vec{q},\vec{q},E)$ and $S(\vec{q}',\vec{q}',E)$ are called Dynamic Form Factors (DFF) for the momentum transfer vectors $\vec{q}$ and $\vec{q}'$ respectively [35, 36] that describes the inelastic scattering of the electrons. The last term in Eq. (1.3) is the inelastic interference term called mixed dynamic form factor (MDFF) denoted by $S(\vec{q},\vec{q}',E)$. MDFF is a complex quantity and contains the magnetic information of the material and this term is zero for non-magnetic samples.

1.1.2 EMCD Sum Rules

EMCD sum rules for quantitative determination of magnetic moments are derived from differential cross section calculated for symmetric positions in the diffraction plane [23,25]. The derived spin and orbital moment sum rules are expressed in terms of experimental spectra and dynamical diffraction coefficients as given in Eq. (1.4) and Eq. (1.5) and after neglecting $\langle T_z\rangle$ in Eq. (1.6) and Eq. (1.7) respectively.

$$\frac{\int_{L_3}(\sigma_2-\sigma_1)dE-2\int_{L_2}(\sigma_2-\sigma_1)dE}{\int_{L_3+L_2}(\sigma_2+\sigma_1)dE}=K\left(\frac{2}{3}\frac{\langle S_z\rangle}{N_h}+\frac{7}{3}\frac{\langle T_z\rangle}{N_h}\right) \quad \text{... (1.4)}$$

$$\frac{\int_{L_3+L_2}(\sigma_2-\sigma_1)\,dE}{\int_{L_3+L_2}(\sigma_2+\sigma_1)\,dE}=K\frac{1}{2}\frac{\langle L_z\rangle}{N_h} \qquad \text{... (1.5)}$$

$$m_{\text{spin}}=\frac{3N_h}{K}\;\frac{3\int_{L_3}(\sigma_2-\sigma_1)\,dE-2\int_{L_3+L_2}(\sigma_2-\sigma_1)\,dE}{\int_{L_3+L_2}(\sigma_2+\sigma_1)\,dE} \qquad \text{... (1.6)}$$

$$m_{\text{orb}}=\frac{2N_h}{\mathrm{K}}\frac{\int_{L_3+L_2}(\sigma_2-\sigma_1)\,dE}{\int_{L_3+L_2}(\sigma_2+\sigma_1)\,dE} \qquad \text{... (1.7)}$$

Here, $\sigma_1=(\partial^2\sigma/\partial E\partial\Omega)_{pos1}$ and $\sigma_2=(\partial^2\sigma/\partial E\partial\Omega)_{pos2}$ are the differential scattering cross sections at two different positions. The terms $\langle S_z\rangle/N_h$, $\langle L_z\rangle/N_h$, and $\langle T_z\rangle/N_h$ are the ground-state expectation values of spin momentum, orbital momentum, and magnetic-dipole operators per hole in *d* bands respectively. The factor '*K*' is calculated derived for a very well defined geometry and it contains information related to dynamical effects. The expression for '*K*' is given by Eq. 1.8.

$$K=\frac{3\sum_{(n,m)}\sum_{(n',m')\neq(n,m)}\frac{\mathrm{Im}(A^{pos1}_{n,m;n',m'})\left[(\delta-n)(\varepsilon-m')-(\delta-n')(\varepsilon-m)\right]}{\left[(\delta-n)^2+(\varepsilon-m)^2+\frac{q_z^2}{g^2}\right]\left[(\delta-n')^2+(\varepsilon-m')^2+\frac{q_z^2}{g^2}\right]}}{\left\{\sum_{(n,m)}\frac{A^{pos1}_{n,m;n,m}\left[(\delta-n)^2+(\varepsilon-m)^2+2\frac{q_z^2}{g^2}\right]}{\left[(\delta-n)^2+(\varepsilon-m)^2+\frac{q_z^2}{g^2}\right]^2}+2\sum_{(n,m)}\sum_{(n',m')\neq(n,m)}\frac{\mathrm{Re}(A^{pos1}_{n,m;n',m'})\left[(\delta-n)(\delta-n')+(\varepsilon-m)(\varepsilon-m')+2\frac{q_z^2}{g^2}\right]}{\left[(\delta-n)^2+(\varepsilon-m)^2+\frac{q_z^2}{g^2}\right]\left[(\delta-n')^2+(\varepsilon-m')^2+\frac{q_z^2}{g^2}\right]}\right\}} \qquad \text{... (1.8)}$$

where, $\mathrm{Im}(A)=-2a_1a_2\frac{4\gamma^2k_f}{a_0^2k_i}$, $\mathrm{Re}(A)=2a_1a_2\frac{4\gamma^2k_f}{a_0^2k_i}$, $A=\frac{4\gamma^2k_f}{a_0^2k_i}(a_1^2+a_2^2)$, a_1 and a_2 represent plane waves corresponding to the direct and diffracted beams. Under simplified geometry, e.g., for two beam case, the expression for '*K*' reduces to Eq. 1.9.

$$K=\frac{48a_1a_2}{(a_1^2+a_2^2)(8+2\frac{q_z^2}{g^2})+(4a_1a_2\times2\frac{q_z^2}{g^2})} \qquad \text{... (1.9)}$$

It depends on the sample thickness, excitation error of the incident beam, detector position and aperture size [25]. Also these equations are derived assuming the beam is perfectly parallel. But in practice the beam may not be perfectly parallel and small convergence and partial coherence of electron source always exist. Therefore, by taking the ratio of the two equations and neglecting the effect of magnetic dipole operator, one can get rid of the effect of any dynamical coefficients and the ratio of the orbital to spin moments (m_{orb}/m_{spin}) can be calculated according to EMCD sum rules (as shown in Eq. (1.9)) since the equation now is free from the factor K.

$$\frac{m_{orb}}{m_{spin}} = -\frac{2}{3}\ \frac{\int_{L_3+L_2}(\sigma_2-\sigma_1)\,dE}{2\int_{L_3+L_2}(\sigma_2-\sigma_1)\,dE - 3\int_{L_3}(\sigma_2-\sigma_1)\,dE} \qquad \text{... (1.10)}$$

Expressions for spin moment and orbital moment in the case of XMCD for 3d transition elements [6] are given in Eq. (1.11) and Eq. (1.12) and after neglecting $\langle T_z \rangle$ in Eq. (1.13) and Eq. (1.14) respectively.

$$m_{spin} = -\frac{6\int_{L_3}(\mu_+-\mu_-)\,d\omega - 4\int_{L_3+L_2}(\mu_+-\mu_-)\,d\omega}{\int_{L_3+L_2}(\mu_++\mu_-)\,d\omega} \times (10-n_{3d}) \times \left(1+\frac{7T_z}{2S_z}\right)^{-1} \qquad \text{... (1.11)}$$

$$m_{orb} = -\frac{4\int_{L_3+L_2}(\mu_+-\mu_-)\,d\omega}{3\int_{L_3+L_2}(\mu_++\mu_-)\,d\omega} \times (10-n_{3d}) \qquad \text{... (1.12)}$$

$$m_{spin} = -2N_h\ \frac{3\int_{L_3}(\mu_+-\mu_-)\,d\omega - 2\int_{L_3+L_2}(\mu_+-\mu_-)\,d\omega}{\int_{L_3+L_2}(\mu_++\mu_-)\,d\omega} \qquad \text{... (1.13)}$$

$$m_{orb} = -\frac{4N_h}{3}\ \frac{\int_{L_3+L_2}(\mu_+-\mu_-)\,d\omega}{\int_{L_3+L_2}(\mu_++\mu_-)\,d\omega} \qquad \text{... (1.14)}$$

where m_{spin} and m_{orb} are the spin and orbital moments respectively in μ_B/atom units. n_{3d} is the 3d electron occupation number. L_3 and L_2 are the absorption edges denoting the integration range. $\langle T_z \rangle$ is the expectation value of magnetic dipole operator and $\langle S_z \rangle$ is equal to half of m_{spin} in Hartree atomic units. $(\mu_+ - \mu_-)$ denotes the MCD (magnetic circular dichroism) spectra and

$(\mu_+ + \mu_-)$ denotes the XAS (X-ray Absorption Spectra). Spin to orbital moment ratio according to XMCD sum rules is given in Eq. (1.15).

$$\frac{m_{orb}}{m_{spin}} = -\frac{2}{3}\ \frac{\int_{L_3+L_2}(\mu_+ - \mu_-)d\omega}{2\int_{L_3+L_2}(\mu_+ - \mu_-)d\omega - 3\int_{L_3}(\mu_+ - \mu_-)d\omega} \quad \text{... (1.15)}$$

The equations for m_{orb}/m_{spin} ratio according to EMCD and XMCD sum rules (Eq. (1.10) and Eq. (1.15)) are exactly the same in terms of integrated dichroic signal obtained by two different methods after neglecting $\langle T_z \rangle$ term but the individual sum rules are different in terms of multiplicative constants and parameter '*K*'. This means individual EMCD sum rules will be strongly dependent on the accurate determination of parameter '*K*'.

1.1.3 EMCD: Techniques to Improve Spatial Resolution

Study of magnetism at nano and atomic scale became extremely important in order to meet the increasing demands of device miniaturization in the rapidly expanding field of spintronics. There are many reports and demonstrations on the ability of EMCD technique to reach nano and atomic scale magnetism studies. The obtainable spatial resolution at the time of introduction of the technique was about 100-200 nm. This is limited by the size of the selected area aperture. In order to improve this limit either the size of the apertures in TEM have to be made smaller or have to develop new experimental methods in terms of modifying the scattering geometries during experiment. The convergent beam techniques like LACDIF [37,38] (Large Angle Convergent Diffraction) and CBED [13] (Convergent Beam Electron Diffraction) were used to acquire the dichroic signal with the improvement in the spatial resolution to 30 nm. But in the case of LACDIF method, the intensity of the signal is compromised with the spatial resolution due to the beam convergence while in the case of CBED technique, the signal intensity is compromised with the interference of the diffraction discs.

The spatial resolution was then improved to 2 nm by performing the experiment with convergent electron-beam diffraction in the scanning mode of TEM [9]. This method is demonstrated on an epitaxial Fe/Au multilayer film with a 3 nm wide Fe layer and a substantial increase in the spatial resolution of the magnetic dichroic signal was observed. This value can be further increased in a C_S corrected microscope. The geometry used in this experiment is shown in

Fig. 1.2. Convergent electron probe of 1.7 nm is scanned across the Au/Fe multilayer film in scanning mode of TEM. The Gaussian full width at half maximum (1.66 nm) calculated from the assumed Gaussian spot profile drawn across the Au/Fe multilayer indicated that the limiting factor for the resolution is the spot size of the probe. Acquiring EMCD signal from reciprocal space maps allows the extraction of quantitative magnetic moments with superior spatial resolution [24]. Also, availability of aberration corrected TEMs with high brightness sources can push the scale of obtainable information to atomic resolution [27-29].

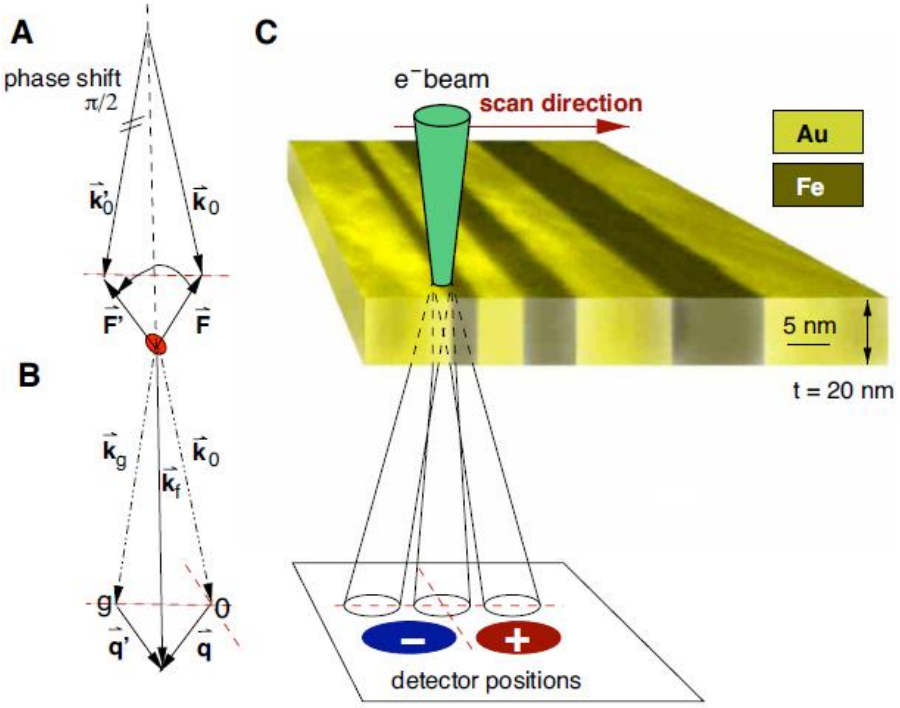

Figure 1.2. Geometry for EMCD experiment in STEM mode with convergent beam electron diffraction. (A) Two plane waves phase shifted by (π/2) producing a rotating electric field vector $\vec{F}$ *. (B) Detector positions with respect to '0' and 'g' beam after diffraction through the crystal and the final scattering direction* $\vec{k}_f$ *and momentum transfer directions are indicated. (C) EMCD experiment in convergent beam STEM mode showing the detector positions '+' and '–' in the diffraction plane. Copyright (2008) by American Physical Society [9].*

In short, the aim of each of these proposed experimental methods is to obtain higher spatial resolution along with high signal to noise ratio. In this context we have taken a different approach which was based on a gun monochromator excitation available with FEI TITAN^{3TM}

80-300 kV (kindly see Fig. 2.2) to improve the signal to noise ratio significantly. We obtained ~60 % higher signal to noise ratio with this method compared to that using probe in parallel mode (see Fig. 2.4). This technique routinely offers a spatial resolution of 5-10 nm. The EMCD experimental method and results using gun monochromator are discussed in Chapter 2.

1.2 EMCD in Comparison to Other Magnetism Characterization Techniques

EMCD is a recently evolved atomic and nano-scale magnetic characterization tool. There are many other magnetically sensitive microscopic techniques that have been extensively used to characterize magnetism of materials like Kerr-microscopy [39], Lorentz-microscopy [40], Scanning Electron Microscopy with Polarization Analysis (SEMPA) [41], Scanning Near-field Magneto-optical Microscopy (SNMOM) [42], Magnetic Force Microscopy (MFM) [43] etc. However, neither of these techniques have spatial resolution below 10 nm. Scanning Tunneling Microscopy (STM) [44,45] can routinely give atomic level spatial resolution but it is essentially a surface characterization technique. Moreover, EMCD is the only available technique that allows the evaluation of bulk sensitive and element specific spin and orbital magnetic moments at nanoscale. Electron holography in TEM is another technique used to characterize magnetic field distribution which is based on the interference of coherent electron waves [46-49]. Recent advancement in the technology has lead to the availability of vortex electron beam in TEMs. The vortex electron beams carrying high angular momentum [31,32,50] can be used to study atomic scale magnetism and also has applications in electron tweezing. Research in this direction is still emerging.

1.3 Overview of the Thesis

We have carried out our first experimental EMCD on CrO_2 epitaxial thin films grown on TiO_2 substrate along two different growth orientations [51]. In this work, we have shown how one can exploit the gun monochromator available with FEI TITAN^{3TM} 80-300 kV meant for high energy resolution (better than 0.18 eV) EELS spectroscopy to increase the signal to noise ratio significantly from an area as small as 5 sq. nm while ensuring that the out coming electron beam is in parallel mode as evident from the diffraction spots [52]. Though our results closely matches with the first principle based calculations of atom specific magnetic moments for the two different CrO_2 thin films but they are not in agreement with the experimental XMCD

measurement. Experimental and calculated results are discussed and we point out some possible reasons for this discrepancy [52].

Subsequently, we have carried out quantitative EMCD of two important spinel oxide epitaxial thin films, $NiFe_2O_4$ and $CoFe_2O_4$ grown by Direct Liquid Injection Chemical Vapor Deposition method [53]. Our goal was to probe the difference in magnetic signal obtained from the perfect inverse spinel configurations and the regions with A site cation vacancies and cation mixing [54-56]. During this experimentation we observed that dichroic signal is very low irrespective of sample thickness and an imbalance in dichroic signal exists between L_3 and L_2 absorption edges. The low dichroic signal was explained based on oscillating nature of propagating Bloch waves in the crystal and the imbalance in signal was explained based on particular momentum resolved signal detection during EMCD experimentation. We also have developed one simple model for the site specific magnetic signal evaluation for inverse spinel structure which is important for any quantitative work in this system. This particular work is important and the results strengthen the promise of utilizing EMCD as a routine nanoscale magnetic characterization technique [57].

We have also applied EMCD technique to study element specific magnetism in Co doped ZnO epitaxial thin films [58] where we already reported Co concentration dependent coercivity in ZnO. We developed a method on how to grow epitaxial thin film of ZnO on highly lattice mismatched (~18.4 %) *c*-plane sapphire [59]. This method was used to grow all the epitaxial ZnO thin films. The solubility limit of Co and Mn in ZnO was studied and thin films were grown by pulsed laser deposition method. Structural and magnetic characterization was done. Materials characterizations in terms of composition and macroscopic magnetic study is done by EDX (Energy-dispersive X-ray Spectroscopy) and SQUID (Superconducting Quantum Interference Device) respectively. We already have explained the experimentally observed giant coercivity due to charge transfer from Co *d* electrons to the defect band. DFT based calculation was carried out to check the energy landscape of Co *d* electron states and the defect states whether such charge transfer is feasible. Experimental EMCD shows weak magnetism at the Co atoms thus confirming that the origin of magnetism in this system is predominantly from the defects and the observed coercivity is due to the interaction of Co with defect level via charge transfer.

1.4 Bibliography

[1]. C. Hébert, and P. Schattschneider, Ultramicroscopy 96 (2003) 463.

[2]. P. Schattschneider, S. Rubino, C. Hébert, J. Rusz, J. Kuneš, P. Novák, E. Carlino, M. Fabrizioli, G. Panaccione, and G. Rossi, Nature 441 (2006) 486.

[3]. P. Schattschneider, Linear and Chiral Dichroism in the Electron Microscope, CRC Press, Taylor & Francis Group, 2011.

[4]. G. Schütz, W. Wagner, W. Wilhelm, P. Kienle, R. Zeller, R. Frahm, and G. Materlik, Phys. Rev. Lett. 58 (1987) 737.

[5]. B. T. Thole, P. Carra, F. Sette, and G. van der Laan, Phys. Rev. Lett. 68 (1992) 1943.

[6]. C. T. Chen, Y. U. Idzerda, H. –J. Lin, N. V. Smith, G. Meigs, E. Chaban, G. H. Ho, E. Pellegrin, and F. Sette, Phys. Rev. Lett. 75 (1995) 152.

[7]. J. Yuan, and N. K. Menon, J. Appl. Phys. 81 (1997) 5087.

[8]. A. P. Hitchcock, Jpn. J. Appl. Phys. 32 (1992) 176.

[9]. P. Schattschneider, M. Stöger-Pollach, S. Rubino, M. Sperl, C. Hurm, J. Zweck, and J. Rusz, Phys. Rev. B 78 (2008) 104413.

[10]. P. Schattschneider, I. Ennen, M. Stöger-Pollah, J. Verbeeck, V. Mauchamp, and M. Jaouen, Ultramicroscopy 110 (2010) 1038.

[11]. H. Lidbaum, J. Rusz, A. Liebig, B. Hjörvarsson, P. M. Oppeneer, E. Coronel, O. Eriksson, and K. Leifer, Phys. Rev. Lett. 102 (2009) 037201.

[12]. J. Verbeeck, C. Hébert, S. Rubino, P. Novák, J. Rusz, F. Houdellier, C. Gatel, and P. Schattschneider, Ultramicroscopy 108 (2008) 865.

[13]. S. Rubino, P. Schattschneider, M. Stöger-Pollah, C. Hébert, J. Rusz, L. Calmels, B. Warot-Fonrose, F. Houdellier, V. Serin, and P. Novak, J. Mater. Res. 23 (2008) 2582.

[14]. B. Warot-Fonrose, F. Houdellier, M. J. Hÿtch, L. Calmels, V. Serin, and E. Snoeck, Ultramicroscopy 108 (2008) 393.

[15]. C. Gatel, B. Warot-Fonrose, P. Schattschneider, Ultramicroscopy 109 (2009) 1465.

[16]. R. C. Che, C. Y. Liang, X. He, H. H. Liu, and X. F. Duan, Sci. Technol. Adv. Mater. 12 (2011) 025004.

[17]. L. Calmels, and J. Rusz, J. Appl. Phys. 109 (2011) 07D328.

[18]. Z. H. Zhang, X. Wang, J. B. Xu, S. Muller, C. Ronning, and Q. Li, Nat. Nanotech. 4 (2009) 523.

[19]. I. Ennen, S. Löffler, C. Kübel, D. Wang, A. Auge, A. Hütten, and P. Schattschneider, J. Magn. Magn. Mater. 324 (2012) 2723.

[20]. Z. Q. Wang, X. Y. Zhong, R. Yu, Z. Y. Cheng, and J. Zhu, Nat. Comm. 4 (2013) 1395.

[21]. J. Rusz, P. M. Oppeneer, H. Lidbaum, S. Rubino, and K. Leifer, J. Microscopy 237 (2009)465.

[22]. B. Warot-Fonrose, C. Gatel, L. Calmels, V. Serin, and P. Schattschneider, Ultramicroscopy 110 (2010) 1033.

[23]. J. Rusz, O. Eriksson, P. Novák, and P. M. Oppeneer, Phys. Rev. B 76 (2007) 060408.

[24]. H. Lidbaum, J. Rusz, A. Liebig, B. Hjörvarsson, P. M. Oppeneer, E. Coronel, O. Eriksson, and K. Leifer, Phys. Rev. Lett. 102 (2009) 037201.

[25]. L. Calmels, F. Houdellier, B. Warot-Fonrose, C. Gatel, M. J. Hÿtch, V. Serin, E. Snoeck, and P. Schattschneider, Phys. Rev. B 76 (2007) 060409.

[26]. J. Rusz, H. Lidbaum, A. Liebig, B. Hjörvarsson, P. M. Oppeneer, S. Rubino, O. Eriksson, and K. Leifer, J. Magn. Magn. Mater. 322 (2010) 1478.

[27]. P. Schattschneider, I. Ennen, S. Löffler, M. Stöger-Pollach, and J. Verbeeck, J. Appl. Phys. 107 (2010) 09D311.

[28]. P. Schattschneider, B. Schaffer, I. Ennen, and J. Verbeeck, Phys. Rev. B 85 (2012) 134422.

[29]. P. Schattschneider, J. Verbeeck, and A. L. Hamon, Ultramicroscopy 109 (2009) 781.

[30]. J. Rusz, J. Idrobo, and S. Bhowmick, Phys. Rev. Lett. 113 (2014) 145501.

[31]. L. Clark, A. Béché, G. Guzzinati, and J. Verbeeck, Phys. Rev. A 89 (2014) 053818.

[32]. J. Rusz, S. Bhowmick, M. Eriksson, and N. Karlsson, Phys. Rev. B. 89 (2014) 134428.

[33]. P. Schattschneider, Fundamentals of Inelastic Electron Scattering, Springer, New York, 1986.

[34]. J.C. Fuggle, J. E. Inglesfield (Eds.), Unoccupied Electronic States, Springer, Berlin, 1992.

[35]. M. Nelhiebel, N. Luchier, P. Schorsch, P. Schattschneider, and B. Jouffrey, Phil. Magazine B 79 (1999) 941.

[36]. P. Schattschneider, M. Nelhiebel, H. Souchay, and B. Jouffrey, Micron 31 (2000) 333.

[37]. J. P. Morniroli, F. Houdellier, C. Roucau, J. Puiggalí, S. Gestí, A. Redjaïmia, Ultramicroscopy 108 (2008) 100.

[38]. P. Schattschneider, C. Hébert, S. Rubino, M. Stöger-Pollach, J. Rusz, and P. Novák, Ultramicroscopy 108 (2008) 433.

[39]. A. Hubert, R. Schäfer, Magnetic Domains, Springer, 1998.

[40]. J. N. Chapman, J. Phys. D 17 (1984) 623.

[41]. K. Koike, J. Electr. Microsc. 47 (1994) 157.

[42]. E. Betzig, J. K. Trautmann, R. Wolfe, E. M. Gyorgy, P. L. Flinn, Appl. Phys. Lett. 61 (1992) 142.

[43]. Y. Martin, H. K. Wickramasinghe, Appl. Phys. Lett. 50 (1987) 1455.

[44]. G. Binning, H. Rohrer, C. Gerber, E. Weibel, Phys. Rev. Lett. 50 (1983) 120.

[45]. R. Wiesendanger, H. –J. Güntherodt, G. Güntherodt, R. J. Gambino, R. Ruf, Phys. Rev. Lett. 65 (1990) 247.

[46]. H. Lichte, and M. Lehmann, Rep. Prog. Phys. 71 (2008) 016102.

[47]. D. Gabor, Nature 161 (1948) 563.

[48]. D. Gabor, Proc. R. Soc. A 197 (1949) 545.

[49]. M. E. Haine, and T. Mulvey, J. Opt. Soc. Am. 42 (1952) 763.

[50]. J. Verbeeck, H. Tian, and P. Schattschneider, Nature 467 (2010) 302.

[51]. M. Pathak, H. Sato, X. Zhang, K. B. Chetry, D. Mazumdar, P. LeClair, and A. Gupta, J. Appl. Phys. 108 (2010) 053713.

[52]. B. Loukya, X. Zhang, A. Gupta, and R. Datta, J. Magn. Magn. Mater. 324 (2012) 3754.

[53]. N. Li, Y. A. Wang, M. N. Iliev, T. M. Klein, and A. Gupta, Chem. Vap. Deposition 17 (2011) 261.

[54]. R. Datta, S. Kanuri, S. V. Karthik, D. Mazumdar, J. X. Ma, and A. Gupta, Appl. Phys. Lett. 97 (2010) 071907.

[55]. R. Datta, B. Loukya, N. Li, and A. Gupta, J. Cryst. Growth 345 (2012) 44.

[56]. K. Dileep, B. Loukya, N. Pachauri, A. Gupta, and R. Datta, J. Appl. Phys. 116 (2014) 103505.

[57]. B. Loukya, D. S. Negi, K. Dileep, N. Pachauri, A. Gupta, and R. Datta, Phys. Rev. B 91 (2015) 134412.

[58]. B. Loukya, D. S. Negi, K. Dileep, N. Kumar, J. Ghatak, and R. Datta, J. Magn. Magn. Mater. 345 (2013) 159.

[59]. B. Loukya, P. Sowjanya, K. Dileep, R. Shipra, S. Kanuri, L. S. Panchakarla, and R. Datta, J. Cryst. Growth 329 (2011) 20.

Chapter 2

EMCD of CrO_2 Epitaxial Thin Films at Nanoscale with Significant Improvement in Signal to Noise Ratio

This chapter first discusses the experimental aspects of electron magnetic circular dichroism particularly on improvement of the signal to noise ratio significantly at nanoscale. Detailed EMCD experimental results on CrO_2 epitaxial thin films with this new technique are discussed in the second half of the chapter.

This work has been published in Journal of Magnetism and Magnetic Materials 324 (2012) 3754.

2.1 Introduction

CrO_2 is the only known half-metal [1,2] with spin polarization as high as 98% measured through Point-contact Andreev reflection [3-5] and Meservey-Tedrow Spin-polarized tunneling measurements [6]. This makes CrO_2 an attractive candidate for spintronics. It crystallizes in tetragonal rutile structure (space group: D_{4h}^{14} : $P4_2/mnm$) with each Cr atom octahedrally coordinated around the oxygen atoms. It has inversion symmetry about the body centered Cr atom which means that the dichroic signal obtained is due to the presence of magnetic moments and not due to the lack of inversion symmetry. We have performed EMCD experimentation of CrO_2 epitaxial thin films grown on TiO_2 substrate with two different orientations i.e., (100) and (110) by Chemical Vapor Deposition Method (CVD) [7]. The thickness of the film grown is ~ 45 nm. The (100)-oriented film remains strained (compressive strain along (010) and tensile strain along (100)) whereas (110)-oriented film is fully relaxed [8,9]. The (110) oriented film shows higher spin magnetic moment compared to (100) oriented film at room temperature. XMCD measurement on these two set of samples shows 50% higher spin magnetic moment for the relaxed (110) film compared to strained (100) film which is also consistent with the observation of higher Curie temperature for the former film sample [10].

EMCD of these two different CrO_2 thin films are studied with a different experimental approach i.e. using a gun monochromator in an aberration corrected transmission electron microscope operating at 300 kV. Excellent signal-to-noise ratio is obtained with spatial resolution ~10 nm using a monochromatic probe as compared to conventional parallel illumination (~ 60% improvement), large area convergent beam electron diffraction and scanning transmission electron microscopy techniques of EMCD. Relatively rapid exposure using mono probe illumination enables collection of EMCD spectra in total of 8-9 minutes in energy filtered imaging mode for a given Cr $L_{2,3}$ energy scan (energy range ~35 eV). We compared the EMCD signal obtained by extracting the Cr $L_{2,3}$ spectra under three beam diffraction geometry of two different reciprocal vectors (namely g = 110 and 200) and found that the g = 200 vector enables acquisition of excellent EMCD signal from relatively thicker specimen area due to the associated larger extinction distance. Orbital to spin moment ratio has been calculated using EMCD sum rules derived for 3*d* elements and the dichroic spectral features associated with CrO_2 are discussed in comparison with calculated XMCD spectra.

2.2 Experimental Details

2.2.1 Cross-sectional and Plan View TEM Sample Preparation

Cross-sectional thin film TEM samples were prepared by conventional mechanical polishing and Ar ion milling to perforation so as to obtain a large electron transparent thin area. Different steps of sample preparation are described below.

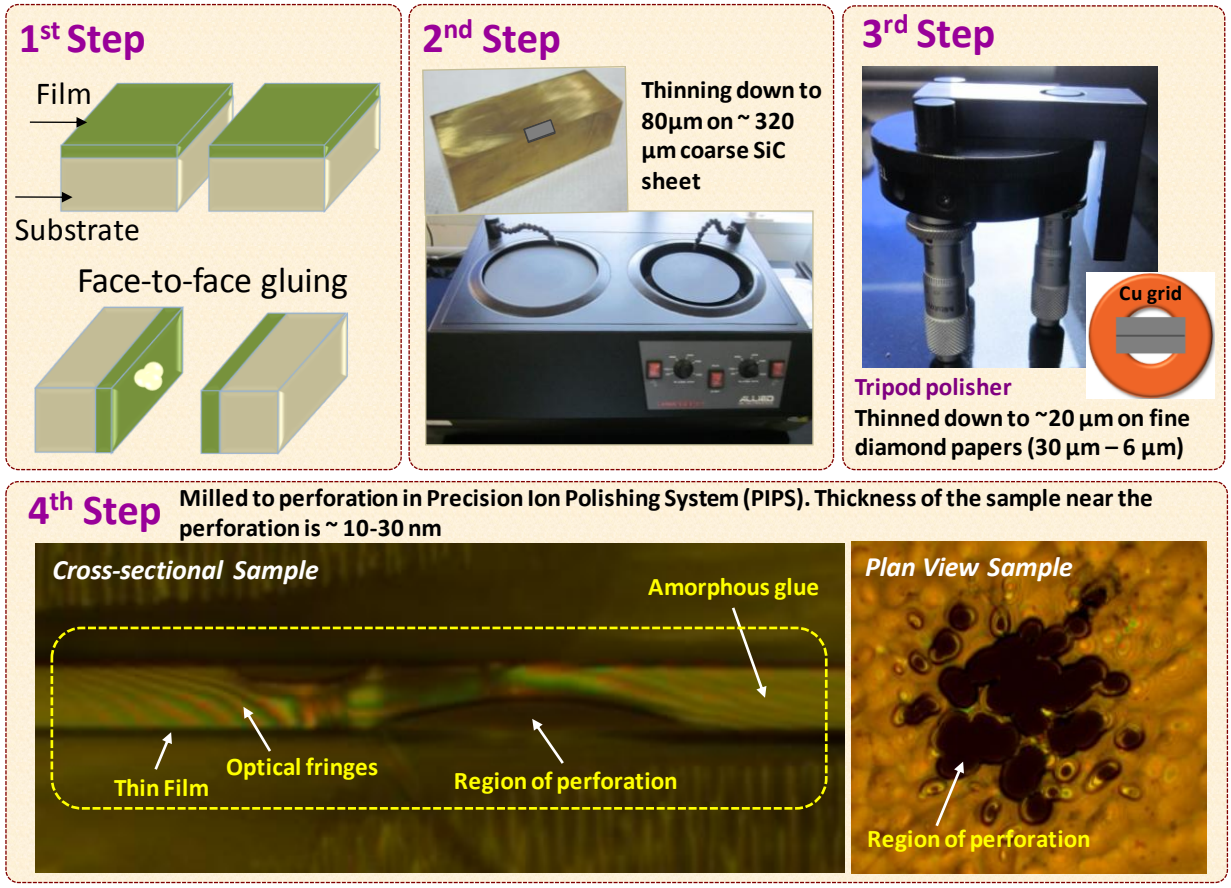

Figure 2.1. Step-by-step procedure of thin film TEM cross-sectional sample preparation. First two steps involve face-to-face gluing and mechanical polishing of the sample to thin down to 80 µm. In the third step, sample is further thinned down to <20 µm using a hand held tripod polisher. The sample is then mounted on copper grid and milled to perforation in a Gatan Precision Ion Polishing System (PIPS) to obtain an electron transparent thin area as shown in the figure as a part of 4^{th} step. The optical images of both cross-sectional and plan view samples at the region of perforation are shown.

Figure 2.1 shows the step-by-step procedure for the cross-sectional TEM sample preparation. First step involves the face-to-face gluing of films to prepare a sandwich. The

assembly is then mounted on a brass block with a temporary mounting wax having melting point of 135 ºC. The second step involves mechanical polishing along the cross-sectional direction shown in the Fig. 2.1 in order to shape it to fit within 3 mm Cu grid and to reduce the thickness to below 80 µm. Mechanical polishing was done using SiC polishing papers. In the next step, the thickness is further reduced to < 20 µm using diamond polishing sheets of varying grit sizes from 30 to 6 µm. The sample is then mounted on to a copper grid and milled in the precision Ar ion polishing machine to perforation. The beam settings used were ±7° and 4 keV energy. The voltage was reduced to 3 kV at the end to remove any surface amorphous layer. Similar procedure of mechanical polishing and Ar ion milling is followed in the case of plan view sample preparation except that face-to-face gluing of the films is not done. The polishing is done from the substrate side and thinned down to < 20-30 µm before ion milling to perforation. Here both the Ar ion gun beams are set at +7° and 4 keV with no modulation.

2.2.2 Effect of Gun Monochromator Excitation on the Improvement of the Signal

We employed gun monochromator excitation equipped with FEI TITAN^{3TM} 80-300 kV (see Fig. 2.2) microscope to improve the dichroic signal to noise ratio significantly compared to other methods discussed in the literature. The monochromator excitation is based on the principle of Wien filter where the electron beam is dispersed by applying a static potential in the plane perpendicular to its propagation. Depending on the applied potential and corresponding dispersion, the probe elongates in a plane perpendicular to the applied field. The central bright region of the probe has an energy resolution better than 180 meV as measured from the full width at half maxima of the zero loss peak at 300 kV. A parallel slit at the height of C1 condenser lens is used to select the central bright region of the probe and the illumination size can be controlled. Such a focused monochromatic probe offers high electron flux and improves the signal to noise ratio significantly. Fig. 2.3 (a) shows monochromatic probe focused and centered at the height of C1 aperture. Fig. 2.3 (b) shows the CrO_2 (110) thin film (~45 nm thickness) illuminated by the central bright region of the monochromatic probe selected by the slit perpendicular to the energy spread. Fig. 2.3 (c) shows the spot like diffraction pattern from the film along <001> zone axis. (200) and (110) spots are indexed in the diffraction pattern. Spot like diffraction pattern also indicates that the monochromatic probe illuminating the sample is essentially a plane wave.

Figure 2.2. FEI TITAN^{3TM} 80-300 kV at International Centre for Materials Science (ICMS), Jawaharlal Nehru Centre for Advanced Scientific Research (JNCASR), Bangalore. It has double Cs corrector technology with both image and probe corrector systems.

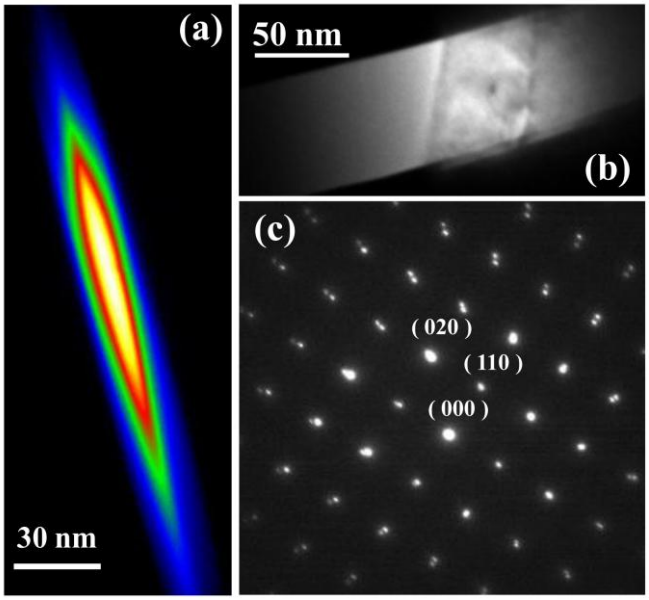

Figure 2.3. (a) Mono chromatic probe at the height of C1 lens, (b) Central part of the probe as selected by parallel slit and (c) Selected area diffraction pattern from CrO_2 / TiO_2 along 001 zone axis and <200> and <110> spots are indexed. Copyright (2012) by Elsevier [33].

Parallel probe (for obtaining spot like diffraction pattern) is essential for EMCD experiment to allow the extraction of EMCD signal from the desired positions in between the diffraction spots unlike the convergent beam case where the diffraction spots are discs like and difficult to place the aperture in between the broadened discs. The EMCD signal is extracted in the 3-beam condition from the positions 1 & 2 or 3 & 4 on the Thales circle as shown in Fig. 2.4.

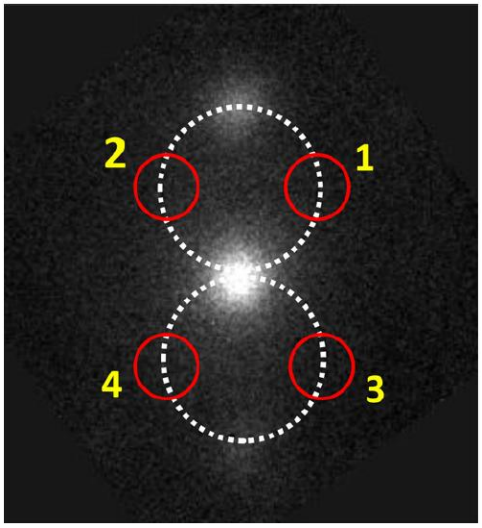

Figure 2.4.The three beam diffraction pattern marked with positions 1, 2, 3 and 4 at the symmetric positions on the thales circle drawn connecting the direct and diffracted beams. The EMCD signal can be extracted taking the difference of the signal from position 1 & 2 or from position 3 & 4. Copyright (2012) by Elsevier [33].

Cr $L_{2,3}$ signal obtained in parallel mode illumination (mono focus spread at C1 is ~ -24) and mono probe illumination (mono focus spread at C1 is ~ 0, highly converged) with inserted slit to select the central bright region are compared in Fig. 2.5. An improvement ~ 200,000 (~ 60%) in terms of counts/intensity can easily be obtained with mono probe illumination for the same exposure time and area of acquisition. Parallel illumination is important as we know from previously published results that the EMCD signal degrades with increasing convergence angle (spread in the range of *k* vectors increases with the increase in probe convergence angle which reduces the EMCD signal) [11]. Therefore, small probe (down to few Å) along with parallel illumination (or very little convergence) are required for near atomic resolution (few nm) and better dichroic signal. With mono probe illumination we can easily work with parallel illumination with spatial resolution close to 5 nm (at spot size 3) while maintaining excellent signal to background ratio for energy filtered diffraction pattern image acquisition.

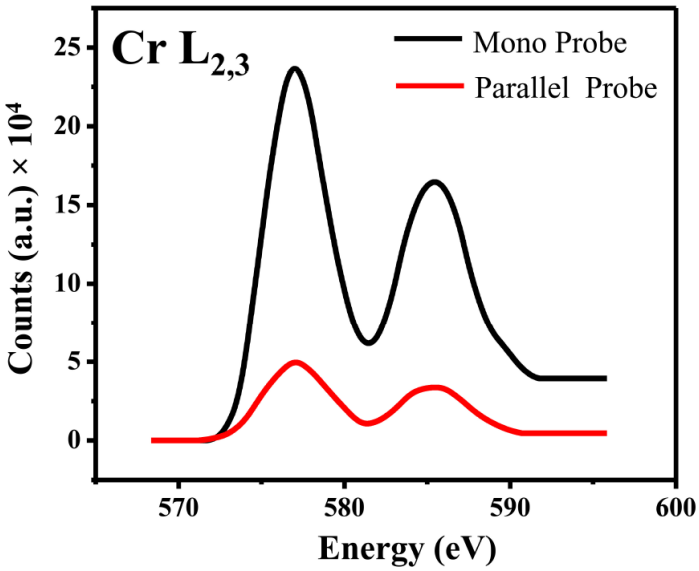

Figure 2.5. Comparison of signal over background between Cr $L_{2,3}$ spectra acquired with mono probe parallel beam illumination and usual parallel beam illumination. Copyright (2012) by Elsevier [33].

2.2.2.1 EMCD Spectra Acquisition and Data Analysis Method

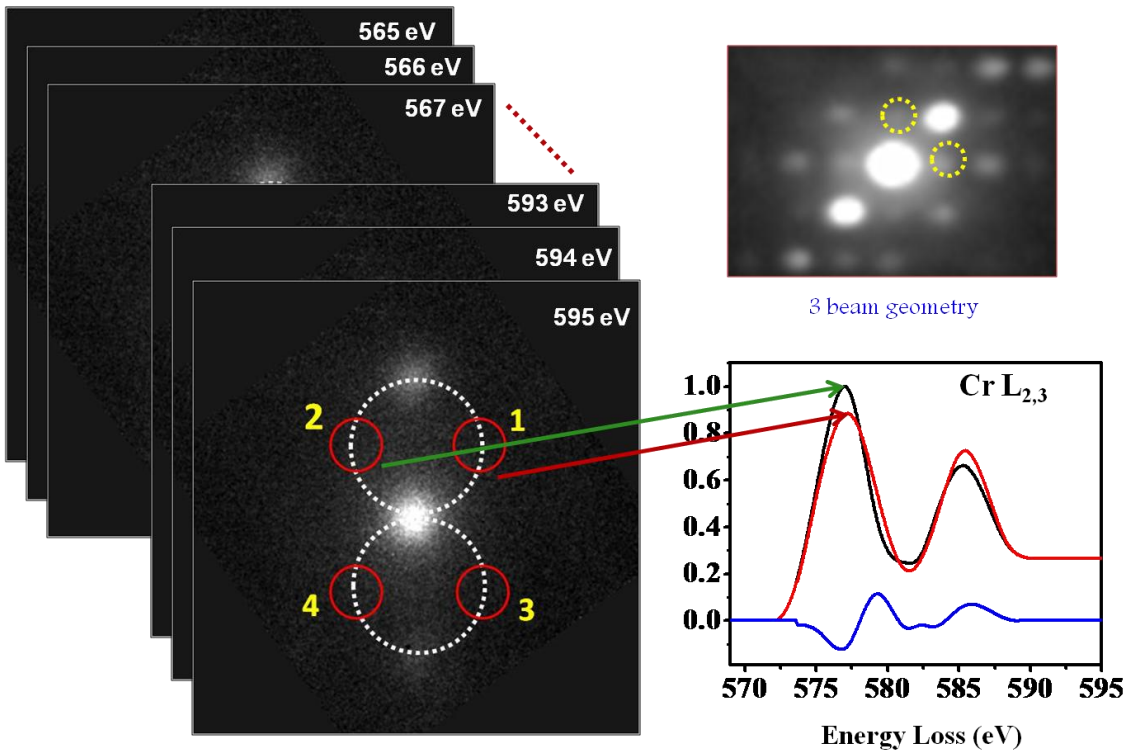

Figure 2.6. Energy-filtered diffraction patterns acquired in scanning the Cr $L_{2,3}$ edge with 1 eV energy step. The Cr $L_{2,3}$ is plotted by extracting the intensities from the positions 1 and 2 as a function of energy.

Energy filtered diffraction pattern imaging was acquired using a Gatan Tridiem camera in a filtered series acquisition mode. Gain correction and GIF tuning (up to 3rd order) were performed to account for uniform signal response and isochromaticity. Energy Filtered series was acquired with 1 eV energy slit with an energy loss step of 1 eV for the energy range 565-590 eV as shown in Fig. 2.6. Each image was acquired with 15 sec exposure time with a total acquisition time of ~ 390 sec. Crystal is tilted to obtain a three beam diffraction geometry (experiments were performed with g = 110 and 200 excitations) for which more symmetrical EMCD signal was reported on Thales circle compared to two beam case where EMCD signal distribution is more towards the diffracted spots [12, 13]. The data is extracted from the energy spectroscopic images by placing a digital aperture ($0.5g \times 0.5g$) on opposite sides of Thales circle (at position 1 and 2 as marked with red circle in Fig. 2.6 and plotted as a function of energy loss of the image using a homemade FORTRAN code which reads the intensity value of each pixel of the energy spectroscopic image. It also detects and removes any spurious X-ray spots from each image. The algorithm of the FORTRAN code is shown in Fig. 2.7.

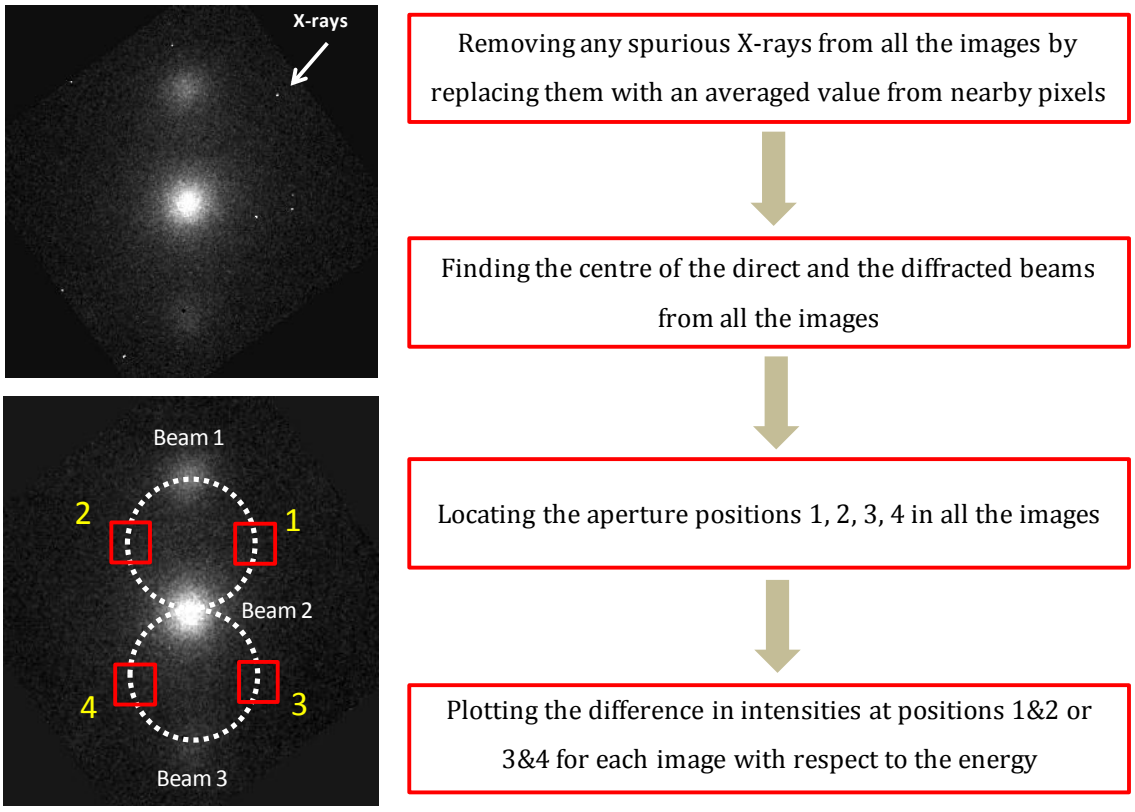

Figure 2.7. The flow of algorithm followed for writing the FORTRAN programming code to extract the EMCD spectra from the energy-filtered diffraction data sets.

2.2.3 Effect of Choice of Reciprocal Lattice Vectors on the EMCD Signal

Dynamical nature of electron diffraction and propagation of Bloch waves inside the crystal results in oscillation of EMCD signal as a function of sample thickness [14]. Larger reciprocal vectors (g) have larger extinction distance, ξ_g [15] for a given material and therefore the choice of larger 'g' allows working with thicker samples during EMCD experiments. Typical values of extinction distance for CrO_2 for different 'g' vectors along with the amplitude at 300 kV is given in Table 2.1. Figure 2.8 (a) shows the oscillation of two different Bloch waves as a function of sample thickness considering absorption using simplified expression given in Eq. (2.1). Figure 2.8 (b) is the corresponding simulated EMCD signal using 'bw code' for 3-beam geometry. Here, MDFF is simulated for a simplified case by Löffler et al. case to account for dipole transitions in one-electron case under first order Born approximation [16].

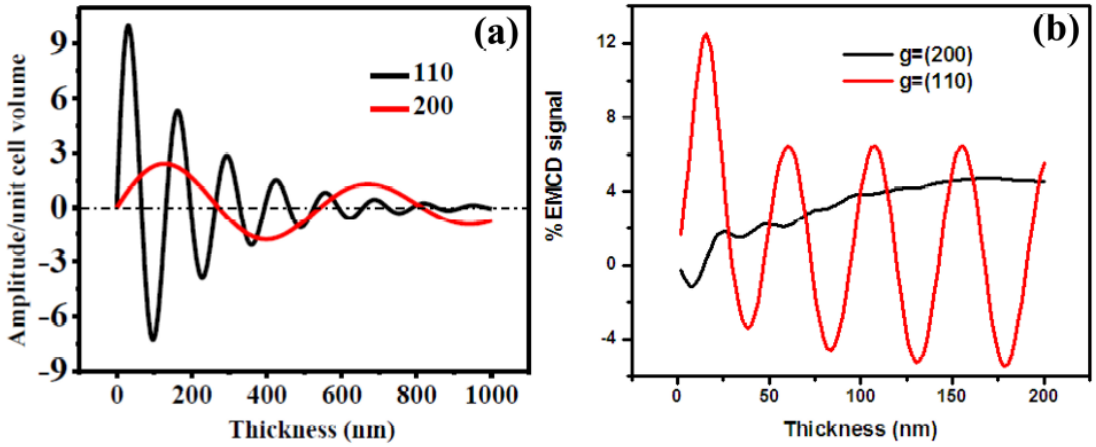

Figure 2.8. (a) Bloch waves propagation through crystal for g = 200 and g = 110 under two beam diffraction condition as a function of crystal thickness at 300 kV. The wave along g =110 oscillates with higher frequency than g= 200 vector and has smaller extinction distance compared to g = 200. (b) EMCD signal variation as a function thickness corresponding to g = 110 and 200. Copyright (2012) by Elsevier [33].

We see that amplitude of the Bloch wave for smaller 'g' vector oscillates with higher frequency with respect to thickness when compared to that of larger 'g'. This results in significant variation in the signal with a very small change in the thickness of the sample and also at certain thicknesses the signal may be very poor. This results in difficulty in carrying out comparative studies of different samples for which thickness at a given area may not be exactly

the same. We acquired EMCD spectra with two different 'g' vectors, namely 110 and 200. Reciprocal lattice vector g = 200 has large ξ_g (~ 271.25 nm) but lower amplitude compared to g = 110 (ξ_g ~ 65.64 nm).

$$\phi_g = \alpha_g \sin\left(\frac{\pi t}{\xi_g}\right)\exp\left(-\frac{\pi t}{\xi_g'}\right) \quad \text{... (2.1)}$$

The terms in Eq. (2.1), ϕ_g represents the amplitude of the diffracted beam for reflection 'g' and the intensity is given by $|\phi_g|^2$, 'α_g' is the Bloch wave excitation amplitude and is a constant in the absence of absorption inside the crystal, 't' is the thickness of the crystal, 'ξ_g' which is referred to as 'extinction distance' is the characteristic length for reflection 'g' and ξ_g' is the absorption length and is typically equal to 10 ξ_g.

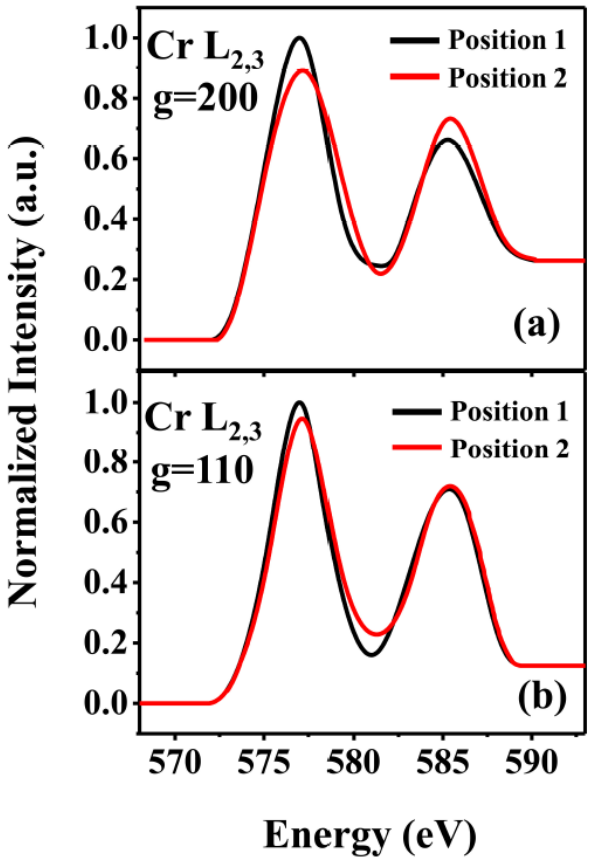

Figure 2.9. Cr $L_{2,3}$ spectra for two different reciprocal vector (a) g = 200 and (b) g = 110 acquired from ~ 50 nm thick area. Clear dichroic signal is obtained for g = 200 case compared to g = 110. Copyright (2012) by Elsevier [33].

Although the amplitude of 200 reflections is much less compared to 110 reflections, we have nevertheless obtained excellent counts even with higher '*g*' vector. As at least half the extinction distance is required to generate sufficient diffracted beam therefore there is a minimum thickness from which one can acquire optimum dichroic signal and this is simply half the extinction distance. However, for larger g = 200 vector decaying of amplitude due to absorption is small as compared to g = 110 beam. From Fig. 2.8 (b) one can see that EMCD signal for g = 200 Bloch wave does not oscillate rapidly as a function of specimen thickness as compared to g = 110. Fig. 2.9 provides a comparison of experimental dichroic signal between 110 and 200 diffracting vectors at a thickness ~50 nm. The thickness of areas from where signals were acquired was in the range of 30-80 nm. Clear dichroic signal is obtained with *g* = 200 at both the L_3 and L_2 peaks. The dichroic signal for 110 vectors is poor because the optimum thickness is around 20 nm and at this thickness range the amplitude decays rapidly (Fig. 2.8 (a)).

Table 2.1.Various diffracting planes in CrO_2 and corresponding extinction distances. (Using JEMS electron microscopy software, P. Stadelmann, 1999-2009). Copyright (2012) by Elsevier [33].

(h k l)	Extinction Distance (ξ_g) (nm)	d-spacing (Å)	Amplitude (α_g) (per unit cell volume)	Bragg angle (mrad)
100	0.00	0.4419	0.000	2.23
110	65.6419	0.31247	11.63946	3.15
101	120.39357	0.24315	6.34614	4.05
111	129.2782	0.21303	5.90999	4.62
222	147.77462	0.10652	5.17009	9.24
400	179.70273	0.11048	4.25152	8.91
310	202.99686	0.13974	3.76371	7.04
210	204.04537	0.19762	3.74442	4.48
200	271.24716	0.22095	2.81674	4.45
221	449.16247	0.13767	1.70099	7.15

2.2.4 EMCD along Two Different Growth Orientations

EMCD Experiment has been performed with mono probe illumination as described in Sec. 2.2.2 on CrO_2 epitaxial thin films grown along two different growth orientations i.e., (100) and (110) on respective TiO_2 substrates with film thickness ~ 45 nm [10]. Our aim was to understand the response of EMCD signal to these two growth orientations of CrO_2 at room temperature and

whether it is possible to distinguish any difference in the moment values between the two films. Cr L_3 and L_2 peak appeared approximately at 577 and 585.4 eV respectively with peak-to-peak separation energy of about 8.4 eV. EMCD spectra were background subtracted (with an exponentially decaying background function) and interpolated to 2000 points using cubic spline method before analyzing and calculating the orbital and spin moment (m_{orb}/m_{spin}) ratio. Fig. 2.10 shows the Cr $L_{2,3}$ scan for two different films with g = 200 diffracting vector under three beam geometry. Excellent dichroic signal (4-5 %) is obtained at both L_3 and L_2.

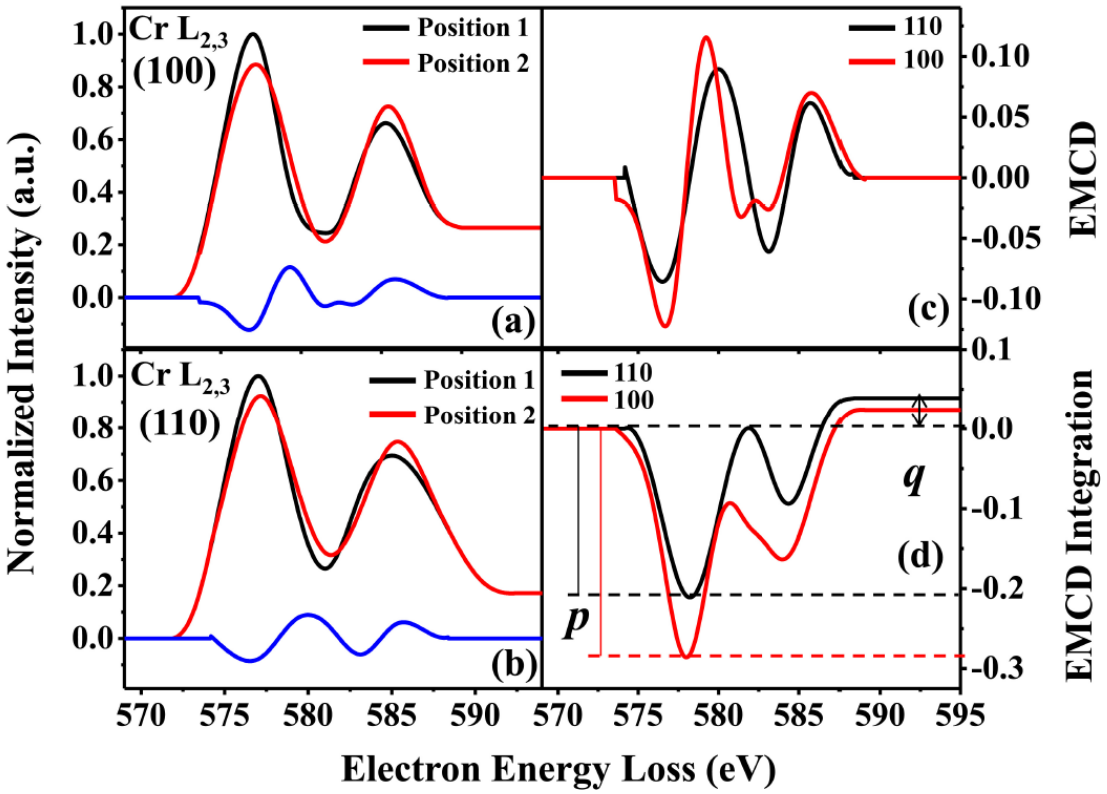

Figure 2.10. Experimental Cr $L_{2,3}$ spectra for two different orientation of CrO_2 thin films, (a) (100) and (b) (110) growth orientation. The Cr L_3, L_2 peaks appear at 577 eV and 585.4 eV showing peak-to-peak separation energy of ~ 8.4 eV. (c) shows the EMCD spectra of both (100) and (110) films and (d) shows the integral of EMCD plot for both the films. Copyright (2012) by Elsevier [33].

Applying the EMCD sum rules on the experimental spectra, we obtained the m_{orb}/m_{spin} to be -0.0155 and -0.0373 for (100) and (110)-oriented films respectively (see Table 2.2). This indicates that the spin moment is smaller for (110) film compared to (100) film (since the orbital moment remains the same for both the films [17,18]). This trend in terms of relative values is in

disagreement with the previous XMCD and Quantum Design Superconducting Quantum Interference Design (SQUID) measurements from a similar set of films [10].

However, for CrO_2 there are some well known issues associated with calculation of magnetic moments using sum rules. One is weak spin orbit coupling in CrO_2 leading to significant spectral overlap between L_3 and L_2 edges resulting in 5-15 % error in the spin sum rules [19,20]. Additionally, the transition is not from pure $p_{3/2}$ and $p_{1/2}$ states rather from a quantum mechanical superposition of states known as **jj** mixing. Moreover, distorted oxygen octahedra of CrO_2 are responsible for significant contributions to dipole moment term, $\langle T_z \rangle$ in the sum rule which is normally ignored during determination of moments in the case of 3*d* elements. To take into account the **jj** mixing effect, a correction factor 2 was used in the estimate of spin moments. But this also led to very high spin moments in the case of CrO_2 (2.4 μ_B per Cr atom) [21]. More accurate determination of moments requires methods such as moment analysis of the spectra i.e., analyzing spectra in terms of different excitation channels, core hole excitation life time as well as consideration of contribution from natural dichroism [18,19,21]. However, mindful of these issues we have continued our analysis using both the EMCD and XMCD sum rules to calculate the orbital to spin moment ratio (as individual determination will involve determination of parameter '*K*' as discussed in Chapter 1.1.2).

Table 2.2. Moments ratio calculated by both EMCD and XMCD sum rules in respective experimentations for two different growth orientation with g = 200. Copyright (2012) by Elsevier [33].

Growth orientation	EMCD sum rules	XMCD measurement		
	(m_{orb}/m_{spin})	(m_{orb}/m_{spin})	m_{orb}	m_{spin}
100	-0.0155	-0.025	-0.03±0.005	1.2±0.2
110	-0.0373	-0.0167	-0.03±0.005	1.8±0.3

2.3 Density Functional Theory based XMCD Calculations

Apart from the discrepancy between the experimental dichroic signal from EMCD (higher for strained film) and XMCD (higher for relaxed film) at room temperature, there is also a discrepancy reported between the experimental Curie temperature and theoretical exchange constant calculated using first principles for strained and strain-free films [8]. The variation of

exchange constant with temperature and internal lattice parameter of oxygen (u_o) are believed to be responsible for such discrepancy. Therefore, we have simulated electron spin-density functional theory based density of states and XMCD spectra under generalized gradient approximation (GGA) in WIEN2k for the case CrO_2 [22]. XMCD spectra can be calculated for any system for which a Wien2k ground-state calculation is carried out. We simulated experimental bulk, GGA relaxed (corresponds to (110) film) and strained lattice (corresponds to (100) film) CrO_2 structures [10]. Oxygen internal lattice parameter (u_o) is relaxed to study its effect on atom specific and net magnetic moments.

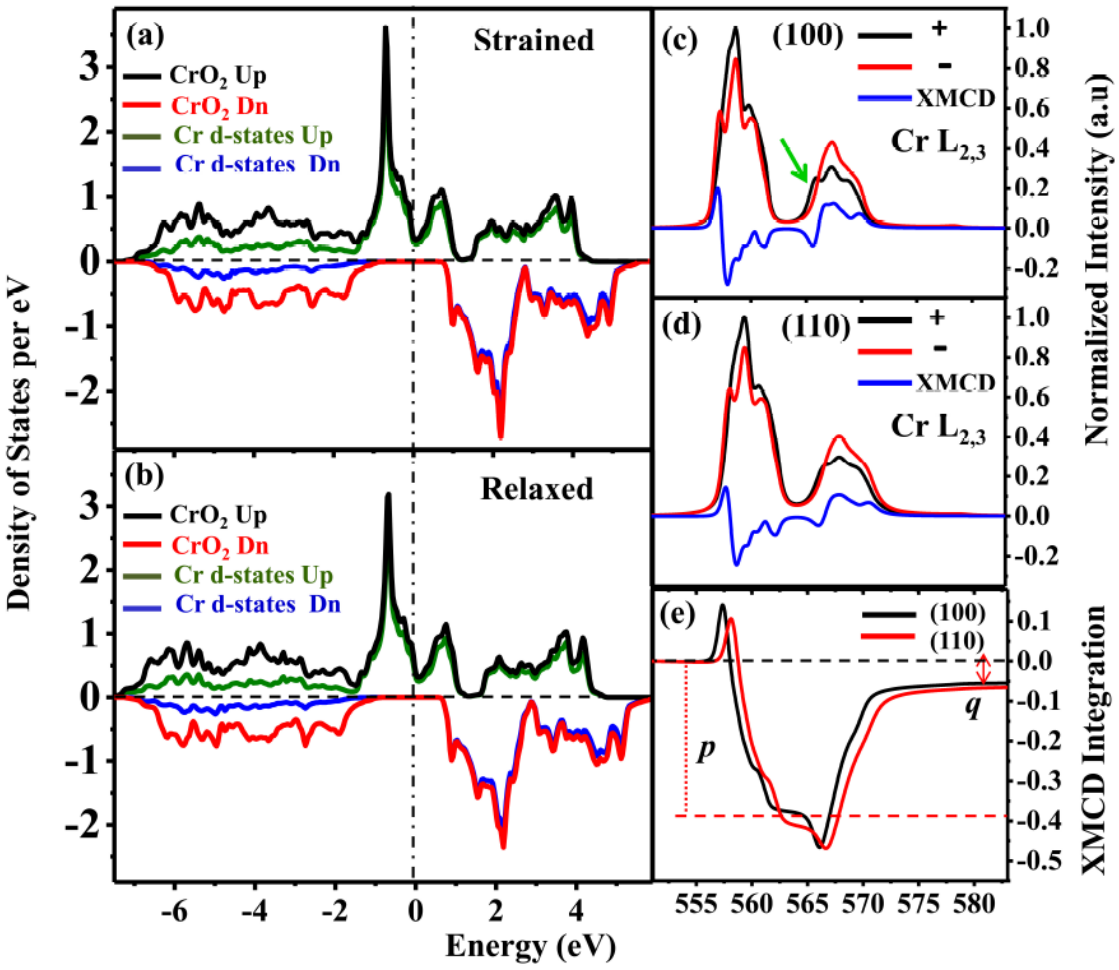

Figure 2.11. Theoretical calculation of XMCD and DOS spectra for both types of CrO_2 films, (a), (c) shows the XMCD and DOS from (100) strained film respectively and (b), (d) shows the XMCD and DOS from (110) relaxed film respectively. (e) shows that integrated XMCD plot for two different films where p and q are found to have same sign. Copyright (2012) by Elsevier [33].

The matrix elements corresponding to the photon absorption cross section with respect to polarization of light and the sample magnetization are calculated within dipole approximation [23,24]. In order to describe core and valence electrons, an all-electron linearized augmented plane wave (LAPW) [25-27] scheme is employed under GGA approximation which is considered to be one of the accurate methods for the description of magnetic properties. We considered a spin-polarized and spin-orbit coupled system as they are recommended for highly correlated electron systems like CrO_2. Orbital dependent potential is introduced to calculate orbital moments along with the spin moments. Dense k-mesh is generated (with 3000 k-points) in the whole Brillouin zone. The X-ray absorption spectra and eigenvalues are evaluated following the procedure given in Ref. 23. The collinear spin arrangement of Cr atoms is assumed though other configuration away from collinear spin arrangement has been reported [28].

2.3.1 Comparison between Calculated and Experimental Spectra

Density of states (DOS) plots shows that both relaxed and strained lattice are half-metallic in character (see Fig. 2.11 (a) and Fig. 2.11 (b)). The total moment at Cr atom is found to be slightly higher (~1.928 μ_B) for strained film as compared to the relaxed (~1.909 μ_B) film with relaxed u_o. Calculated moments show that lattice strain does not have any significant influence on net moments. Table 2.3 summarizes the calculated Cr and O spin and orbital moments. The relaxation of u_o was found to have no significant influence on the calculated moment values. The corresponding XMCD spectra for the strained lattice with relaxed u_o and bulk relaxed lattice are shown in Fig. 2.11 (c) and Fig. 2.11 (d) respectively. The spectra have been convoluted with 0.3 eV and 0.5 eV FWHM Lorentzian at L_2 and L_3 respectively [23]. Different broadenings at L_2 and L_3 are used as the $p_{1/2}$ core-hole has a channel (the *super-Coster-Kronig* process $p_{1/2} \rightarrow p_{3/2}$) which is not available for $p_{3/2}$ and thus experimental L_2 line is wider than L_3 [23,24]. Spectra are finally convoluted with 0.2 eV FWHM Gaussian line shape to account for spectrometer resolution [29].

The peak to peak shift between $L_{2,3}$ majority and minority spin spectra is found to be ~0.1 - 0.2 eV in both experiment and theory leading to crossing of spectra on the sides (as marked by green arrow in Fig. 2.11(c)). This crossing causes EMCD spectra to change sign for the same absorption edge (Fig. 2.11 (c)). Theoretically the integrated XMCD curve for a given

edge is not zero whereas different experimentation show that this may or may not be to zero [10,18,30]. Slight asymmetry is observed in the crossing of the experimental EMCD spectra on both sides of peak and this may have to do with the different energy loss mechanisms and core-hole life time for two different types of spin transitions. The comparison of broadening and asymmetry (i.e. decomposition of FWHM on either side of peak) between experimental EMCD and theoretical XMCD $L_{2,3}$ spectra are shown in Table 2.4. The percentage of dichroic signal obtained from theoretical spectra is ~ 9 - 10 %. Application of sum rules for 3*d* transition metals (without taking into consideration any correction factors for light TM elements) reveals spin moment 1.70 μ_B for (110) film (relaxed) as compared to 1.79 μ_B for (100) film (strained). Orbital moment is found to be ~0.06 μ_B for both the films.

Table 2.3. Calculated moments by DFT and after application of XMCD sum rules on the calculated XMCD spectra. Copyright (2012) by Elsevier [33].

Film growth orientation	DFT calculation				XMCD sum rule applied to DFT calculated spectra		
	Cr m_{spin} (μ_B)	Cr m_{orb} (μ_B)	Om_{spin} (μ_B)	O m_{orb} (μ_B)	Cr m_{spin} (μ_B)	Cr m_{orb} (μ_B)	Cr (m_{orb}/m_{spin})
100 (partially strained film)	1.9285	-0.0328	-0.087	0.0001	1.793	0.062	0.0345
110 (relaxed film)	1.9091	-0.0314	-0.0661	0.0001	1.70	0.064	0.0376

However, the integrals of the XMCD spectra, $p = \int_{L_3} (\mu_+ - \mu_-) d\omega$ and $q = \int_{L_3+L_2} (\mu_+ - \mu_-) d\omega$ have opposite signs in the experimental spectra (as applied to EMCD) whereas they have same sign in the calculated spectra. Application of sum rules on calculated XMCD spectra underestimates moment values as well as the incorrect relative orientation of spin and orbital moment (same sign of *p* and *q* obtained from integrated spectra) compared to DFT calculation. Smaller moment values using sum rules may be due $\langle T_z \rangle$ term negligence, as well as using n_{3d} = 2 without correcting for hybridization. This is showing a clear deviation in the moment values obtained using sum rules applied on either EMCD/XMCD spectra in its simplified form for 3*d* elements as first demonstrated by Wu *et al*. [31,32].

Table 2.4. The comparison of broadening and asymmetry between experimental EMCD and theoretical XMCD $L_{2,3}$ spectra. Copyright (2012) by Elsevier [33].

Spectra	Growth Orientation	$L_{2,3}$ Spin Up(↑)/ Spin Down(↓)	L_3			L_2		
			FWHM (eV)	Asymmetry (eV)		FWHM (eV)	Asymmetry (eV)	
Experimental (EMCD)	100	↑	4.16	2.18	1.98	3.94	1.87	2.07
		↓	4.97	2.42	2.55	3.87	1.87	2.01
	110	↑	4.62	2.31	2.31	5.1	2.31	2.79
		↓	5.27	2.31	2.79	4.08	1.97	2.11
Calculated (XMCD)	100	↑	3.3	1.36	1.94	4.21	2.06	2.15
		↓	3.86	1.79	2.06	3.60	1.36	2.24
	110	↑	3.86	1.43	2.43	4.45	2.05	2.4
		↓	4.23	1.82	2.41	3.94	1.47	2.47

The possible discrepancy between the XMCD and EMCD estimate of moment ratio could result from inherent nature of diffraction based interference origin of dichroic signal in EMCD compared to absorption spectroscopy based XMCD [33]. The trend in the dichroic signal and moment ratio obtained from EMCD between (100) and (110) oriented films is found to be the same for many experimental trials and possible cause could be the effect of strain (in case of 100 film) on the EMCD signal. Strain might affect EMCD signal by changing Debye Waller factor as well as different defect structure in the relaxed film and modify thermal diffused scattering in the diffraction plane non-uniformly (as strain is tensile along *a* direction and compressive along *b* direction, and the diffraction pattern was taken along *c* direction). Additionally, discrepancy between theoretically calculated exchange constant, DFT calculation of magnetic moments (carried out at 0 K and no entropy factor) and experimental Curie temperature may be due to neglecting the entropy factor in the total free energy calculation. As strain energy increases the free energy of the system, therefore the free energy minimization at room temperature demands increase in entropy by randomizing spin orientation in case of strained (100) film relatively more compared to relaxed (110) film and leading to lower Curie temperature. The role of defects in the case of relaxed film which is resulting in higher Cr spin moment and how it affects the

experimental nanoscale EMCD technique also need to be studied to understand the possible reasons for the discrepancy between the XMCD and EMCD calculated moments ratio.

2.4 Conclusions

EMCD experiment has been performed on CrO_2 epitaxial thin films grown along (100) and (110) growth orientations on respective TiO_2 substrates. Mono probe illumination using gun monochromator excitation to acquire EMCD signal improves the signal significantly. An area as small as ~5-10 nm^2 can be accessed with this probe which is essentially a plane wave illumination. Such a parallel probe results in spot like diffraction pattern that is helpful during EMCD signal acquisition under energy spectrum imaging mode. It is found that (200) type of diffracting vector with higher extinction distance allows better EMCD signal from relatively thicker part of the sample. The discrepancy in the moment ratio from XMCD and EMCD is experimental observation, and is independent of the theory used to interpret. Further studies need to be done in applying the EMCD sum rules to calculate the orbital and spin specific magnetic moments particularly in the case of transition metal compounds like CrO_2 where variations in dichroic spectra have been reported in the literature. Also the role of defects in the observed experimental EMCD results needs to be understood.

2.5 Bibliography

[1]. K. Schwarz, J. Phys. F: Met. Phys. 16 (1986) L211.

[2]. J. M. D. Coey, and M. Venkatesan, J. Appl. Physics 91 (2002) 8345.

[3]. S. K. Upadhyay, A. Palanisami, R. N. Louie, and R. A. Buhrman, Phys. Rev. Lett. 81 (1998) 3247.

[4]. A. Anguelouch, A. Gupta, G. Xiao, D. W. Abraham, Y. Ji, S. Ingvarsson, and C. L. Chien, Phys. Rev. B 64 (2001) 180408 (R).

[5]. Y. Ji, G. J. Strijkers, F. Y. Yang, C. L. Chien, J. M. Byers, A. Anguelouch, G. Xiao, and A. Gupta, Phys. Rev. Lett. 86 (2001) 5585.

[6]. R. Meservey, and P. M. Tedrow, Phys. Rep. 238 (1994) 173.

[7]. A. Gupta, X. W. Li, S. Guha, and G. Xiao, Appl. Phys. Lett. 75 (1999) 2997.

[8]. M. Pathak, H. Sato, X. Zhang, K. B. Chetry, D. Mazumdar, P. LeClair, and A. Gupta, J. Appl. Phys. 108 (2010) 053713.

[9]. K. B. Chetry, M. Pathak, P. LeClair, and A. Gupta, J. Appl. Phys. 105 (2009) 083925.

[10]. M. Pathak, H. Sims, K. B. Chetry, D. Mazumdar, P. R. LeClair, G. J. Mankey, W. H. Butler, and A. Gupta, Phys. Rev. B 80 (2009) 212405.

[11]. P. Schattschneider, M. Stöger-Pollach, S. Rubino, M. Sperl, C. Hurm, J. Zweck, and J. Rusz, Phys. Rev. B 78 (2008) 104413.

[12]. J. Verbeeck, C. Hébert, S. Rubino, P. Novák, J. Rusz, F. Houdellier, C. Gatel, and P. Schattschneider, Ultramicroscopy 108 (2008) 865.

[13]. H. Lidbaum, J. Rusz, A. Liebig, B. Hjörvarsson, P. M. Oppeneer, E. Coronel, O. Eriksson, and K. Leifer, Phys. Rev. Lett. 102 (2009) 037201.

[14]. J. Rusz, S. Rubino, and P. Schattschneider, Phys. Rev. B 75 (2007) 214425.

[15]. D. B. Williams, and C. B. Carter, Transmission Electron Microscopy: A Text Book for Materials Science, second ed., Springer, New York, 2009.

[16]. S. Löffler, and P. Schattschneider, Ultramicroscopy 110 (2010) 831.

[17]. M. Komelj, C. Ederer, and M. Fähnle, Phys. Rev. B 69 (2004) 132409.

[18]. E. Goering, A. Bayer, S. Gold, G. Schütz, M. Rabe, U. Rüdiger, and G. Güntherodt, Phys. Rev. Lett. 88 (2002) 207203.

[19]. E. Goering, S. Gold, and A. Bayer, Appl. Phys. A 78 (2004) 855.

[20]. A. Scherz, H. Wende, K. Baberschke, J. Minár, D. Benea, and H. Ebert, Phys. Rev. B 66 (2002) 184401.

[21]. E. Goering, Phil. Mag. 85 (2005) 2895.

[22]. P. Blaha, K. Schwarz, G. K. H. Madsen, D. Kvasnicka, and J. Luitz, WIEN2k: An Augmented Plane Wave + Local Orbitals Program for Calculating Crystal Properties (Karlheinz Schwarz, Techn. Universität Wien, Austria, 2001)

[23]. L. Pardini, V. Bellini, F. Manghi, and C. Ambrosch-Draxi, Computer Phys. Comm. 183 (2012) 628.

[24]. L. Pardini, Ph.D Thesis, University of Modena and Reggio Emilia, 2008.

[25]. D. D. Kölling, and G. O. Arbman, J. Phys. F: Metal Physics 5 (1975) 2041.

[26]. D. J. Singh, and L. Nordstrom, Planewaves, Pseudopotentials, and the LAPW Method, second ed., Springer, Berlin, 2006.

[27]. C. Ambrosch-Draxl, Physica Scripta T109 (2004) 48.

[28]. H. Sims, S. J. Oset, W. H. Butler, J. M. MacLaren, and M. Marsman, Phys. Rev. B 81 (2010) 224436.

[29]. J. E. Müller, J. W. Wilkins, Phys. Rev. B 29 (1984) 4331.

[30]. N. Baadji, M. Alouani, and H. Dreyssé, Euro. Phys. Lett. 87 (2009) 27004.

[31]. R. Wu, D. Wang, and A. J. Freeman, 71 (1993) 3581.

[32]. R. Wu, and A. J. Freeman, Phys. Rev. Lett. 73 (1994) 1994.

[33]. B. Loukya, X. Zhang, A. Gupta, and R. Datta, J. Magn. Magn. Mater. 324 (2012) 3754.

Chapter 3

Quantitative and Site-Specific EMCD of $NiFe_2O_4$ and $CoFe_2O_4$ Spinel Oxide Epitaxial Thin Films

This chapter presents our results on evaluation of 'K' parameter in EMCD sum rules and determination of site-specific spin and orbital moments in technologically important $NiFe_2O_4$ and $CoFe_2O_4$ inverse spinel oxide thin films. A Bloch wave absorption model is presented to evaluate site specific contribution to EMCD signal for the inverse spinel structure.

This work has been published in the following journals.

- ✓ *Physical Review B 91 (2015) 134412. Copyright (2015) by American Physical Society.*
- ✓ *Journal of Applied Physics 116 (2014) 103505. Copyright (2014) by American Institute of Physics.*
- ✓ *Journal of Crystal Growth 345 (2012) 44. Copyright (2012) by Elsevier.*
- ✓ *Journal of Crystal Growth 390 (2014) 61. Copyright (2014) by Elsevier.*

3.1 Introduction

Electron Magnetic Circular Dichroism (EMCD) is an element specific bulk sensitive magnetic characterization technique in a Transmission Electron Microscope (TEM) for the evaluation of orbital (m_L) and spin (m_S) magnetic moments at nanoscale [1-4]. Indeed, with suitable theoretical guidelines atomic-scale information can be obtained [5,6]. Though there are several reports on its development and applications to various materials, the technique is still confined to the evaluation of moment ratio (m_L/m_S) values [4,7,8]. This is due to the fact that the EMCD signal is dependent on a number of factors, primarily the choice of reciprocal lattice vectors, specimen thickness and '*K*' parameter etc. [3,9]. Without precise determination of these parameters it is practically impossible to determine the individual m_L and m_S values for a given material using the EMCD sum rules. The present chapter discusses on the site-specific quantitative EMCD (evaluation of individual m_L and m_S values) of two different ferromagnetic spinel oxides, namely $NiFe_2O_4$ (NFO) and $CoFe_2O_4$ (CFO). A phenomenological model based of Bloch wave absorption was developed to evaluate site specific magnetic moments for the inverse spinel structure.

3.2 Thin Film Growth, Structural and Optical Properties of NFO and CFO

Nickel Ferrite ($NiFe_2O_4$) and Cobalt Ferrite ($CoFe_2O_4$) are well-known and technologically important materials due to their attractive properties. These are ferrimagnetic insulators (semiconductors) with inverse spinel structures. Wide range of applications of these materials is possible due to their high curie temperatures of 850 K and 800 K for $NiFe_2O_4$ and $CoFe_2O_4$, respectively. $NiFe_2O_4$ has applications in microwave integrated devices [10], magnetoelectric coupling heterostructures [11-13], and active barrier material for emerging class of spintronic devices known as spin filters [14-16]. These are possible due to its high Curie temperature, large exchange splitting, and potentially large tunnel magneto-resistance effect. $CoFe_2O_4$ has relatively large magnetic anisotropy, moderate saturation magnetization, remarkable chemical stability and good mechanical hardness.

Atomically smooth epitaxial thin films of $NiFe_2O_4$ and $CoFe_2O_4$ were grown on $MgAl_2O_4$ substrates by Direct Liquid Injection – Chemical Vapor Injection (DLI-CVD) method developed at University of Alabama [17,18] were studied in this quantitative EMCD experimentation. CVD method offers a number of advantages over other deposition methods such as, large area

deposition, excellent step coverage and relatively high growth rates. DLI-CVD technique, which can generate a vapor from a liquid solution at relatively low temperatures (<200 ºC) is particularly useful method for multi component systems as several precursors can be dissolved in the same solution and relative delivery rates of precursors are defined by the solution composition. NFO and CFO films used in EMCD studies are grown on <100> oriented $MgAl_2O_4$ (MAO) substrate at 800 °C and 690 °C temperatures respectively.

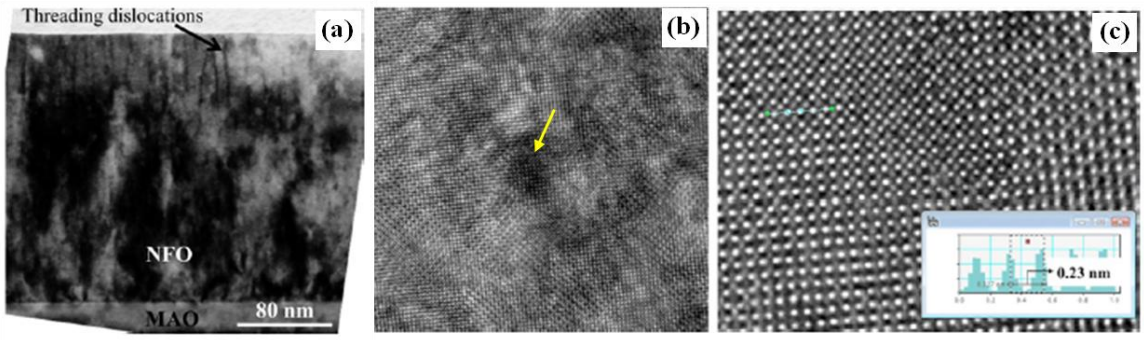

Figure 3.1.(a) TEM cross-sectional diffraction contrast image from NFO grown on MAO substrate. Threading dislocations are marked in the image. (b) High resolution TEM image from dark diffused contrast area and (c) magnified view of (b). Copyright (2014) by American Institute of Physics [19].

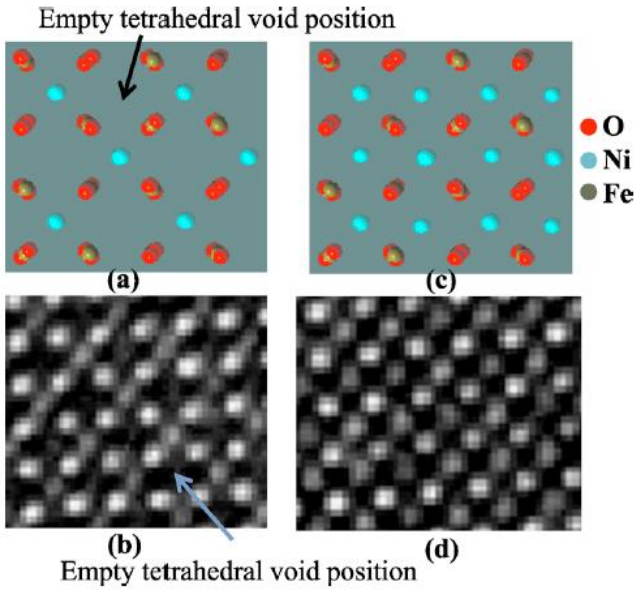

Figure 3.2. (a) and (b) are the schematic of spinel NFO structure and corresponding HRTEM image. (c) and (d) are the schematic and HRTEM image from two different antiphase domains in projection. . Copyright (2014) by American Institute of Physics [19].

The microstructural investigation of these films done previously by transmission electron microscopy revealed that along with the presence of threading dislocations (Fig. 3.1 (a)) there are also certain regions of dark diffused contrast areas as shown in Fig. 3.1 (b). High resolution Transmission Electron Microscopy (HRTEM) performed on these dark contrasted areas revealed that these areas consisted either two different antiphase domains along the beam direction or due to the presence of A-site cation defects as shown in Fig. 3.1 (c) [19-21]. The schematic ideal spinel structure of NFO along <100> zone axis is shown in Fig. 3.2. The octahedral and tetrahedral atom positions are indicated in Fig. 3.2 (a) and Fig. 3.2 (b) shows the corresponding high resolution TEM image. Fig. 3.2 (c) and Fig. 3.2 (d) schematic structure and high resolution image of the regions with two different anti-phased domains in projection. Fig. 3.2 (d) is the view of atomic arrangement from a region where two different domains with ¼<110> translation vectors are superimposed. Apart from the presence of antiphase domains, these structures are also found to have A-site cation vacancy regions as shown in Fig. 3.3. Regions X and Y in Fig. 3.3 indicate the regions of A-site cation defects and regular inverse spinel structure with alternate tetrahedral sites filled respectively in both NFO and CFO.

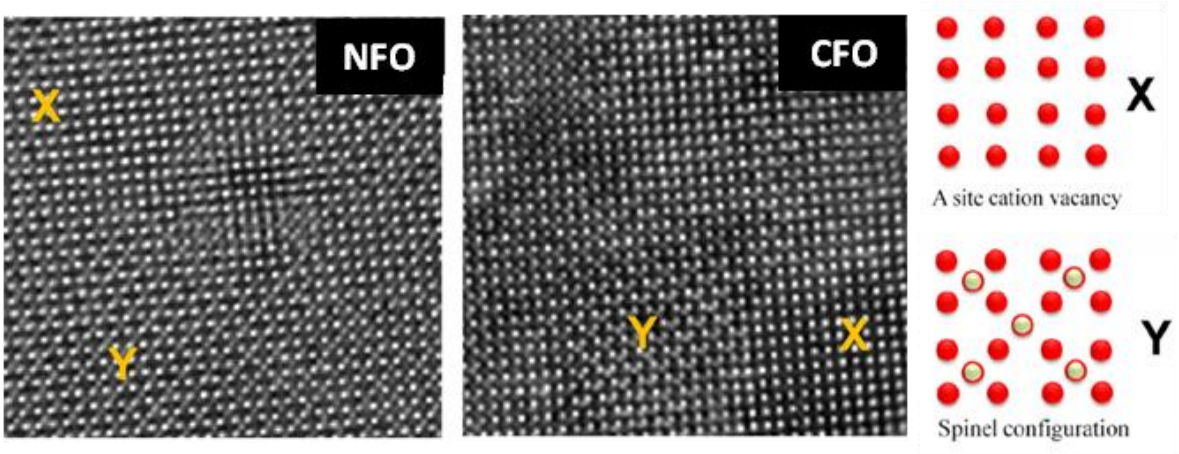

Figure 3.3. High resolution TEM image showing the tetrahedral A site cation vacancy regions (marked as X) along with regular lattice structures (marked as Y) from NFO and CFO along the <100> zone axis. For regular periodicity, alternate tetrahedral sites are vacant (schematic Y) but for A site vacancy regions, atoms are missing from the tetrahedral sites (schematic marked as X). Copyright (2014) by American Institute of Physics [21].

We also have performed HAADF-STEM (High angle annular dark field-scanning transmission electron microscopy) imaging as shown in Fig. 3.4 to characterize the local atomic arrangement of as-deposited NFO films [20]. The marked regions A and B indicate the two different atomic arrangements in this structure. In the area A, alternate tetrahedral voids can be observed to be filled and in the area B, no tetrahedral voids are filled. This may be correlated with the dark diffused contrast observed in HRTEM images shown in Fig. 3.1 and Fig. 3.2. This different atomic arrangement has origin at the film-substrate interface. Such structural deviations and different cation arrangements can influence the optical and magnetic properties of these materials.

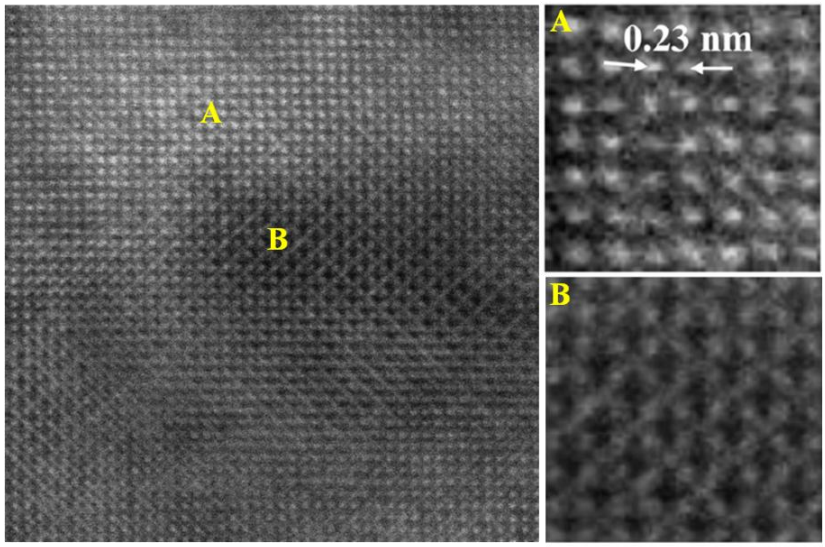

Figure 3.4. STEM-HAADF image from NFO grown on PZN-PT substrate. A and B are two regions where cations have different arrangements. Only octahedral positions are filled in region A whereas usual alternate tetrahedral positions are observed to be filled in region B. Copyright (2012) by Elsevier [20].

Nanoscale optical absorption spectroscopy studies by spatially resolved high resolution electron energy loss spectroscopy (HREELS) have been performed on these films from dark diffused contrasted regions [21]. Experimentally, both NFO and CFO show indirect/direct band gaps around 1.52 eV/2.74 eV and 1.3 eV/2.31 eV respectively corresponding to the ideal inverse spinel configuration with considerable standard deviation in the band gap values for CFO due to various levels of deviation from the ideal inverse spinel structure. Direct probing of the regions

in both the systems with tetrahedral A site cation vacancy regions shows significantly smaller band gap values.

3.3 Experimental Methods and Computational Details

TEM cross-sectional and plan view samples were prepared by conventional mechanical polishing and then Ar ion milling as already discussed in Chapter 2.2.1. Experiments were performed in a FEI TITAN^{3TM} 80-300 kV aberration corrected TEM with monochromatic probe illumination. Monochromatic probe significantly improves the signal to noise ratio as already discussed in Chapter 2.2.2. [7]. 2-beam geometry (2BC) was used for EMCD experimentation because for sufficiently smaller and larger window size, i.e. $0.25g \times 0.25g$ and $0.5g \times 0.5g$ (g represents the reciprocal lattice vector), which ensures m_L/m_S ratio similar between 2BC and 3BC geometry[4]. Moreover, working with 2BC geometry is found to result in higher dichroic signal obtainable due to equal amplitude of the direct and diffracted beams unlike the 3-beam (3BC) case where EMCD signal reduces due to the unequal amplitudes of the direct and the two diffracted beams and decrease in the magnitude of the imaginary part of mixed dynamic form factor.

Ferrimagnetic $NiFe_2O_4$ and $CoFe_2O_4$ inverse spinel structures were considered for calculating the density of states and the site specific magnetic moment on each atom along with total magnetic moment in Wien2k [22]. The cohesive energies were calculated for different structural configurations with varying cation distributions [21]. Spin-polarized and spin-orbit coupled system with orbital polarization are considered to enable the calculation of both spin and orbital moments. A dense 14×14×14 k-mesh is used for integration of the Brillouin zone based on tetrahedron integration scheme. The system lattice parameters are fully relaxed by using GGA-PBE exchange correlation functional with self-consistent field cycles performed until the energy and charge values are below the convergence criterion of 0.0001 Ry and 0.001 e respectively. Force minimization is performed to ensure the forces between the atoms to be below 1 mRy/bohr. PBE-GGA functional cannot predict the exact excited state properties. So the recent method development by F. Tran and P. Blaha [23,24] to calculate the exact excited state properties, known as the 'modified Becke-Johnson' exchange correlation potential (mBJLDA), has been used to correct the band gap in these systems. This method is more accurate and comparatively less compute-intensive. It was found that NFO exists in inverse spinel structure

while CFO is susceptible to structural changes with cation mixing and A-site cation vacancies. The calculated atom and site-specific magnetic moments are listed in Table 3.1 that will be referred for interpreting experimental EMCD results.

The X-ray magnetic circular dichroism (XMCD) spectra are simulated using WIEN2k code following is same procedure as described in Chapter 2.3. We have carried out XMCD calculation instead of EMCD as the latter has so far not been implemented within the WIEN2k code and there should not be any significant difference in the percentage dichroic signal between the two as the cross section expression for both are equivalent within the dipole approximation except in terms of the magnitude for the individual spectra [1, 2]. The spin and orbital moments and their ratio are evaluated from the calculated spectra using the XMCD sum rules [26,27] and are compared with the DFT predicted values as given in Table 3.2.

3.4 Results and Discussion

3.4.1 Dichroic Signal from Theory and Experiment: Discrepancy in the Magnitude

We consistently observed two important characteristics in the experimental EMCD spectra. Firstly, the experimentally obtained percentage dichroic signal is always smaller than that obtained from the first principle based calculations. Secondly, the absolute dichroic signal percentage measured by the ratio between the dichroic signals at an individual edge to the total sum signal is always much smaller for L_2 edge as compared to that at the L_3 edge for the investigated range of thicknesses (as indicated by C and D respectively for percentage dichroic signal at L_3 and L_2). Figure 3.5 shows an example experimental EMCD spectra in NFO for g = 400 diffracting vector along with the theoretical XMCD spectra. Table 3.1 is the summary of the magnetic moments obtained using the EMCD sum rules applied on the experimental spectra, XMCD sum rules applied on the calculated XMCD spectra and moments obtained directly from DFT calculations. From Fig. 3.5 (b) & (c) we observe that theoretically, we obtained essentially equal percentages of dichroic signal at L_3 and L_2 edges in the case of NFO. But the experimentally observed signal at each edge is much lower than the theoretical prediction and moreover the signal at L_2 is always lower than that at the L_3 edge. However, the magnitude of dichroic signal depends on the available density of states and the transition probabilities.

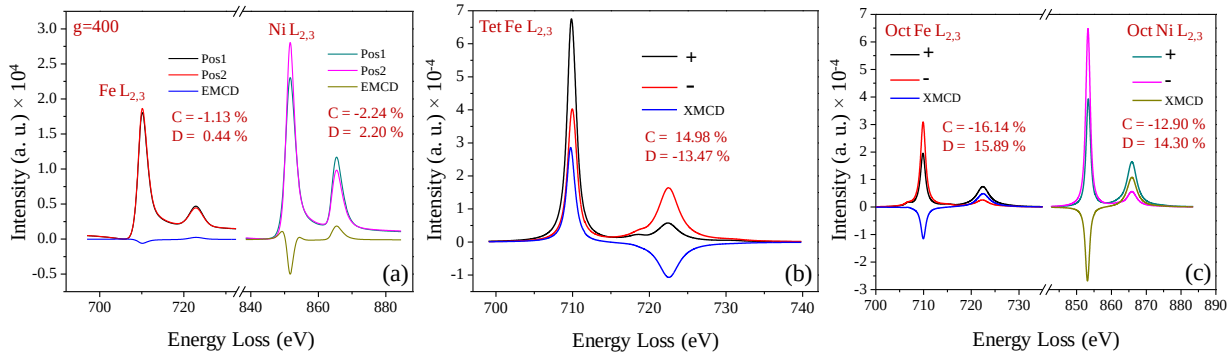

Figure 3.5. (a) Experimental example EMCD $L_{2,3}$ spectra and dichroic signal for Fe at both tetrahedral and octahedral and Ni at octahedral sites in $NiFe_2O_4$. C and D are the % dichroic signal with respect to total sum at L_3 and L_2 edge, respectively. (b) and (c) are that theoretical XMCD plots for atoms at the two sites. The graph shows discrepancy between experimental and theoretical EMCD percentage in terms of magnitude of signals and imbalance between L_2 and L_3 dichroic signal. Copyright (2015) by American Physical Society [38].

Table 3.1: Orbital (m_l) and spin (m_s) specific moment values for NFO obtained from the experimental results on NFO and CFO and by applying XMCD sum rules on the calculated XMCD spectra and from the density functional theory based (WIEN2k) calculations, for ideal inverse spinel configuration. The experimental moment values for Oct Fe is not corrected for signal mixing from A site Fe but corrected for the imbalance due to particular momentum selection direction. Copyright (2015) by American Physical Society [38].

Structure		EMCD sum rules applied on expt. spectra (μ_B/atom)		XMCD sum rules applied on cal. spectra	From Wien2k calculation (μ_B/atom)		
		m_L	m_S	m_L/m_S	m_L	m_S	m_L/m_S
NFO	Tet Fe	--	--	0.0240	0.0075	4.1142	0.00180
	Oct Ni	--	--	0.0223	-0.0500	-1.8031	0.02770
	Oct Fe	-0.0061	-0.2772	0.0034	-0.0070	-4.2076	0.00160
CFO	Tet Fe	--	--	0.0238	0.0076	4.1290	0.00180
	Oct Co	--	--	0.0130	-0.0408	-3.6727	0.01110
	Oct Fe	-0.0190	-0.8563	0.0194	-0.0081	-4.1928	0.00193

The experimentally observed low dichroic signal can be understood from the Bloch wave electron propagation and its absorption through the crystal. The imbalance in the dichroic signal at L_3 and L_2 is a result of the EMCD spectra acquisition selecting a particular momentum transfer

direction away from the direct beam. Such experimental issues can lead to inaccuracies in the quantitative evaluation of moments. Also, there are earlier reports claiming the percentage dichroic signal for NFO as high as 33% for Fe and 42% for Ni, though the authors did not address on the maximum observable limit [28] and this should not exceed the theoretical values. EMCD has not been widely used experimentally most likely due to these practical issues not having been addressed previously.

3.4.2 Dependence of EMCD Signal on Sample Thickness

As already discussed in Chapter 1, EMCD is an electron diffraction based technique [29] where a pair of equally intense Bragg spots corresponding to direct and diffracted beams are chosen for the simultaneous and perpendicular momentum transfer at two different positions, which are opposite to each other in the diffraction plane (see Fig. 3.6). These pair of diffraction spots (0 & g) that are phase shifted by $\pi/2$ and with perpendicular momentum transfer, represented by $q \pm i.q'$ (equivalent to opposite helicity of incoming photons, $\varepsilon \pm i.\varepsilon'$) drive the spin selected transitions from $p \rightarrow d$ states ($\Delta l = \pm 1$ and $\Delta m = \pm 1$).

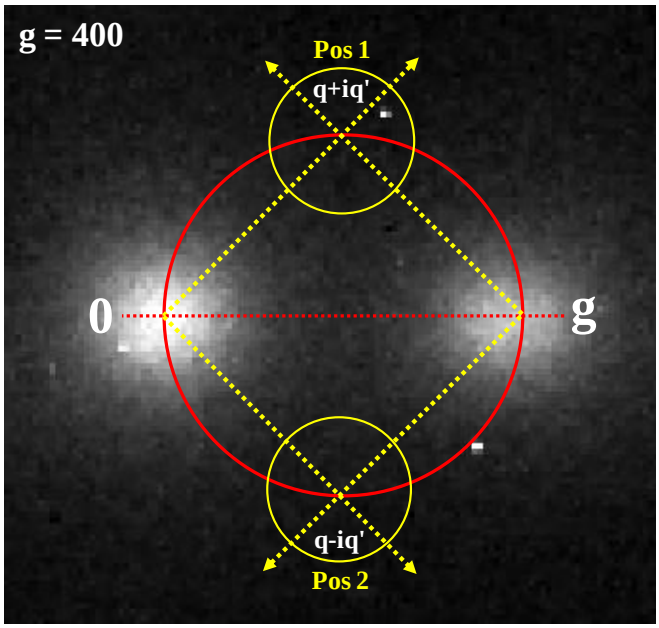

Figure 3.6. EMCD experimental geometry showing perpendicular momentum transfer simultaneously by the direct and one of the diffracted beams (in this case g = 400) under two beam excitation. Simultaneous momentum transfer at two opposite positions represented by q±i.q´ is equivalent to two different helicity of incoming photons as ε±i.ε′ in case of XMCD. Copyright (2015) by American Physical Society [38].

The incident electron beam behaves as Bloch waves due to the periodic crystal potential and its propagation amplitude oscillates with the crystal thickness [30,31]. Inelastic absorption of Bloch waves by the crystal under appropriate geometric condition (e.g., two or three beam orientation) is responsible for the resultant EMCD signal. Quantitative moment analysis needs evaluation of '*K*' parameter (Eq. 1.8) in the EMCD sum rules to obtain m_L and m_S separately. The oscillation or pendellosung phenomenon of Bloch wave propagation in the crystal results in oscillation of '*K*' with the sample thickness. Fig. 3.7 shows the oscillation of direct and diffracted beam amplitudes as a function of thickness for g = 400 (extinction distance ξ_g = 95.51 nm, for NFO) considering the phenomenological absorption (i.e., ξ'_g = 10 ξ_g) [31]. This also results in variation of '*K*' parameter with the sample thickness. '*K*' has been evaluated under two beam geometry according to the equation provided in Ref. 3 and is evaluated for two beam geometry under dynamical theory of diffraction as discussed in Chapter 1.1.2. It varies between 0 and 3 and value of '*K*' is maximum at which direct and diffracted beams amplitudes are equal.

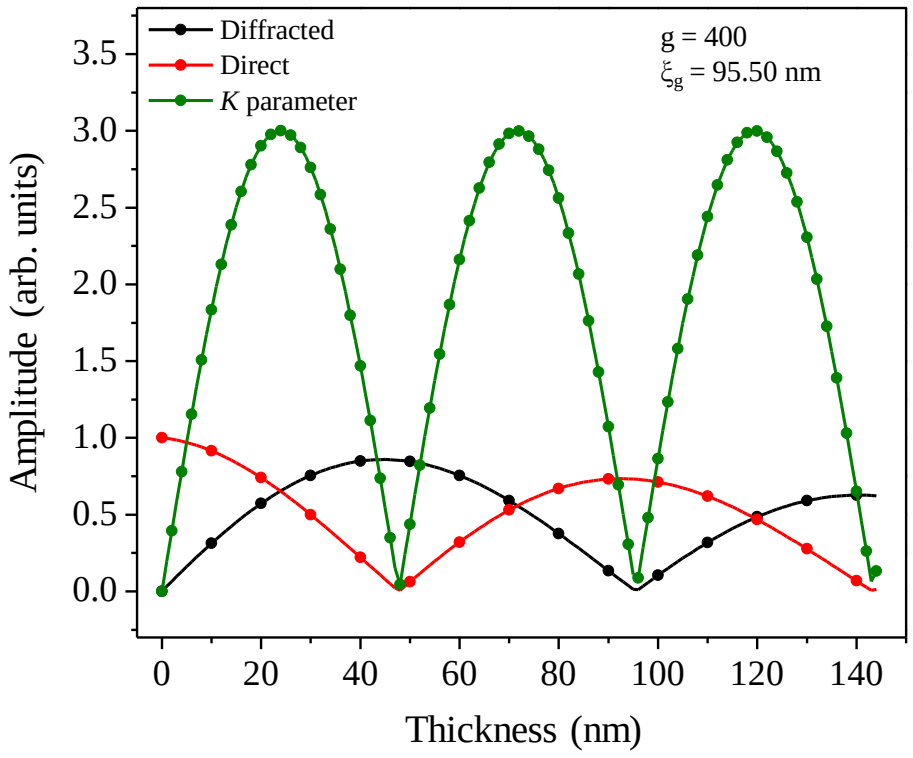

Figure 3.7. Direct and diffracted beam oscillations as they propagate through the sample thickness for g = 400 of NFO. Variation of K parameter with thickness is also shown. The extinction distance is ξ_g = 95.51 nm. Copyright (2015) by American Physical Society [38].

Therefore, it is clear that for most of the thicknesses the amplitude of direct and diffracted beams and thus '*K*' are not the same during EMCD experiment (see Fig. 3.7) and this results in variation of dichroic signal with sample thickness. For $K = 3/2$, XMCD and EMCD sum rules become equivalent. For '*K*' greater or lower than 3/2, there will be a concomitant increase or decrease in percentage of EMCD signal. Therefore, in order to explain the experimentally observed low dichroic signal, one need to consider the thickness averaged '*K*' as well as thickness averaged percentage dichroic signal. We can understand this by carefully considering the oscillating nature of the Bloch wave and its absorption through the sample thickness. It is the absorption of the elastic Bloch waves that gives rise to inelastic signal (mostly comprised of phonons, plasmons and electronic excitations). A small fraction of this inelastic signal gives rise to the $L_{2,3}$ absorption edge. Phenomenological absorption, which is a measure of the probability of inelastic scattering varying with sample thickness with all other parameters (e.g., exposure time) being constant, for both the direct and diffracted beams is plotted in Fig. 3.8 (a). This approach is similar to the treatment by Dudarev *et al* [32] but differs from the single electron Bloch wave treatment developed by Schattschneider *et al* [33]. Bloch wave model in this case is limited as it considers only the interference terms, which is only a small fraction of the inelastic waves taking part in the event and requires placing the detectors following the symmetry of the outgoing waves while phenomenological treatment considers signals in terms of the scattering cross section. It is also possible to trivially consider the thickness dependence of absorption. Both treatments yield essentially similar site-specific signal from spinel oxides and will be discussed further in section 3.4.4.

Now, to understand how the EMCD signal vary with the sample thickness in terms of difference and its percentage with respect to the sum, let us first look at the cross section at two positions in the reciprocal space. The cross sections under two beam geometry (with incident waves as plane waves) at position 1 (+) and position 2 (-) are given by:

$$\sigma_{\pm}(E) = \frac{\partial^2\sigma((q \pm iq'),E)}{\partial E \partial \Omega} = C\left\{\left|\langle \psi_f | q\cdot r | \psi_i \rangle\right|^2 + \left|\langle \psi_f | q'\cdot r | \psi_i \rangle\right|^2 \pm 2i\langle \psi_f | q'\cdot r | \psi_i \rangle\langle \psi_i | q\cdot r | \psi_f \rangle\right\}\delta\left(E_i - E_f + E\right)$$

$$= C\left\{\frac{S(\vec{q},\vec{q},E)}{\vec{q}^4} + \frac{S(\vec{q}',\vec{q}',E)}{\vec{q}'^4} \pm 2i\frac{S(\vec{q},\vec{q}',E)}{\vec{q}^2\vec{q}'^2}\right\}\delta\left(E_i - E_f + E\right) \qquad \ldots (3.1)$$

where, $C = \frac{4\gamma^2 k_f}{a_0^2 k_i}$, γ is the relativistic factor, a_0 Bohr radius, k_i and k_f are wave vectors before and after the interaction respectively. $\sigma_{\pm}(E)$ is the differential scattering cross section for two different momentum transfer directions, $\frac{\partial^2\sigma}{\partial E \partial \Omega}$ double differential scattering cross section, $\vec{q}$ and $\vec{q}'$ are the π/2 dephased momentum transfer vectors, r is the position vector, ψ_i and ψ_f are the initial and final state wave functions, $\delta\left(E_i - E_f + E\right)$ is the Delta function that ensures the selected transition probability, $S\left(\vec{q},\vec{q},E\right)$ and $S\left(\vec{q}',\vec{q}',E\right)$ are the dynamic form factors (DFF) for momentum transfer vectors $\vec{q}$ and $\vec{q}'$ respectively and $S\left(\vec{q},\vec{q}',E\right)$ is the mixed dynamic form factor (MDFF). Therefore, dichroic signal and the sum at these two positions can be derived as given by Eq. 3.2 & Eq. 3.3 respectively.

$$\triangle\sigma = \sigma_+\left(E\right) - \sigma_-\left(E\right) = 4\frac{4\gamma^2 k_f}{a_0^2 k_i}\beta\,\mathrm{Im}\left(\frac{S\left(\vec{q},\vec{q}',E\right)}{\vec{q}^2\vec{q}'^2}\right)\delta\left(E_i - E_f + E\right) \qquad \ldots (3.2)$$

$$\sigma_+\left(E\right) + \sigma_-\left(E\right) = 2\frac{4\gamma^2 k_f}{a_0^2 k_i}\left(a_1^2\frac{S\left(\vec{q},\vec{q},E\right)}{\vec{q}^4} + a_2^2\frac{S\left(\vec{q}',\vec{q}',E\right)}{\vec{q}'^4}\right)\delta\left(E_i - E_f + E\right) \qquad \ldots (3.3)$$

where, a_1 and a_2 are the amplitudes of the direct and diffracted beams, and $\beta = 2a_1a_2$. We consider varying amplitudes for both the direct and diffracted beams, which is in fact the practical situation.

In the spin and orbital EMCD sum rules as already presented in Chapter 1, if '*K*' varies, then there has to be readjustment in the left hand side of Eqs. (1.4) & (1.5) accordingly, as the expectation values remains constant as these are related to the property of the material. Figure 3.8 (a) shows absorption of direct and diffracted beams as a function of thickness through the variation of a_1 and a_2 (for g = 400) (the calculation is dynamical and performed for two beam geometry). Fig. 3.8 (b) shows the variation in the percentage dichroic signal with sample thickness (Fig. 3.8 (b)). The thickness averaged dichroic signal is also shown in the same figure. We observe from this plot that for very small thickness there is a linear increase in the average dichroic signal percentage value up to 30 nm, which is ~ 0.3 ξ_g and beyond this, the average

dichroic signal does not vary strongly. In fact, experimentally we observed essentially the same trend where the dichroic signal does not vary significantly for higher thicknesses. Therefore, for a given thickness the experimental percentage dichroic signal is the integrated average over the thickness, and the net resultant signal will be reduced as compared to the theoretical value. This also signifies the advantage in using the EMCD technique due to its insensitivity to the thickness beyond a certain value determined by the choice of the reciprocal lattice vector. The graph shown in Fig. 3.8 (b) can be considered only as an indication of the trend in the variation of the signal with thickness but the absolute numbers can be calculated by evaluating the exact DFF (dynamic form factor) and MDFF (mixed dynamic form factor) for a given transition process. The variation of '*K*' parameter and its thickness average is shown in Fig. 3.8 (c). The individual EMCD sum rules should therefore be modified accordingly after averaging over the sample thickness to obtain correct spin and orbital moments.

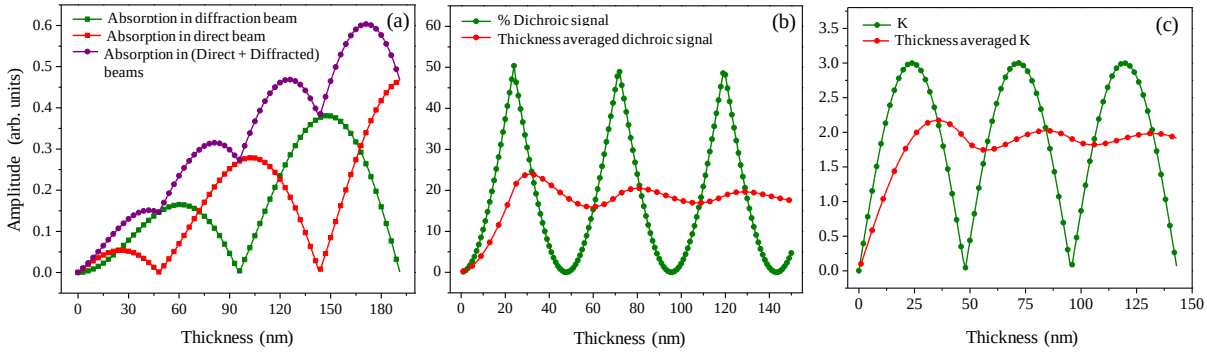

Figure 3.8. (a) Absorption part of both direct and diffracted beams (g = 400) along with total absorption as a function of sample thickness for g = 400 of NFO under two beam orientation. Oscillation and thickness averaged (b) % dichroic signal (with respect to total sum), this has been plotted considering equal amplitude of either direct or diffracted wave whenever they occur with sample thickness and (c) K parameter with sample thickness are shown. Both % dichroic signal and K parameter become almost flat beyond a certain thickness thus favoring experimental evaluation of moment values. Copyright (2015) by American Physical Society [38].

3.4.3 Dependence of EMCD Signal on Momentum Transfer Direction

The other characteristic feature that we observed is that the experimental dichroic signal percentage with respect to the total sum at L_2 edge is always lower compared to L_3 edge for both the NFO and CFO films investigated in this study. For a given thickness, approximately 3-4

times more signal in terms of percentages can be observed for L_3 edge as compared to L_2 edge (see Fig. 3.5 (a)). The reason behind this is related to the detection of EMCD signal along a particular momentum transfer direction with a small collection aperture.

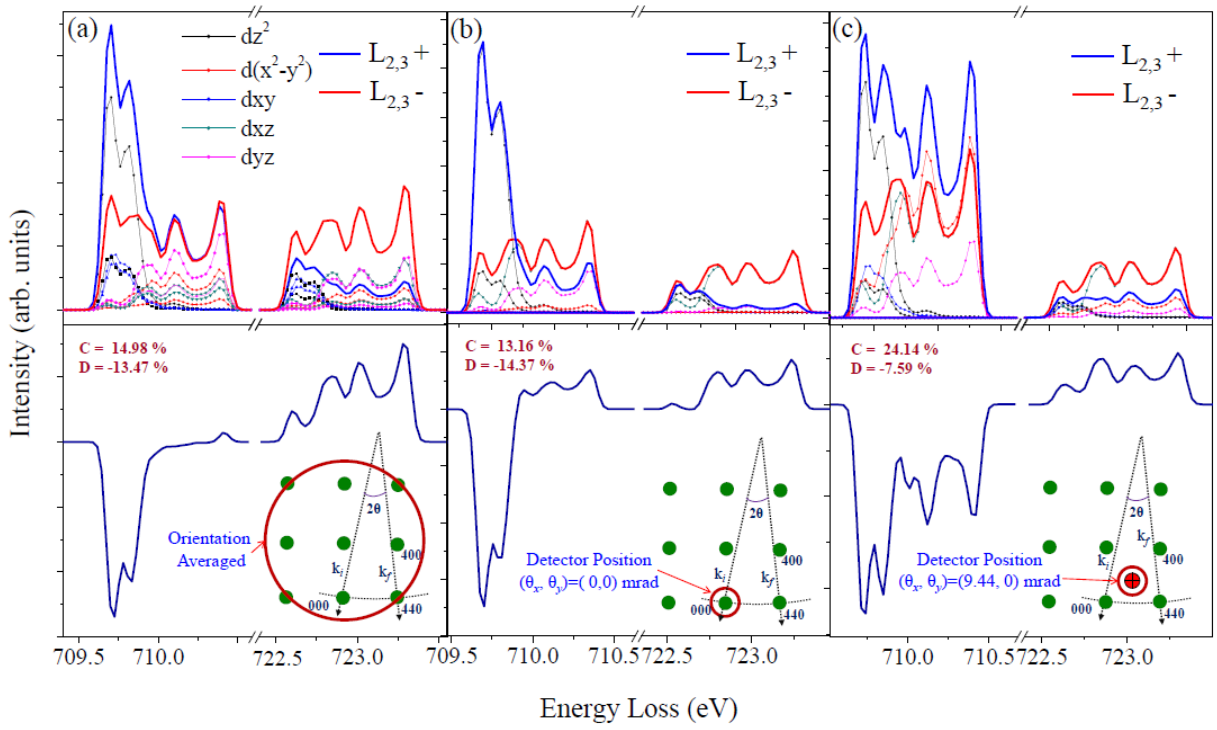

Figure 3.9. (a) Orientation-averaged theoretical EMCD spectra along with relative orbital contributions for Fe_{tet} site in NFO with g = 440 diffracting condition. (b) Momentum resolved EMCD with incoming beam parallel to z axis of the crystal and detector position at (θ_x, θ_y) = (0.0, 0.0) with 2 mrad collection aperture. (c) Momentum resolved EMCD for detector position at (θ_x, θ_y) = (9.44, 0.0), which is typically one of the EMCD aperture positions, with same 2 mrad. collection aperture. One can observe the development of imbalance in EMCD signal between L_3 and L_2 edges. Similar observations were made for atoms at other sites, e.g., Fe_{Oct} and Ni_{Oct} and the details are given in supporting information. Copyright (2015) by American Physical Society [38].

We know that EELS is the measure of projected density of unoccupied states in the diffraction plane. Depending on the location of the detector, different types of anisotropic empty state information will be obtained. For example, it is well known from momentum resolved EELS experiments that if the detector is placed around the Bragg beams then the signal is obtained mostly along the $q \| z$ projected orbitals [33]. On the other hand, if the detector is placed

at some locations other than the Bragg beams, or if the sample is tilted significantly from the incoming beam direction, then the information is predominantly obtained from the perpendicular orientation governed by the *q.r* quantity. For a typical EMCD set up, the *z* and the beam direction are almost parallel, with a slight sample tilt (~4°) to achieve two-beam geometry. For $p \rightarrow d$ transitions ($L_{2,3}$ absorption edge), L_3 is mostly composed of transitions from $p_{3/2}$ to $d_{5/2}$ + $d_{3/2}$ and L_2 is due to transitions from $p_{1/2}$ to $d_{3/2}$ states following $\Delta l = \pm 1$and $\Delta m = 0$ selection rules corresponding to linearly polarized beam. However, for dichroic transitions the selection rule is modified to $\Delta l = \pm 1$and $\Delta m = \pm 1$.

In order to calculate the contributions from projected partial empty *d*-DOS for different momentum selected signal detection, we have taken the following approach. We have first calculated the various partial *d*-DOS contributions to the orientation averaged XMCD or EMCD spectra. The XMCD and EMCD cross sections become equivalent under dipole approximation with $\varepsilon.r$ for X-ray which means with $q.r$ for electrons as discussed in Chapter 1.1.1. The difference between the two absorption cross sections corresponding to two different helicity of X-ray photons i.e., $\varepsilon \pm i\varepsilon'$ or momentum transfer vectors, $q \pm iq'$ for electrons equivalently gives the information on dichroic signal. It is this mathematical equivalence or resemblance between the two equations which makes EMCD similar to XMCD under specific diffraction geometry. The theoretical spectra should look similar for the two cases but the absolute values may differ because of different units and pre-factors used in the respective cross sections formula. Therefore, any attempt to calculate mixed dynamic form factor $S(q,q',E)$ in EMCD sum rules must yield similar results as in case of X-ray following $\Delta l = \pm 1$and $\Delta m = \pm 1$ selection rules for circularly polarized photons. $S(q,q',E)$ can also be evaluated from the knowledge of X-ray cross-sections equations given in Ref. 3. After evaluating the partial *d*-DOS contributions to the orientation averaged EMCD spectra, we have evaluated the matrix elements required to calculate the EMCD spectra at two different positions as shown in Fig. 3.9. This is based on the theory already explained in Ref. 33 and implemented in WIEN2k for $\Delta l = \pm 1$ and $\Delta m = 0$ selection rule applicable for linearly polarized case. However, when we evaluate matrix elements considering, $\Delta l = \pm 1$and $\Delta m = \pm 1$ selection rule we can calculate the partial *d*-DOS contributions to the EMCD spectra. Cross DOS terms are important but we found that their contribution is negligible for the case of the present material. Figure 3.9 (a) shows the calculated orientation-averaged

dichroic signal for tetrahedral Fe in NFO with partial DOS contributions included. The calculation is performed manually by selecting density of states for the specific spin-selected transitions mentioned above. Figure 3.9 (b) & 3.9 (c) show how the partial DOS contribution to the spectra (for tetrahedral Fe site) change in going from the orientation-averaged spectra to aperture positions (θ_x, θ_y) = (0.0, 0.0) mrad around the direct Bragg beam and at (θ_x, θ_y) = (9.44, 0.0) mrad for one of the two typical EMCD aperture positions for g = 440 orientation. The projected amplitude of the individual partial components on the *x*-*y* (or *a*-*b*) plane will be anisotropic and different for different orbitals. The percentage dichroic signal for each orientation is mentioned in the respective figures and one can notice the evolution of imbalance in percentage dichroic signal over L_3 and L_2 edges. We have carried out a series of calculations for other atoms in NFO and orientations, to show a similar imbalance between L_3 and L_2 signal in going away from direct positions (or Bragg beam) towards perpendicular *q* direction.

Table 3.2: Variation in dichroic percentages along three different principle axes with two different detector positions for the case of NFO. Copyright (2015) by American Physical Society [38].

	X - orientation				Y – orientation				Z - orientation			
(θ_x , θ_y)	(0 , 0)		(9.44 , 0)		(0 , 0)		(9.44 , 0)		(0 , 0)		(9.44 , 0)	
	L_3	L_2	L_3	L_2	L_3	L_2	L_3	L_2	L_3	L_2	L_3	L_2
Tet Fe	-26.37	5.09	-26.31	3.57	-21.16	10.33	-14.49	10.44	-13.16	14.37	-24.14	7.59

In addition to this, for the case of cubic crystal the appearance of diffraction pattern along three different principle crystallographic axes (i.e. *x*, *y* and *z*) are indistinguishable and we do not have any prior knowledge on the orientation of crystal along the beam direction (but the crystal knows!). Momentum resolved EELS experimentation will give different percentage dichroic signal along three different beam directions because of the anisotropy of *d* orbitals. The calculated results are summarized in Table 3.2. The experimentation along three different principle axes for NFO (g = <440>) shows that the trend is indeed according to the theoretical prediction. This has consequences on the quantitative moments analysis by EMCD either in terms of moment ratio or their individual values. The experimental results show very high m_L/m_S ratio value due to such behavior therefore one need to rectify this percentage by taking guidance from theory to obtain the correct moments ratio.

Table 3.3: C and D values along g=440 obtained from the three different crystallographic axes of NFO. Copyright (2015) by American Physical Society [38].

NFO / g = 440	% C (Fe L_3)	% D (Fe L_2)
1st axis	2.70	-0.59
2nd axis (plan view)	2.68	-0.65
3rd axis	1.59	-0.71

3.4.4 Magnetic Dichroic Signal from NFO and CFO

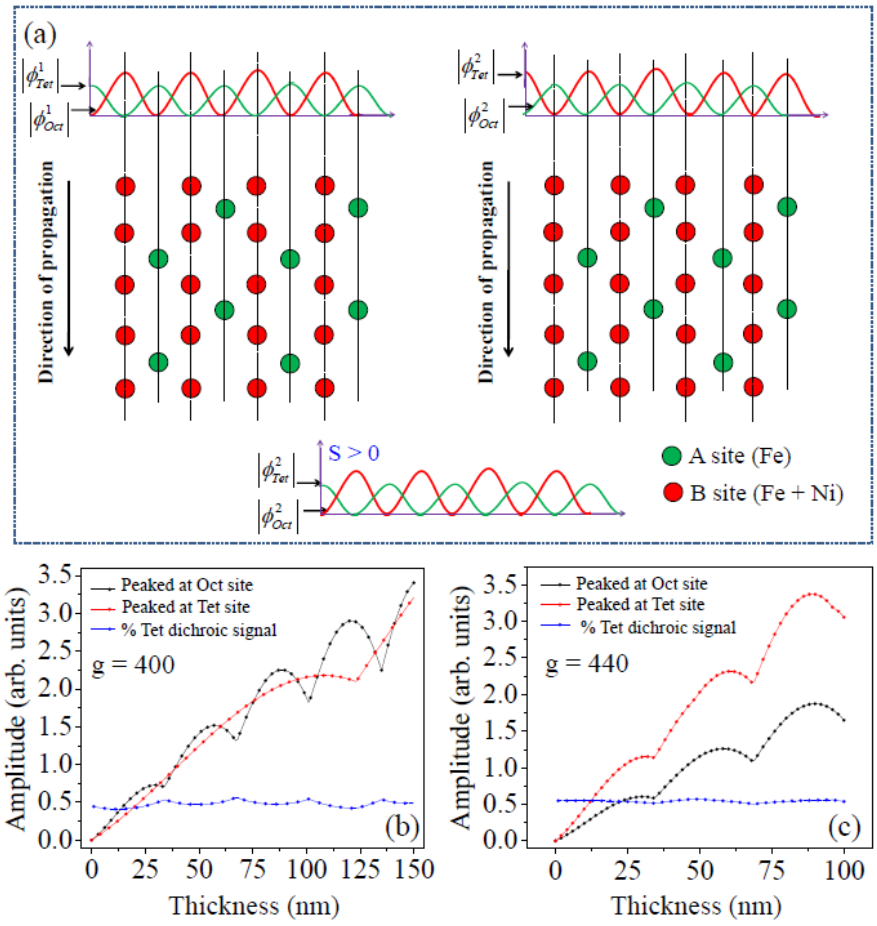

Figure 3.10. (a) Two independent sublattice based model for inverse spinel structure where Bloch waves corresponding to tetrahedral and octahedral symmetry are shown. Percentage signal contribution from tetrahedral Fe site relative to octahedral site with (b) g = 400 and (c) with g = 440 diffracting condition. The % contribution does not oscillate strongly with thickness and shows almost constant value. Copyright (2015) by American Physical Society [38].

EMCD experiments are carried out with two different diffracting vectors, 400 and 440 types. The corresponding extinction distances for the NFO ideal inverse spinel structure are 95.5 nm and 78 nm respectively. These extinction distance values are calculated from average Fourier component of the crystal potential for a given periodicity but this is not an accurate description of extinction distances for spinel structure for the following reasons.

In the case of inverse spinel structure, for 400 type reflection, 4B (2Fe↑+2Ni↑) planes will concentrate the channeled electrons relatively more than 2A (2Fe↓) planes and for 440 type, 4A+4B (4Fe↓+2Fe↑+2Ni↑) planes channel more electrons as compared to 4B (2Fe↑+2Ni↑) planes. The above understanding is qualitatively developed based on relative atomic density for a given plane. Therefore, with 400 and 440 diffracting vector, signals from octahedral Fe, Ni and tetrahedral Fe were previously assumed to dominate the EMCD spectra, respectively [28]. This notion is not correct and significant contributions from other sites will be present. For g = 400 diffraction condition, it was previously shown that the percentage contribution from tetrahedral and octahedral Fe sites will approximately be equal at the exact Bragg condition [34]. The above calculation was based on atomic site dependent evaluation of EELS cross section under two beam condition (single electron model with Bloch wave formalism) for a given aperture position (due to the treatment of inelastic waves as Bloch waves) and specimen thickness. This calculation assumed the same average extinction distance for both the tetrahedral and octahedral 400 periodic planes, which is not the correct picture (see Fig. 3.10 (a) for schematic). Therefore, we have taken a different and simpler approach, which provides insight into the physical processes involving electron channeling through specific atomic planes and its absorption, which is probabilistic in nature. We have calculated the Fourier component of crystal potential separately for atomic planes (e.g., 4B and 2A separately for 400 reflection) having same periodicity (400 and 440 in the present case) formed by the octahedral and tetrahedral atoms corresponding to two independent sub-lattices. Table 3.4 shows the atom averaged amplitude for tetrahedral and octahedral sub-lattices in NFO (similar numbers and trend are obtained for CFO).

The calculation for sub-lattice contribution to the amplitude is performed in JEMS [35] after removing atoms from specific sites (e.g., to measure the effect of tetrahedral sites, the atoms from octahedral sites are removed). The average amplitude considering both the sites equals the amplitude for the lattice containing all the atoms. However, extinction distances

cannot be averaged in this manner and need to be evaluated from the corresponding amplitude separately (because of reciprocal relationship). This approach gives extinction distances corresponding to g = 400 as 67 nm and 375 nm for octahedral and tetrahedral sub-lattices, respectively. From this, absorption per atom was evaluated for a given plane that depends on particular atomic density of that plane.

$$abs\left(a*\sin\left(\frac{pi*t}{\xi_g}\right)-a*\sin\left(\frac{pi*t}{\xi_g}\right)*\exp\left(-\frac{pi*t}{\xi_g'}\right)\right) \quad \text{... (3.4)}$$

$$abs\left(a*\cos\left(\frac{pi*t}{\xi_g}\right)-a*\cos\left(\frac{pi*t}{\xi_g}\right)*\exp\left(-\frac{pi*t}{\xi_g'}\right)\right) \quad \text{... (3.5)}$$

Eq. 3.4 & Eq. 3.5 are the expressions for absorption by the direct and diffracted beams for a given plane respectively. Eq. 3.6 represents the absorption for the case of tetrahedral site at exact Bragg condition and similarly absorption per atom is evaluated for octahedral site also.

$$abs\left(2.04*\sin\left(\frac{pi*t}{375.24}\right)-2.04*\sin\left(\frac{pi*t}{375.24}\right)*\exp\left(-\frac{pi*t}{3752.4}\right)\right)$$

$$+abs\left(2.04*\cos\left(\frac{pi*t}{375.24}\right)-2.04*\cos\left(\frac{pi*t}{375.24}\right)*\exp\left(-\frac{pi*t}{3752.4}\right)\right)$$

$$+abs\left(11.32*\sin\left(\frac{pi*t}{375.24}\right)-11.32*\sin\left(\frac{pi*t}{375.24}\right)*\exp\left(-\frac{pi*t}{3752.4}\right)\right)$$

$$+abs\left(11.32*\cos\left(\frac{pi*t}{375.24}\right)-11.32*\cos\left(\frac{pi*t}{375.24}\right)*\exp\left(-\frac{pi*t}{3752.4}\right)\right) \quad \text{... (3.6)}$$

The absorption through channeling by the two sub-lattices as a function of thickness for g = 400 is given in Fig. 3.10 (b) along with percentage signal contribution from two different atomic sites. Therefore, the EMCD signal will be composed of ~51% contributions from octahedral Fe atoms and ~49% contributions from tetrahedral Fe atoms at exact Bragg condition. For 440 reflections, the tetrahedral Fe signal will be ~ 54% (Fig. 3.10 (c)). The moment value evaluation carried out by Wang *et. al.* completely ignored these mixing contributions from both

the sites [28]. Ignoring such contribution affects the percentage dichroic signal contribution in the sum rules and results in improper evaluation of the moment values. The confusion lies in the earlier work of authors who assumed that the tetrahedral atoms are like impurity sites and Bloch wave propagation through these can be ignored [36]. This is not true as one can clearly see the tetrahedral atoms along the zone axis imaging condition by HR-STEM, which suggests that the channeling through *A* site cations cannot be ignored relative to *B* sites [20,37]. However, if one considers all the sites then one can estimate such contributions not only at Bragg condition but as a function of deviation parameter, *s* [35]. However, the EMCD experiment with the deviation from Bragg condition is not recommended as the diffracted beam amplitude will be reduced and consequently the EMCD signal (Fig. 3.8 (a)). We have taken into consideration this mixing contribution from other sites along with the thickness effect on the dichroic signal and '*K*' parameter. If one corrects for such relative contributions for the values listed in Table 3.4 (for NFO, Fe oct, m_s = 0.2772, this is the value after mixing effect), then it closely matches with the DFT-based calculations [38]. For CFO, the mixed (both *A* and *B* site contribution) spin moment values are somewhat higher (Fe oct, m_s = 0.8563) because of mixed cation character (see subsequent section for the discussion). The results are in very good agreement with the theory, unlike the case in Ref. 28.

Table 3.4: Tetrahedral and octahedral sub lattice dependent amplitude and extinction distances for NFO and CFO structures. Copyright (2015) by American Physical Society [38].

Structure	Diffracting plane	Tetrahedral Lattice		Octahedral Lattice	
		Ext. Dist. (nm)	Amplitude (per Vol)	Ext. Dist. (nm)	Amplitude (per Vol)
NFO	(400)	375.24	2.04	67.45	11.32
	(440)	132.41	5.77	96.14	7.96
CFO	(400)	422.02	1.81	67.37	11.34
	(440)	139.69	5.46	96.12	7.94

All the experimental EMCD spectra are acquired extracted according to the procedure discussed in Chapter 2.2.2.1. The obtained spectra are pre-edge background subtracted using a straight line deduction to remove any background at the L_3 edge onset. Peak fitting procedure is followed to accurately extract the dichroic signal and get rid of any unwanted signal due to the noise resulting from various sources during acquisition. The fitting equation is considered such that it accounts for various components contributing to the intensity at each edge [38].

$$I_{fit}(E) = \sum_{2,3}\left(h_{2,3}A\left\{1+\left[\frac{E-E_{2,3}}{\beta+\alpha\left(E-E_{2,3}\right)}\right]^2\right\}^{-1}\right.$$
$$+h_{2,3}\left(1-A\right)\exp\left\{-\ln\left(2\right)\left[\frac{E-E_{2,3}}{\beta+\alpha\left(E-E_{2,3}\right)}\right]^2\right\}$$
$$\left.+B_{2,3}\left\{\frac{1}{2}+\frac{1}{\pi}\arctan\left[\frac{E-E_{2,3}}{\gamma/2}\right]\right\}\right) \quad \text{..... (3.7)}$$

Factors such as the broadening of the peak, the peak intensity, asymmetry etc., are taken into account in choosing the fit equation as shown in the Eq. (3.7). Gaussian and Lorentzian curves with asymmetry factor are used to fit the $L_{2,3}$ shape as accurately as possible. Step function containing arctan function is fitted to model the background resulting from the core-to-continuum transitions. In the Eq. (3.7), $h_{2,3}$ represent the amplitude of the $L_{2,3}$ peaks, $E_{2,3}$ the energy position of $L_{2,3}$, 'A' is the Lorentzian-Gaussian mixing ratio, α is the asymmetry, 2β is the Full Width at Half Maxima (FWHM) of the peak. $B_{2,3}$ is the amplitude and γ is the steepness of the arctan functions for the background. The $L_{2,3}$ difference spectra obtained from the two positions is the dichroic signal from which the orbital and spin magnetic moments are evaluated using the sum rules.

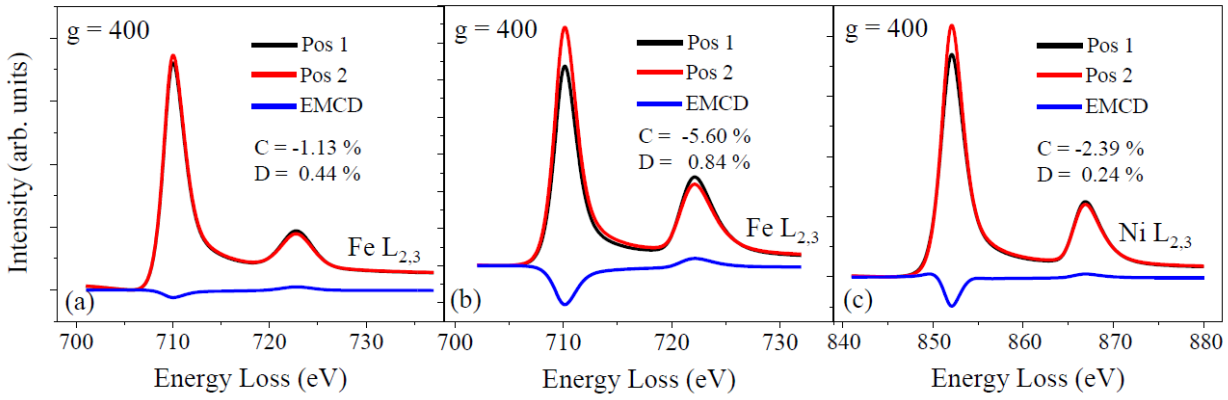

Figure 3.11. Example EMCD spectra for NFO with g = 400 diffracting vector. (a) From ideal inverse spinel structure and (b) from A site cation defect area from Fe. (c) EMCD spectra from Ni. Copyright (2015) by American Physical Society [38].

In the case of NFO, the previously performed spatially resolved optical studies by HREELS revealed that the films do not show any cation mixing and the robust structure is inverse spinel. We observe very low dichroic signal in most of the sample regions (C = -1.203±0.33 %) for *g* =400 condition (see Fig. 3.11 (a)). This is because of near cancellation of dichroic signal from the Fe residing at two different sites where moment directions are opposite to each other. A few areas give higher values of dichroic signal (see Fig. 3.11 (b), C = -5.593±1.5%) and these correspond to *A* site cation vacancy regions (see Ref. 20), where in the absence of *A* site cations, the net moment contributions increases from the *B* site Fe [21]. Similar observation has been made for *g* = 440 diffracting condition. For Ni the dichroic signal is relatively strong (C = -3.13±0.58%) as there is no cancellation effect like as in the case of Fe (see Fig. 3.11 (c)).

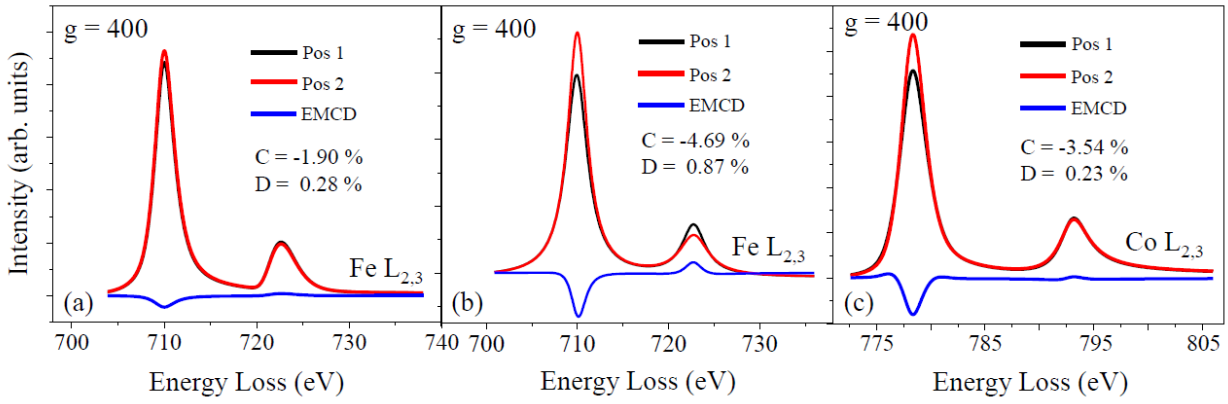

Figure 3.12. (a) Example EMCD spectra for CFO with g = 400 diffracting vector. (a) EMCD signal from ideal inverse spinel area and (b) from cation mixed area from Fe. (c) EMCD spectra from Co. Copyright (2015) by American Physical Society [38].

In case of CFO, theoretical calculation of cohesive energy suggests that the structure can deviate from ideal inverse spinel configurations with the mixing of *B* site Co with *A* site Fe [21]. For 50% mixing case one can see that *B* site Co adopts a low spin configuration and this is compensated by *A* site Co. This means while performing experiment with 440 and 400 diffracting condition, octahedral Fe EMCD signal will dominate for 50% mixed case and for all intermediate cases $[(4-x)Fe\downarrow+xCo\downarrow+ (2+x)Fe\uparrow+(2-x)Co\uparrow]$ in comparison to ideal inverse spinel configuration. For Fe, in most of the areas we observe intermediate (C = -2.711±0.68%, see Fig. 3.12 (a)) and in some areas higher (C = -5.229±0.69%, see Fig. 3.12 (b)) percentage of dichroic

signal from regions having mixed cases and *A* site cation defects, respectively. This is the first time that EMCD has been used to study the cation mixing effect in spinel oxide system and the uniqueness of the technique is demonstrated in comparison to its X-ray counterpart. For Co we see higher percentage of dichroic signal. This is because for mixed case, *A* site Co will have higher magnitude of moment (2.54 μ_B per atom) compared to *B* site Co (0.81 μ_B per atom) (see Fig. 3.12 (c)) [21].

3.5 Conclusions

Element and site-specific quantitative magnetic moment is evaluated by EMCD for two important spinel oxide thin films, $NiFe_2O_4$ and $CoFe_2O_4$. Nanoscale magnetism by EMCD is demonstrated to be extremely useful in obtaining atom specific and site specific spin and orbital magnetic moments from the regular inverse spinel structure, as well as from the distinguishing regions with *A* site cation defects and cation mixed configurations. We have found that the dichroic signal is much lower compared to theoretically predicted values and an imbalance in the dichroic signal exists between the L_3 and L_2 edges. The former is explained by the oscillating nature of dichroic signal with sample thickness and its thickness average is less than the theoretical value. The latter observation has been related to the momentum resolved signal detection during EMCD experiment. A simple model based on phenomenological absorption is exploited for calculating not only the site specific contributions of signals from inverse spinel configuration but its thickness dependence as well.

3.6 Bibliography

[1]. C. Hébert, and P. Schattschneider, Ultramicroscopy 96, 463 (2003).

[2]. P. Schattschneider, S. Rubino, C. Hébert, J. Rusz, J. Kuneš, P. Novák, E. Carlino, M. Fabrizioli, and G. Panaccione, Nature 441, 486 (2006).

[3]. L. Calmels, F. Houdellier, B. Warot-Fonrose, C. Gatel, M. J. Hÿtch, V. Serin, E. Snoeck, and P. Schattschneider, Phys. Rev. B 76, 060409(R) (2007).

[4]. H. Lidbaum, J. Rusz, A. Liebig, B. Hjörvarsson, P. M. Oppeneer, E. Coronel, O. Eriksson, and K. Leifer, Phys. Rev. Lett. 102, 037201 (2009).

[5]. P. Schattschneider, M. Stöger-Pollach, S. Rubino, M. Sperl, C. Hurm, J. Zweck, and J. Rusz, Phys. Rev. B 78, 104413 (2008).

[6]. P. Schattschneider, J. Verbeeck, V. Mauchamp, M. Jaouen, and A. –L. Hamon, Phys. Rev. B 82, 144418 (2010).

[7]. B. Loukya, X. Zhang, A. Gupta, and R. Datta, J. Magn. Magn. Mater. 324 (2012) 3754.

[8]. B. Warot-Fonrose, C. Gatel, L. Calmels, V. Serin, and P. Schattschneider, Ultramicroscopy 110 (2010) 1033.

[9]. J. Rusz, O. Eriksson, P. Novák, and P. M. Oppeneer, Phys. Rev. B 76, 060408 (R) (2007).

[10]. J. D. Adam, S. V. Krishnaswamy, S. H. Talisa, and K. C. Yoo, J. Magn. Magn. Mater. 83 (1990) 419.

[11]. C. Deng, Y. Zhang, J. Ma, Y. Lin, and C. Nan, J. Appl. Phys. 102 (2007) 074114.

[12]. Y. Zhang, C. Deng, J. Ma, Y. Lin, and C. Nan, Appl. Phys. Lett. 92 (2008) 062911.

[13]. J. J. Yang, Y. G. Zhao, H. F. Tian, L. B. Luo, H. Y. Zhang, Y. J. He, and H. S. Luo, Appl. Phys. Lett. 94 (2009) 212504.

[14]. U. Lüders, A. Barthélemy, M. Bibes, K. Bouzehouance, S. Fusil, E. Jacquet, J. -P. Contour, J. -F. Bobo, J. Fontcuberta, and A. Fert, Adv. Mater. 18 (2006) 1733.

[15]. M. G. Chapline, and S. X. Wang, Phys. Rev. B 74 (2006) 014418.

[16]. A. V. Ramos, M. –J. Guittet, J. -B. Moussy, R. Mattana, C. Deranlot, F. Petroff, and C. Gatel, Appl. Phys. Lett. 91 (2007) 122107.

[17]. N. Li, Y. A. Wang, M. N. Illiev, T. M. Klein, and A. Gupta, Chem. Vap. Deposition 17 (2011) 261.

[18]. L. Shen, M. Althammer, N. Pachauri, B. Loukya, R. Datta, M. Illiev, N. Bao, and A. Gupta, J. Cryst. Growth 390 (2014) 61.

[19]. R. Datta, S. Kanuri, S. V. Karthick, D. Mazumdar, J. X. Ma, and A. Gupta, Appl. Phys. Lett. 97 (2010) 071907.

[20]. R. Datta, B. Loukya, N. Li, and A. Gupta, J. Cryst. Growth 345 (2012) 44.

[21]. K. Dileep, B. Loukya, N. Pachauri, A. Gupta, and R. Datta, J. Appl. Phys. 116 (2014) 103505.

[22]. P. Blaha, K. Schwarz, G. K. H. Madsen, D. Kvasnicka, and J. Luitz, WIEN2k: An Augmented Plane Wave + Local Orbitals Program for Calculating Crystal Properties (Karlheinz Schwarz, Techn. Universität Wien, Austria, 2001).

[23]. F. Tran, and P. Blaha, Phys. Rev. Lett. 102 (2009) 226401.

[24]. D. Koller, F. Tran, and P. Blaha, Phys. Rev. B 85 (2012) 155109.

[25]. L. Pardini, V. Bellini, F. Manghi, and C. Ambrosch-Draxi, Comm. Phys. Commun. 183 (2012) 628.

[26]. B. T. Thole, P. Carra, F. Sette, and G. van der Laan, Phys. Rev. Lett. 68 (1992) 1943.

[27]. C. T. Chen, Y. U. Idzerda, H. -J. Lin, N. V. Smith, G. Meigs, E. Chaban, G. H. Ho, E. Pellegrin, and F. Sette, Phys. Rev. Lett. 75 (1995) 152.

[28]. Z. Q. Wang, X. Y. Zhong, R. Yu, Z. Y. Cheng, and J. Zhu, Nat. Commun. 4 (2013) 1395.

[29]. S. Rubino, P. Schattschneider, M. Stöger-Pollah, C. Hébert, J. Rusz, L. Calmels, B. Warot-Fonrose, F. Houdellier, V. Serin, and P. Novak, J. Mater. Res. 23 (2008) 2582.

[30]. B. Fultz and J. M. Howe, Transmission Electron Microscopy and Diffractometry of Materials, 3rd ed. (Springer, Heidelberg, 2008).

[31]. D. B. Williams, and C. B. Carter, Transmission Electron Microscopy: A Text Book for Materials Science, 2nd ed. (Springer, New York, 2009).

[32]. S. L. Dudarev, L. M. Peng, and M. J. Whelan, Phys. Rev. B 48 (1993) 13408.

[33]. M. Nelhiebel, P. -H. Louf, P. Schattschneider, P. Blaha, K. Schwarz, and B. Jouffrey, Phys. Rev. B 59 (1999) 12807.

[34]. K. Tatsumi, S. Muto, and J. Rusz, Microsc. Microanal. 19 (2014) 1586.

[35]. P. A. Stadelmann, Ultramicroscopy 21 (1987) 131.

[36]. J. Taftø and O. L. Krivanek, Phys. Rev. Lett. 48 (1982) 560.

[37]. K. Tatsumi, and S. Muto, J. Phys.:Condens. Matter 21 (2009) 104213.

[38]. B. Loukya, D. S. Negi, K. Dileep, N. Pachauri, A. Gupta, and R. Datta, Phys. Rev. B 91 (2015) 134412.

[39]. H. Lidbaum, Transmission Electron Microscopy for Characterization of Structures, Interfaces and Magnetic Moments in Magnetic Thin Films and Multilayers, Ph. D thesis, Uppasala University (2009).

Chapter 4

Epitaxial Thin Film Growth of ZnO and Mn/Co alloyed ZnO by Pulsed Laser Deposition - Structural and Magnetic Characterization

This chapter discusses on the ZnO and (Co/Mn):ZnO epitaxial thin film growth, solubility limit, structural and magnetic characterization of these films grown by Pulsed Laser Deposition.
This work has been published in the following journals.

- ✓ *Journal of Crystal Growth, 329 (2011) 20. Copyright (2011) by Elsevier.*
- ✓ *Journal of Magnetism and Magnetic Materials, 325 (2013) 159. Copyright (2013) by Elsevier.*
- ✓ *Superlattices and Microstructures, 63 (2013) 289. Copyright (2013) by Elsevier.*

4.1 ZnO as a Dilute Magnetic Semiconductor (DMS)

ZnO is a direct, wide band gap semiconductor (~3.37 eV) with large exciton binding energy of ~ 60 meV. ZnO has many promising properties for blue or ultra-violet optoelectronics, transparent electronics, spintronic devices and sensor applications. It has hexagonal wurtzite structure with Zn atoms tetrahedrally coordinated by four O atoms. The lattice parameters are a = 3.25 Å and c = 5.12 Å with space group $P6_3mc$ [1].

ZnO being an attractive material for optoelectronic applications, Co/Mn doped ZnO has been paid tremendous attention as a candidate for dilute magnetic semiconductor (DMS) after the prediction of room temperature ferromagnetism by Dietl *et al*. This is based on modified Zener model using mean field theory [2] according to which localized spin of Mn in (III/II,Mn)V/VI compounds couples with its own delocalized itinerant hole via *p-d* exchange interaction to give rise to ferromagnetism [3]. Room temperature ferromagnetism was reported in ZnO with and without transition metal (TM) impurities [4-7] and is a highly controversial and debated topic in today's solid state physics. Ferromagnetism was also observed both in *n*-type and resistive (*r*-type) ZnO samples [8,9]. However, there is no report so far on obtaining a true DMS based on either ZnO or GaN.

Models based on defects and charge transfer to and from defect bands have been put forward to explain ferromagnetism in ZnO based DMS systems [10,11]. Some reports on observation of strong magnetization attributed it either to the formation of secondary incoherent Co or Mn clusters in the matrix of ZnO or contamination due to mishandling of samples [12-14]. Research is still active in order to understand whether this phantom magnetism is intrinsic or not and the possibilities of using these materials in practical application. As already pointed by Dietl, in order to realize *p-d* exchange in this system, solubility of TM elements, self compensation and related issues need to be addressed. There are numerous reports based on Co and Mn doped ZnO, however detailed microstructure and physical property investigation as a function of Co/Mn content is important to understand the system.

Among the various reports on Co:ZnO thin films [15-19], Kenji *et al*. reported solubility of Co up to 50 % by Pulsed Laser Deposition (PLD) and beyond 50 %, phase separation was observed [16]. Co solubility has been reported as high as 70 % under metastable synthesis

condition [18]. CoO, Co_3O_4, $ZnCo_2O_4$ (*n*-type) secondary phases in Co:ZnO systems can show antiferromagnetic coupling whereas $ZnCo_2O_4$ (*p*-type) can show ferromagnetic coupling. Metallic cobalt precipitation was also reported for higher Co doping concentrations (~30 % or higher) [17]. Garcia *et al.* reported that Co_3O_4 can give rise to ferromagnetic response due to surface dispersion of Co^{+3} to Co^{+2} [20]. Few reports attributed Co clusters as a source of strong ferromagnetic response [12,21]. However, first principle study showed that Co ion pair does not have any tendency to form coherent clusters [22] and moreover, the nearest Co-Co interaction is antiferromagnetic [23]. Co:ZnO grown on ZnO substrate is found to be paramagnetic below 20 at.% of Co doping even at very low temperatures (10 K) but ferromagnetic for 20 at.% of Co doping [24]. However, $Zn_{0.9}Co_{0.1}O$ film grown on sapphire was ferromagnetic and the observed magnetism was attributed to the defects. Absence of ferromagnetism was also reported in Co/Mn doped system by Rao *et al.* [25]. Anomalous giant magnetic moment is also reported at room temperature [26,27] and this behavior was described by super coupling of bound magnetic polaron (BMP) or formation of defect states or defect related impurity band. Anisotropy in magnetism is also observed [28,29].

Research on Mn doped ZnO system received more attention after the first report by Sharma *et al*. on the room temperature ferromagnetism in bulk and transparent Mn doped ZnO thin films [30]. There are many reports since then discussing the solubility limit [31,32], secondary phase formation [33-36], magnetism (absence of ferromagnetism in few cases) etc. [37-41] in this system. Fukumura *et al*. grew homogeneous alloy thin films on Al_2O_3 with Mn content up to 36 % by PLD [31,32]. Secondary phases such as MnO_2, MnO, Mn_2O_3, Mn_3O_4 were detected [34]. Large magnetization as high as ~20 emu/cm^3 is observed for 7% Mn doped ZnO at 10 K [37], while another report claims paramagnetism for the same Mn content [38]. However, films with high Mn content (~ 36 %) showed no ferromagnetic ordering. Moreover, a strong antiferromagnetic exchange coupling is reported even for very low dopant concentrations [32]. Observed ferromagnetism was attributed to the formation of defects and deep acceptor defect levels formed due to Zn vacancies mediate the parallel alignment of magnetic moments in the system [39]. A weak antiferromagnetic interaction that is increasing with the Mn dopant concentration was observed and interaction remained antiferromagnetic in the presence of donor defects while it turned out to be ferromagnetic with the introduction of acceptor defects [41].

In the present chapter, we present on the detailed experimental approach in growing epitaxial ZnO and ZnO thin films alloyed with Co/Mn up to 30 at.% by PLD to study the solubility limit, secondary phase formation and effect of Co/Mn concentration on the magnetic properties [42,43]. Our investigation has led to novel findings such as composition dependent coercivity in Co:ZnO and secondary phase formation in Mn doped films beyond 25 at.%.

4.2 ZnO Thin Film Growth by Pulsed Laser Deposition

Although ZnO has attracted considerable research attention due to its potential applications in optoelectronics and spintronics, there was no large scale effort to develop ZnO epitaxial thin films based devices in comparison to GaN. This is probably due to the unavailability of crystal growth techniques to manipulate ZnO thin film during deposition on large lattice mismatch substrates in order to control defect structure similar to GaN [44-48], difficulty in *p*-doping [49-51] and as well as lack of suitable dopants for tuning band gap in the visible range [52]. Growth of ZnO on large lattice mismatched substrate such as *c*-plane single crystal sapphire or Si is inevitable due to the same reason as GaN where defect free large area ZnO single crystal substrates are very expensive. Therefore it is important to understand the ZnO film growth on large lattice mismatched substrates and the major growth parameters controlling crystalline quality, defect structure and morphology, because they have major role to play in controlling electrical, optical and magnetic properties. Reducing defect density not only improves optical and electronic property of ZnO but allows the investigation of dilute magnetic semiconductor systems based on ZnO with various defect configurations. In ZnO based DMS system, mainly point defects dictates the physical properties and we mean the same in our discussions [6,7,10]. PLD technique was chosen because it is easy to control, versatile and economic for academic research study.

There are many reports on PLD growth of ZnO on sapphire to study crystal growth, defect structure, optical, electrical and magnetic properties as a function of various growth schemes [1,10,53-56]. Among these Narayan *et al*. described domain matching epitaxy scheme to obtain single crystalline film for systems where large lattice mismatch is involved including ZnO on sapphire [53]. For ZnO on sapphire relaxation occurs within one monolayer of film thickness and lattice mismatch is accommodated by interfacial misfit dislocations through matching of 5 or 6

(2-1-10) planes of ZnO with 6 or 7 (30-30) planes of sapphire. In another report on multi-stage ZnO growth by kinetic control i.e. allowing nucleation layer and subsequent seeding layer to relax (by growing at 1 Hz laser pulse frequency, typical relaxation time mentioned to be 0.5 s for $SrTiO_3$) improved the surface morphology and smoothness along with the carrier mobility [54]. The growth of film layer by layer by controlling super saturation of plume (lowering laser pulse rate to 1 Hz) was first described by Koster *et al*. for homoepitaxial growth of $SrTiO_3$ [57,58].

However, it is well known for GaN growth on sapphire (large lattice parameter mismatched) by metal organic vapor phase epitaxy that nucleation layer deposited at low temperature (~ 500 °C) contain large density of defects. Low temperature is necessary to achieve substantial coverage of substrate. Upon annealing to high temperature (~ 1000 °C) defective nucleation layer transforms to well-defined crystal shapes and form better quality film [45]. However, we have found that significant number of misaligned crystal domains are present (i.e. rotation between the seed islands) for ZnO directly grown on sapphire at 5 Hz and at various temperatures between 300-700 °C and which gives rise to ring diffraction pattern in large area plan view images (which does not appear clearly in cross section TEM diffraction pattern except streaking at higher order diffraction vector g). The rotation between seed islands does not improve completely upon annealing alone. Our PLD growth system is limited by minimum pressure of 1×10^{-5} Torr and maximum temperature of 850 °C that one can utilize. High temperature and low pressure is important to achieve predominantly two dimensional growths (2D). However, growing the seeding layer at very slow rate i.e. at 1-2 Hz, removes rotations/misalignment between seed islands completely. Kinetic control by lowering laser pulse frequency to obtain smooth film by PLD was demonstrated by Koster *et al*. for $SrTiO_3$ [58]. However, detailed microscopic analysis on the evolution of film grown through kinetic control on large lattice mismatched substrate is not available. Therefore, in the present study we report on the microstructure of ZnO film grown under different kinetic condition (controlled by laser frequency) as well as other growth parameters such as nucleation condition, pressure, temperature etc on *c*-plane Al_2O_3. Detailed defect microstructure is also presented which are very important to explain any macroscopic property based on ZnO system.

Table 4.1. Growth parameters for various samples of ZnO thin film grown on c-plane Al_2O_3. All samples were grown at 2×10^{-5} Torr pressure except sample S12. Copyright (2011) by Elsevier [59].

Sample	No of steps	Seeding (°C) / No of shots	Annealing	Final growth	Cooling condition
S1	Single	350	-	3000 shots(5Hz)	2 hrs to RT at 10^{-3} Torr
S2	Single	350	-	3000 shots(5Hz)	Same
S3	Single	600	-	5000 shots (5 Hz)	Same
S4	Two steps	300 (250 shots/5Hz)	Ramp to 650 °C in 15 min and stay for 20 min	4000 shots at 650°C, (5Hz)	same
S5	Two steps	300 (250 shots/5Hz)	Ramp to 650 °C in 30 min and stay for 10 min	4000 shots at 650°C, (5Hz)	same
S6	Two steps	300 (250 shots/5Hz)	Ramp to 700 °C in 40 min and stay for 20 min	5000 shots at 700°C, (5Hz)	same
S7	Single	300 (250 shots/5Hz)	-	-	same
S8	Single	300 (250 shots/5Hz)	Ramp to 700 °C in 40 min and stay for 20 min	-	same
S9	Three steps	400 (300 shots/2Hz)	Ramp to 800 °C in 40 min and stay for 20 min, then 1000 shots at 2Hz	4000 shots at 800°C, (5Hz)	same
S10	Three steps	400 (300 shots/2Hz)	Ramp to 800 °C in 40 min and stay for 20 min, then 1000 shots at 2Hz	9000 shots at 800°C, (5Hz)	same
S11	Three steps	400 (300 shots/1Hz)	Ramp to 800 °C in 40 min and stay for 20 min, then 1000 shots at 1Hz	9000 shots at 800°C, (5Hz)	same
S12	Three steps	400 (300 shots/2Hz)	Ramp to 800 °C in 40 min and stay for 20 min, then 1000 shots at 2Hz at 10^{-2} Torr	4000 shots at 800°C, (5Hz) at 10^{-2} Torr	2 hrs to RT at 10^{-2} Torr

We have used ZnO sintered pellets (99.99 % purity, Sigma Aldrich) as PLD target. Sintered ZnO pellets (~ 17 mm dia.) were prepared first by cold pressing ground ZnO powders (< 5 μm) and then sintered in air under atmospheric pressure and temperature at ~900°C for 5 hrs. Excimer laser (KrF, λ ~ 248 nm) with 150 mJ energy (~1.5 J cm^{-2} energy density at the target) was used to ablate ZnO target. Distance between sapphire substrate (0001 orientation) and target was kept at ~5 cm. Samples grown under various conditions are listed in Table 4.1 for comparison purpose. All the thin films were grown under identical substrate preparation before growth (except sample S2 where we have studied the effect of sapphire substrate oxidation on ZnO crystal growth) and cooling down procedure after completion of deposition. ZnO thin films were studied by various characterization techniques such as Scanning Electron Microscopy (SEM) and Atomic Force Microscopy (AFM) for surface morphology and roughness, photoluminescence (PL) for emission peaks. Plan view (PV) and cross-sectional (X-TEM)

samples were prepared and studied in FEI TITAN^{3TM} transmission electron microscopy (TEM) operating at 300 kV for misaligned crystal domains, defect structure, crystallinity etc., Hall measurements for carrier concentrations and mobility. The Hall mobility was measured using an AC transport option inbuilt in the physical property measurement system (PPMS, Quantum Design, U.S.A.). To measure only the potential difference due to the Hall potential, Hall resistivity corresponding to the Hall voltage was measured for both positive and negative applied magnetic fields. The actual Hall resistivity was calculated by subtracting the average of these two values from the measured resistivity at a particular magnetic field. TEM samples were prepared following the same procedure as described in Chapter 2.2.1 by conventional mechanical and tripod polishing and final thinning to perforation in a Gatan PIPs with Ar ion energy of 4.5 kV. For plan view and cross sectional samples left/right gun setting was +7/+7 and +7/-7 respectively.

4.2.1 Single Step Growth

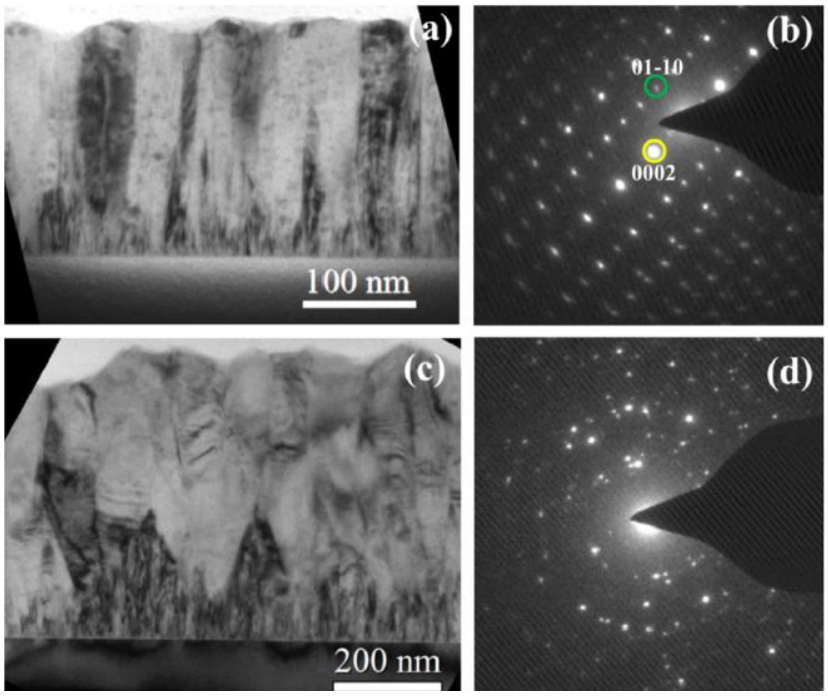

Figure 4.1. TEM bright field images and diffraction pattern from sample S1 (a & b) and S2 (c & d). Growth direction is [0002] for all samples. DPs are not aligned with the image and taken from ZnO only. Copyright (2011) by Elsevier [59].

Samples S1 and S2 were grown under identical conditions (single step growth) except substrate of the sample S2 was oxidized at 600 °C for 30 min prior to deposition at 350 °C. The cross sectional TEM images and corresponding diffraction patterns are displayed in Fig. 4.1. Streaking in spots at higher *g* is clearly visible from diffraction pattern whereas spots are more scattered in S2. Dark contrast areas are crystal domains which are rotated from perfect epitaxial orientation and fringe contrast is due to Moiré fringes between rotated/misaligned and epitaxial crystals. This fringe contrast is not from inversion domain boundaries which appears only with diffracting vector $g = <0002>$. Presence of more scattered spots in sample S2 indicates oxidation of sapphire substrate (i.e. significant chemical reaction between oxygen and sapphire) that led to the formation of large population of tilted and rotated crystals. SEM images (Fig. 4.2) show rough but complete surface coverage from these two samples. Incomplete coverage of ZnO on substrate was obtained for single step sample of S3 grown at higher temperature [see Fig. 4.2(c)], which is generally the case for large lattice mismatched epitaxy.

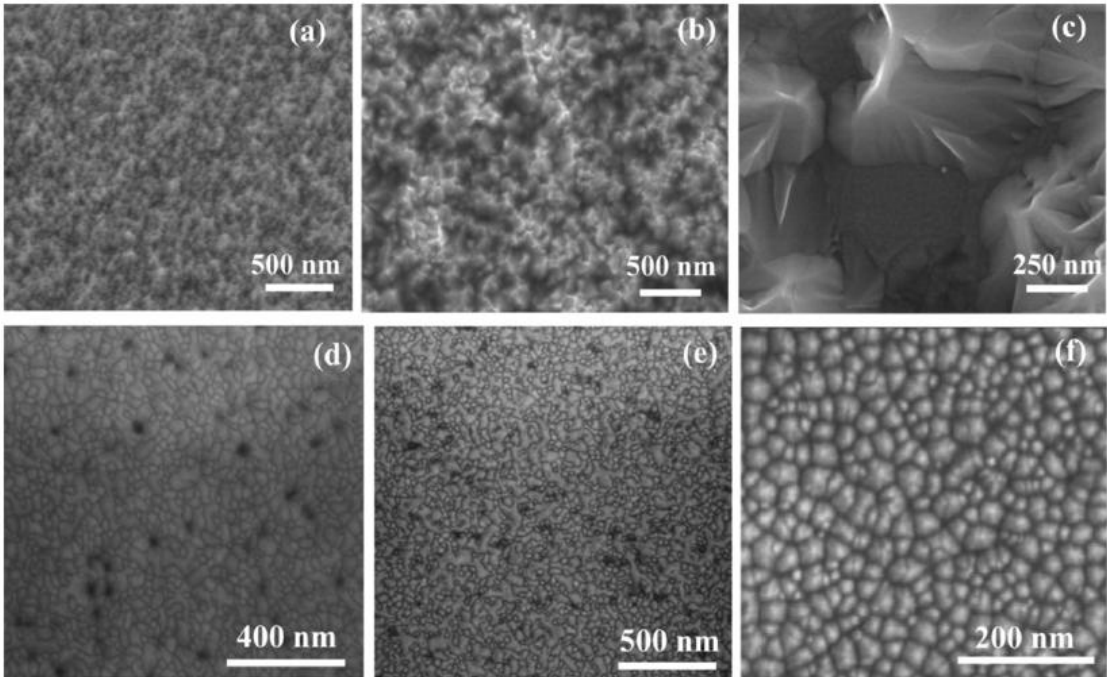

Figure 4.2. SEM images of samples (a) S1, (b) S2, (c) S3, (d) S4, (e) S5 and (f) S6. Copyright (2011) by Elsevier [59].

4.2.2 Two Step Growth

Sample S4, S5 and S6 were grown with two step procedures. Seeding and growth were performed at two different temperatures i.e., 300 shots at 300 °C and 4000 shots at 650 °C

respectively (for S4 and S5). Seeding layer temperature was kept low to achieve complete coverage on sapphire substrate by ZnO. These three samples slightly differ in duration of annealing and final growth temperature. Annealing was performed with the intuition to improve the crystalline quality and establish large area epitaxial relationship with substrate so that no misalignment/rotation is observed from PV electron diffraction pattern. The two step growth schematic representing the growth of nucleation layer at low temperature, ramping to high temperature and then growth is shown in the Fig. 4.3.

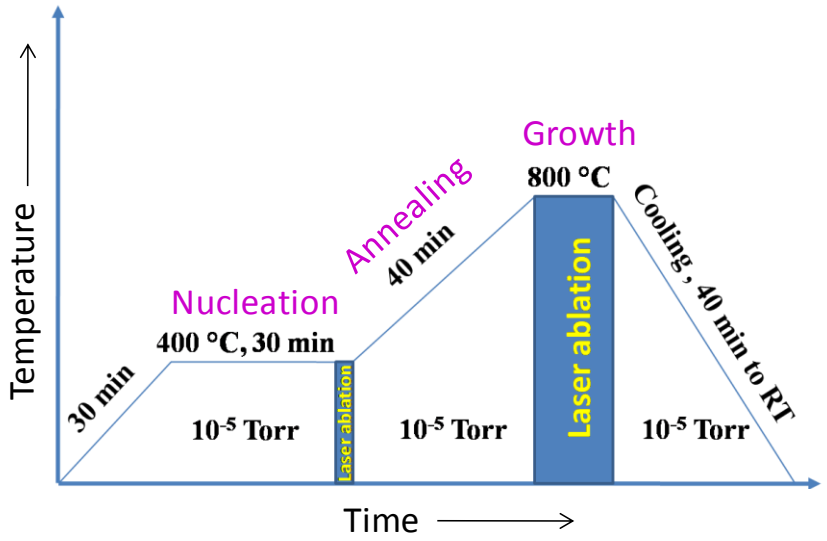

Figure 4.3. Growth schematic that we followed to obtain epitaxial thin films grown by pulsed laser deposition method. Deposition of nucleation layer at low temperature and annealing before actual growth ensures the wetting of substrate that is the key to obtain epitaxial growth of ZnO on sapphire.

Figure 4.2 shows the SEM images taken from these three samples. Sample S4 appears to be completely coalesced but has large number of small crystal grains. Increasing the annealing time led to large crystal grains with incomplete coalescence (sample S5). To achieve complete coalescence, growth temperature was increased by 50 °C and number of laser shots by 1000 (sample S6) and this formed coalesced and round crystal grains. Figure 4.4 displaying the TEM cross sectional and plan view images and corresponding diffraction pattern from samples S5 and S6 respectively. From cross sectional images misaligned/rotated crystal grains and Moiré fringe pattern are observed for both the samples. PV diffraction pattern captured the ring pattern from rotated grains comprehensively compared to cross sectional geometry over a large *c*-plane area.

Dark contrast areas in PV images are regions which are rotated differently than epitaxial orientation. Samples S7 and S8 are the seeding layers deposited to study the substrate coverage. We observe that well defined crystals have formed upon annealing the seed layer as the case of S8. This is also evident from the TEM PV bright field imaging and diffraction patterns proving misalignment improves to some extent upon annealing [59]. Therefore annealing alone is not sufficient to bring all crystal domains into registry with the substrate for the given annealing condition. All the above samples were grown with laser pulse frequency of 5 Hz.

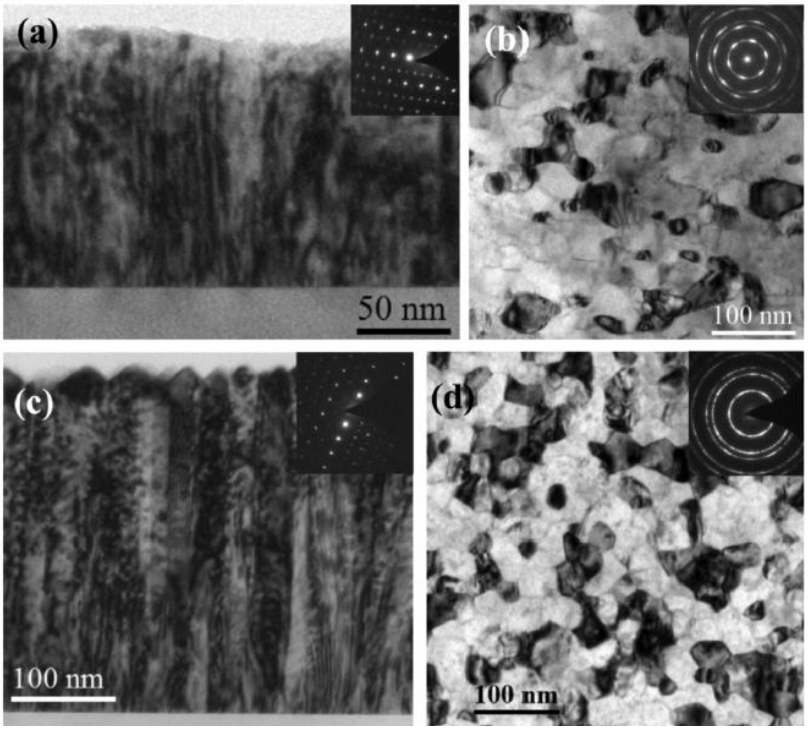

Figure 4.4. Cross sectional and plan view TEM bright field images from sample S5 (a & b) and S6 (c & d) respectively. Corresponding diffraction pattern are shown in inset. Clear rotation in diffraction pattern is observed from plan view geometry. Dark contrast areas in PV images are misaligned crystallites. Copyright (2011) by Elsevier [59].

4.2.3 Three Step Growth

In these three set of samples (S9, S10, and S11) laser pulse frequency was reduced to 2 Hz (S9 and S10) or 1 Hz (S11) during the first two steps (two step seeding) in three step growth at 400 °C and 800 °C respectively to grow the layers at a very slow rate allowing sufficient time for relaxation or establishing epitaxial relationship between seeding layer and substrate. Final deposition (third step) was done at 5 Hz laser frequency at 800 °C. To achieve complete

coalescence, number of final shots was increased from 4000 (sample S9) to 9000 for sample S10 & S11. X-TEM and PV-TEM images along with electron diffraction pattern are shown in Fig. 4.5. Seed layer thickness after first step growth is determined to be ~50 nm. Significant improvement in epitaxial relationship is observed from TEM images and diffraction pattern. Misaligned/rotated crystals are not observed and single crystalline spot pattern is obtained. From plan view images (g=<11-20>) one can see the presence of edge type threading dislocations with few screw and mixed type. Dislocation density estimated to be ~ 10^{10} cm^{-2}. X-TEM image with g = <0002> diffraction vector is presented where one can observe only screw and mixed type dislocations. A surface roughness value ~2.4 nm is obtained from AFM images for sample S11.

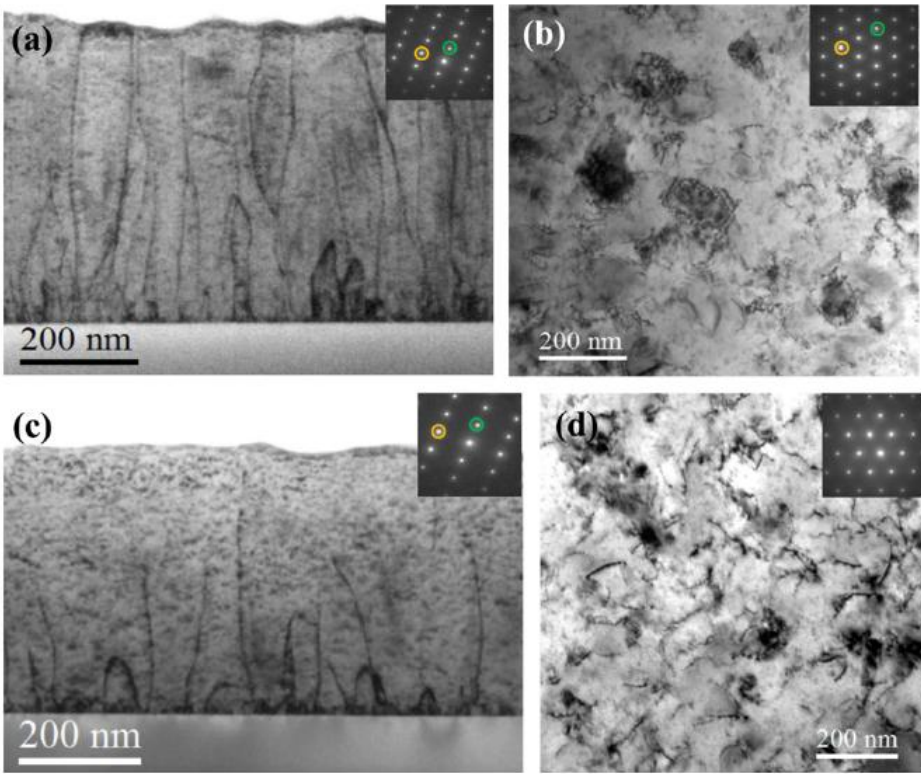

Figure 4.5. X-TEM and plan view images from sample S10 (a & b) and S11 (c & d) respectively. Inset showing single crystal diffraction from ZnO film. X-TEM images with g = <0002> are displayed where only screw and mixed type TDs are visible. Spots circled with green and yellow color are g=0002 and 11-20 for cross sectional case and g=11-20 and 01-10 for plan view case. Growth direction is [0002]. *DPs are not aligned with image and from ZnO only. Copyright (2011) by Elsevier [59].*

However, significant change in morphology was observed when pressure was increased to 10^{-2} Torr during second stage of seeding and final growth stage [59]. Vertical growth of ZnO

can be seen directly from seed ZnO layer without presence of clear crystallographic faceting. The shape is like a bullet and length and width are 100 and 60 nm respectively. They grew with uniform shape and size. This result is reproducible and the density of nanobullets can also be controlled. This is due to predominantly three dimensional growths under higher pressure. The majority charge carriers are electrons for all the samples. The Hall mobility has improved to 58 $cm^2 V^{-1} s^{-1}$ for sample S11 compared to 33 $cm^2 V^{-1} s^{-1}$ for sample S6. This improvement can be explained in terms of improvement in crystal quality by removal of misaligned crystal domains. Further improvement should come with the reduction of threading dislocation (TD) density.

ZnO microstructure such as misaligned crystal boundaries and strain field associated with threading dislocations should have considerable effect on electronic and magnetic properties of this material. Solubility of transition metal (TM) dopants may be affected by this which is important in the area of DMS. Therefore, it is very important to understand and control the microstructure of this material to correlate many physical properties e.g., ferromagnetism with TM doping to facilitate the separation of various factors responsible.

4.3 (Mn/Co):ZnO Epitaxial Thin Film Growth, Structure and Solubility Limit and Magnetism

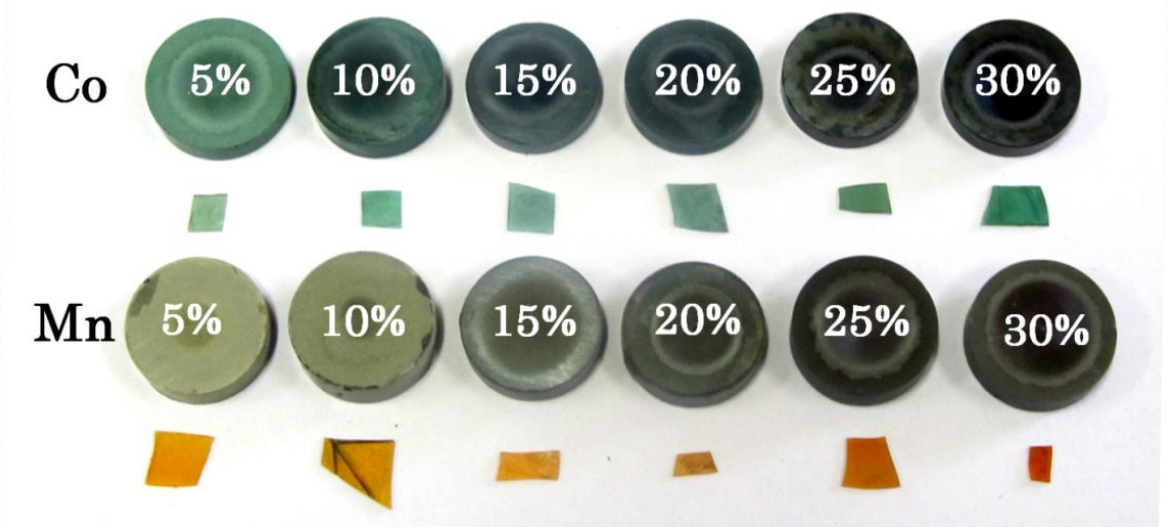

Figure 4.6. Color of the pellets and thin films of both Co:ZnO and Mn:ZnO as a function of alloy concentration. Color shade darkens with increasing alloy concentration indicating that dopants are occupying Zn substitutions sites in the lattice. Copyright (2013) by Elsevier [42].

ZnO thin films doped with Co and Mn (5-30 atom %) were grown by pulsed laser deposition (PLD) technique on sapphire substrate (*c*-plane) according to the single crystal three step growth scheme already discussed above [59]. ZnO target pellets with various atomic (at.) percentage of Co and Mn (5, 10, 15, 20, 25 and 30 at. %) were prepared by mixing ZnO and CoO (for Co:ZnO) and MnO (for Mn:ZnO) powders with 99.99% purity obtained from Sigma Aldrich. The powders were grinded to obtain a homogenous mixture before sintering at 900°C under continuous oxygen flow at atmospheric pressure. The PLD target pellets are shown in Fig. 4.6. After deposition, the colors of the films were green and orange for Co and Mn samples respectively. The color shade darkens with the Co/Mn concentration both in the thin films as well as in the target pellets shown in Fig. 4.6. The color of the films is one of the ways of confirming that Co and Mn have substituted the Zn atoms in the ZnO lattice. This method allows us to dope Co up to 30% and Mn up to 15% without any secondary phase precipitation. High Resolution Transmission Electron Microscopy (HRTEM) studies were performed in an aberration corrected FEI TITAN^{3TM} 80-300 kV microscope to investigate the formation of secondary phases if any and High resolution electron energy loss spectroscopy (HREELS) was used to collect Co $L_{3,2}$ edge for determining its position in the lattice as well as the charge state of Co. Magnetic hysteresis study was performed at room temperature in a superconducting quantum interference device (SQUID), VSM, Quantum Design, USA. Sample size used was 4×3 mm^2.

4.3.1 Mn:ZnO Thin Films

For Mn doped sample we have seen secondary phase formation in a systematic way between the Mn:ZnO and sapphire substrate from Mn doping 25% onwards. Secondary phase has been formed as an interlayer between Mn:ZnO and sapphire substrate (see Fig. 4.7, for 25 and 30 % Mn cases, marked with red arrow). All the films are epitaxial and even for phase separated interlayer sample, incorporation of Mn in the subsequent films is high. Surface of the films is comparatively smoother than Co:ZnO films as can be clearly seen from the TEM images in Fig. 4.7. Films are relaxed on the substrate and threading dislocations are observed to be present in the films. In Fig. 4.8, Mn $L_{2,3}$ absorption edges show clear splitting which confirms that Mn replacing Zn substitutional positions. The L_3/L_2 ratio of the Mn $L_{2,3}$ from the film is ~ 4.5 which is again close to the experimental value reported for Mn^{2+} in Refs. 60 & 61.

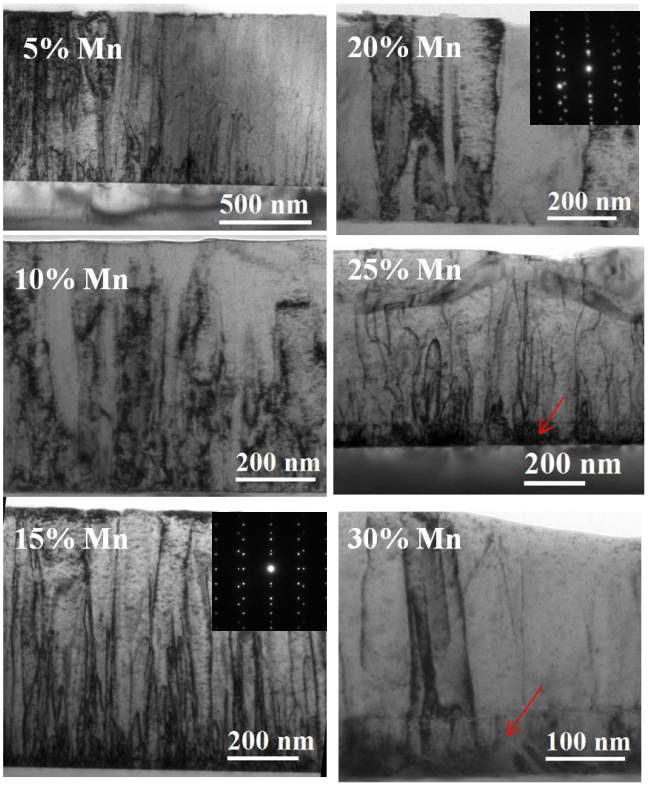

Figure 4.7. TEM bright field images from Mn:ZnO thin films for various alloy concentration. Example diffraction patterns in the inset indicate the formation of single crystalline phase. Red arrows indicate the Mn_3O_4 secondary phase formed as interlayer for 25 at. % and 30 at.% Mn:ZnO. Copyright (2013) by Elsevier [42].

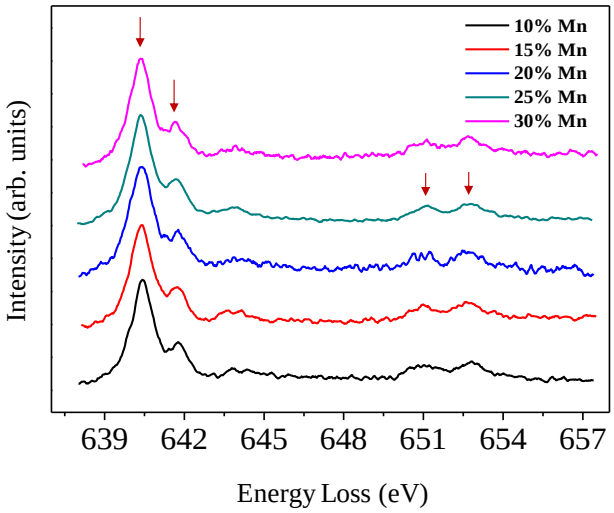

Figure 4.8. Mn $L_{2,3}$ EELS absorption edges showing splitting at L_3 and L_2 as indicated by arrows. This confirms that dopants have occupied the Zn substitutional position in the lattice. Copyright (2013) by Elsevier [42].

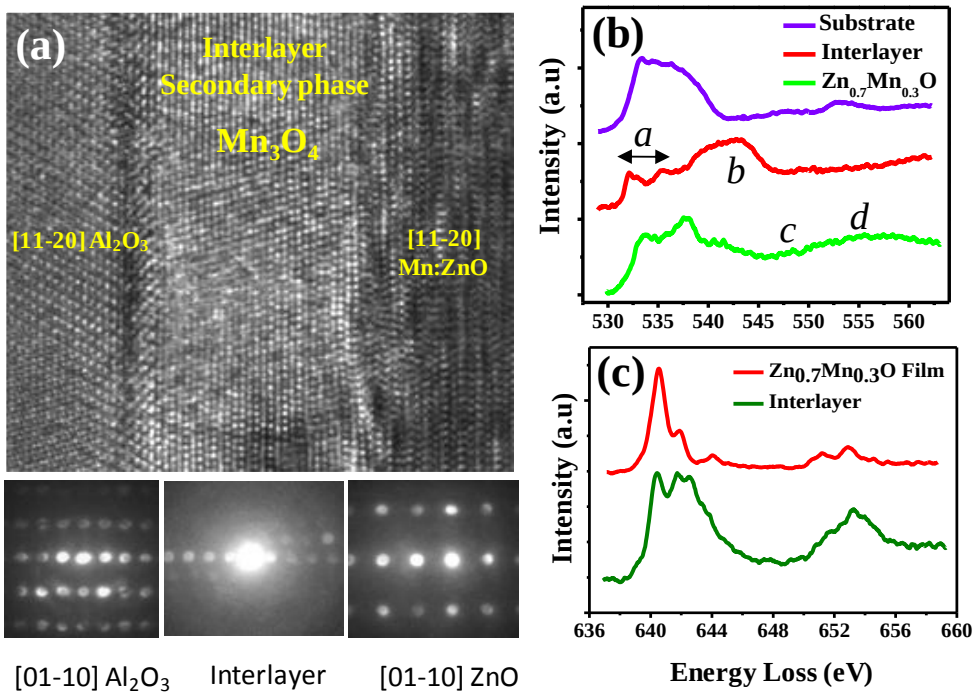

Figure 4.9. (a) High Resolution TEM images from interlayer region (for 30% Mn:ZnO) along with substrate and Mn:ZnO film. One can clearly observe the new alignment of [11-20] Al_2O_3 || [11-20] *ZnO between substrate and film. Below is the corresponding diffraction pattern along* [01-10] *direction from three different layers. (b) Comparison of* O-K *edges from the three different layers and (c) Mn* $L_{2,3}$ *absorption edges from interlayer phase and Mn:ZnO film. Copyright (2013) by Elsevier [42].*

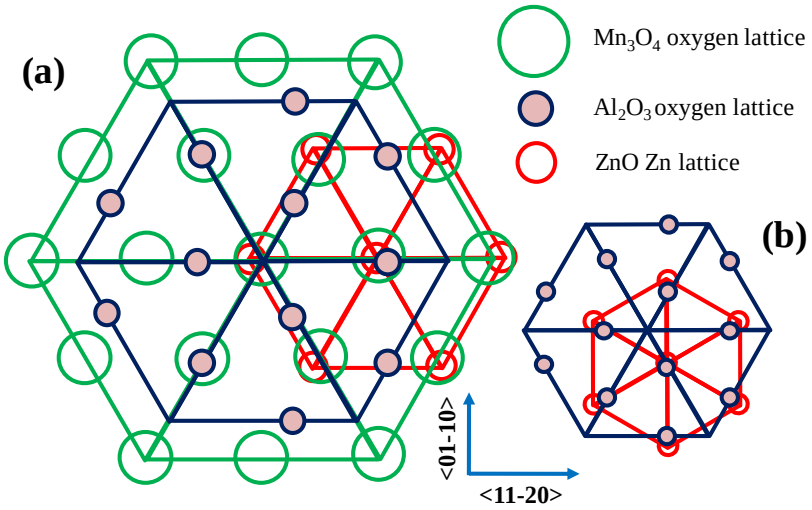

Figure 4.10. New alignment between three different structures shown in (a) which led to [11-20] Al_2O_3 || [11-20] *ZnO compared to the usual* [11-20] Al_2O_3 || [01-10] *ZnO as shown in (b). Copyright (2013) by Elsevier [42].*

The interlayer Mn rich phase has been identified as a spinel Mn_3O_4 phase based on diffraction pattern, high resolution lattice image, both O K and Mn $L_{2,3}$ ELNES and L_3/L_2 ratio (~2.04) (see Fig. 4.9). Comparison of O K absorptions edges from Mn:ZnO, interlayer Mn_3O_4 and sapphire substrate are given in Fig. 4.9 (b). Clear difference in O K edges can be seen between the three materials. The peaks *a* corresponds to transition from O 1*s* to hybridized O 2*p* and Mn 3*d* states and peak *b* corresponds to unoccupied O 2*p* states mixed with Mn 4*sp* bands above the Fermi level. The shape and peaks of the O K and Mn $L_{2,3}$ edges from the interlayer are clearly matching with that of the reported spectra of Mn_3O_4 phase [62-64]. The intensity of peaks *c* and *d* depends on multiple scattering and in our case the strength of these two peaks is weak. From Fig. 4.9 (a), clear …*ABCABC*... stacking can be observed from the interlayer. This cubic phase has grown in such a way that it has rotated the Mn:ZnO layer with respect to sapphire by 30º. This made the possible alignment of Mn:ZnO films with respect to sapphire as [11-20]Al_2O_3 || [11-20]ZnO. The rotation can be explained with the help of Fig. 4.10. Figure 4.10 (b) is the usual case where both *c*-Al_2O_3 and ZnO (0001) plane will be rotated by 30°. In Figure 4.10 (a) the lattice of *c*-Al_2O_3, Mn_3O_4 (111 plane) and Mn:ZnO (0001 plane) is superimposed considering that the lattice is relaxed. The rotation can be explained if these three different crystals align accordingly [11-20]Al_20_3 || [112]Mn_30_4 || [11-20]ZnO as shown in this figure. The formation of this Mn_3O_4 phase might be due to use of low temperature (400 ºC) during the growth of the seeding layer.

We also have grown undoped *n*- and *r*-type ZnO thin films to compare the magnetic properties with that of the alloy samples. Carrier concentrations under *n*-type condition (10^{-5} Torr oxygen partial pressure) is ~ 10^{19} cm^{-3} (with mobility μ_H = 58 cm^2 V^{-1} s^{-1}, measured in a standard Hall system) and the resistance in the *r*-type sample is in the range of kΩ and carrier concentration ~ 10^{17} cm^{-3} (with mobility μ_H = 7 cm^2 V^{-1} s^{-1}, measured in a HL5500 using a buffer amplifier). We can control the resistive and *n*-type sample growth by simply controlling the oxygen partial pressure in PLD chamber during film deposition. Oxygen partial pressure was kept $p_{O2} = 10^{-5}$ Torr throughout the film deposition except for the resistive type sample growth where it is raised to $p_{O2} = 10^{-2}$ Torr during the ramping between different temperatures and holding periods. All the doped films were grown under *n*-type growth condition ($p_{O2} = 10^{-5}$ Torr throughout the growth schedule) as reported in Ref. 59. We also have performed magnetic

measurement for sapphire substrate treated under identical conditions as that of the film growth in order to subtract the diamagnetic response and also to ensure that the magnetic response we see is not due to poor handling of the samples or unwanted contamination in the films. This aspect has already been discussed extensively in literature and is considered to be one of the possible sources of observed ferromagnetism in the system [14]. However, we observed ferromagnetism only for ZnO films but not from the sapphire substrate treated under the same temperature and pressure conditions in the PLD chamber. For Mn:ZnO samples we found that the magnetism is completely disappearing beyond 20% Mn (Fig. 4.11 (b)). Mn:ZnO samples show large paramagnetic signal at higher applied field compared to Co:ZnO samples.

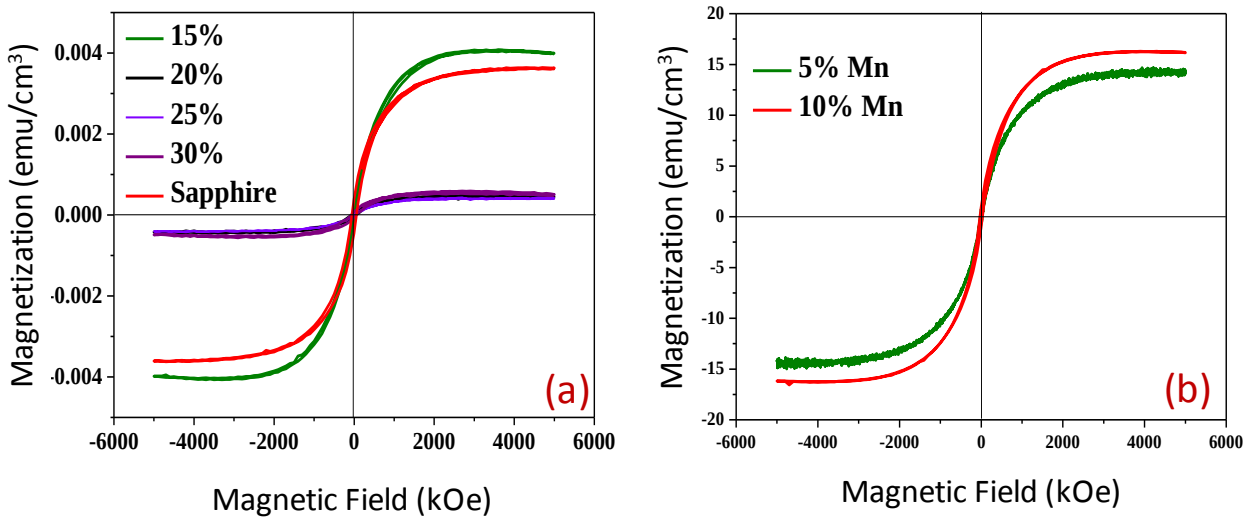

Figure 4.11. M vs H plots for various thin films Mn:ZnO thin films. Observed magnetism is soft and weak. Beyond 20 at. % Mn concentration ferromagnetism disappears. Copyright (2013) by Elsevier [42].

4.3.2 Co:ZnO Thin Films

Co:ZnO films were grown with various Co atomic percentages i.e. 5, 10, 15, 20, 25 and 30 under *n*-type growth condition (with carrier concentration ~ 10^{19} cm^{-3} and mobility μ_H ~ 30-50 cm^2 V^{-1} s^{-1}). The concentration of Co in both pellets and films is characterized by SEM & TEM-EDS and is given in Table 4.2. It can be seen that the concentration of Co in the film is more than that targeted. Similar trend was also reported previously in Co doped ZnO [15]. This could be due to increase in Co concentration in the pellet with laser ablation during the growth.

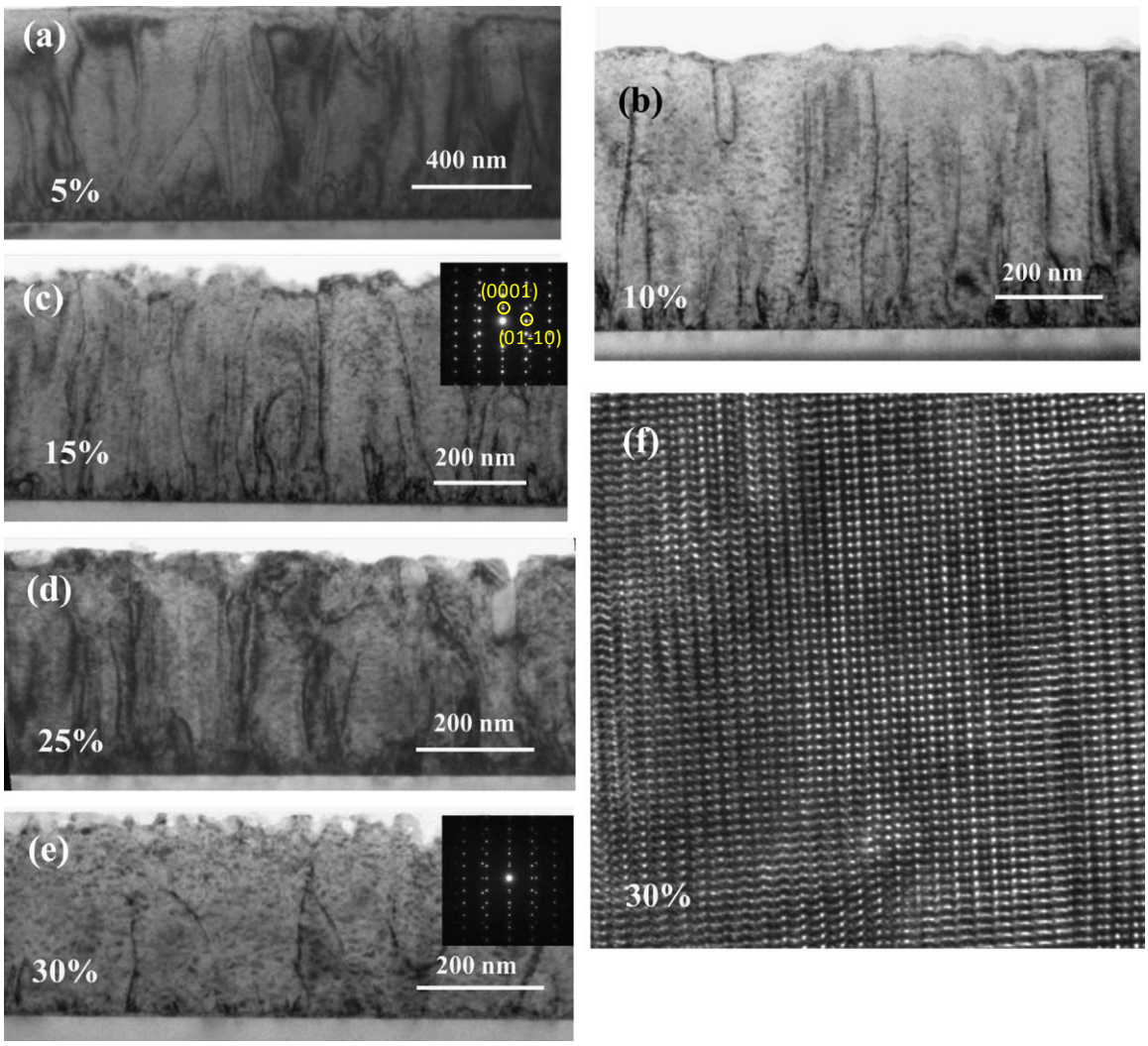

Figure 4.12. (a)-(e) TEM bright field images from Co:ZnO thin films for various alloy concentrations. Example diffraction patterns in the inset indicate the formation of single crystalline phase. No secondary incoherent precipitates are found in these films as examined by HRTEM. (f) Example HRTEM image from 30 at. % Co:ZnO. Copyright (2013) by Elsevier [43].

TEM diffraction contrast shows the presence of threading dislocations. No secondary incoherent precipitates have been detected in the films even at 30 at.% Co doping as confirmed by both conventional strain contrast and high resolution TEM imaging. The films remained single crystalline as evident from diffraction patterns shown in the inset of Fig. 4.12 and there are no scattered spots either due to poly-crystallinity or secondary phases. We did not carry out any experiment to detect the presence of coherent Co clusters or condensed magnetic semiconductors (CMS) in the lattice and the presence of which will not be energetically favorable as revealed by

recent theoretical calculation [22]. Detecting the presence of coherent Co clusters can be performed by spectrum imaging method [60]. High resolution electron energy loss spectroscopy was utilized to collect ELNES (electron energy loss near edge structure) of Co $L_{2,3}$ absorption edge as shown in Fig. 4.13. The characteristic splitting of each L_2 and L_3 edge confirms that the Co atoms have substituted the Zn positions in ZnO lattice [65-68]. The splitting of Co *d* electronic states (e_g and t_{2g}) is due to the crystal field from tetrahedral oxygen environment in the lattice. The Co L_3/L_2 white line ratio is found to be ~2.75. White line ratio of transition metal *L* edge is sensitive to the occupancy of the *d* band, thus related to the oxidation state of the atom. The Co L_3/L_2 ratio value suggests that Co atom has charge state close to +3 [69,70].

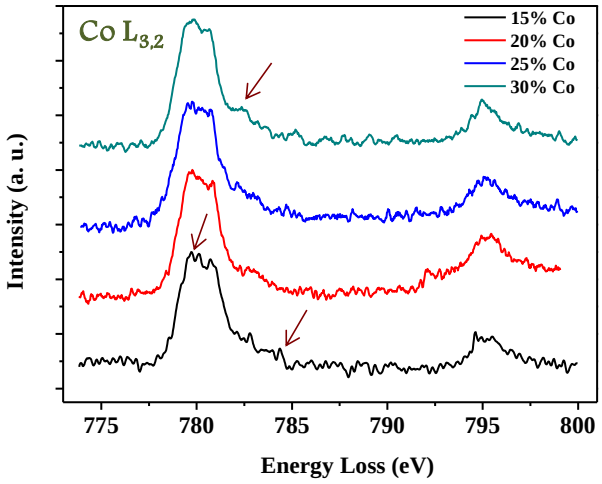

Figure 4.13. Co $L_{2,3}$ EELS absorption edges showing splitting at L_3 and L_2 as indicated by arrows. This confirms that dopants have occupied the Zn substitutional position in the lattice. Copyright (2013) by Elsevier [43].

We have provided magnetic moment per unit volume of the film after considering the correct film thickness as measured from the cross sectional TEM images. Saturation moment is in the order of 10^{20}-10^{21} μ_B cm^{-3} and remains almost the same even for higher Co doped samples. Table 4.2 summarizes magnetic data of Co:ZnO thin films for various doping concentrations along with other information. Figure 4.14 (a) compares the hysteresis loops of Co:ZnO with various Co doping along with undoped ZnO specimens at room temperature. The background of the data is corrected for diamagnetism from sapphire substrate. Sapphire substrate treated under the same heating cycles in the PLD chamber also shows background ferromagnetism in the range of 0.002 emu cm^{-3} after subtracting for its diamagnetic response. We have corrected all the ferromagnetic hysteresis curves due to this sapphire ferromagnetism as well. The sapphire

background ferromagnetism poses a limit on the observation of genuine ferromagnetism in the thin film samples. This background ferromagnetism may be from surface defect states of sapphire [71]. Coercivity remains small to ~ 76 Oe till 5% Co doping concentrations. Beyond 10 % and higher Co doping the coercivity increases significantly and for 25% Co doped sample coercivity is ~ 860 Oe. No significant change in saturation magnetization was observed and a consistent value ~10^{20}-10^{21} μ_B cm^{-3} was obtained even for magnetically undoped sample. The saturation magnetization of *n*-type sample (carrier concentration ~ 10^{19} cm^{-3}) is little higher compared to resistive samples, which means that variation of oxygen point defects and their role as donors does play a role in magnetism in ZnO as already reported previously [10].

Table 4.2. Summary of Magnetic data of various Co/Mn:ZnO thin films. Column 3 of the table lists the theoretical moments only from Co d spins if BMP model is operative. Copyright (2013) by Elsevier [43] and Copyright (2013) by Elsevier [42].

Samples	Magnetization			Coercivity (Oe)	Remnant Magnetization (emu/cm^3)	EDX (Co atom %)
	emu/cm^3 μ_B/cm^3	emu/cm^3 μ_B/cm^3 (BMP)	μ_B/ dopant			
n-type ZnO	39.3 4.24×10^{21}	-	-	27	2.3	-
r-type ZnO	10.28 1.11×10^{21}	-	-	29	0.18	-
$Zn_{0.95}Co_{0.05}O$	7.32 7.89×10^{20}	58.51 6.31×10^{21}	0.375	76	0.68	10
$Zn_{0.90}Co_{0.10}O$	2.19 2.36×10^{20}	116.92 1.26×10^{22}	0.056	730	1.38	14
$Zn_{0.85}Co_{0.15}O$	7.96 8.58×10^{20}	175.47 1.89×10^{22}	0.316	448	2.71	21
$Zn_{0.80}Co_{0.20}O$	105.67 1.14×10^{22}	233.96 2.53×10^{22}	1.35	551	39.13	26
$Zn_{0.75}Co_{0.25}O$	3.6 3.88×10^{20}	292.45 3.15×10^{22}	0.036	860	2.14	30
$Zn_{0.75}Co_{0.25}O^*$	2.97 3.20×10^{20}	292.45 3.15×10^{22}	0.030	1149	1.42	30
$Zn_{0.70}Co_{0.30}O$	14.89 1.60×10^{21}	350.94 3.78×10^{22}	0.127	281	3.48	29
$Zn_{0.95}Mn_{0.05}O$	13.32 1.44×10^{21}	97.5161 1.05×10^{22}	0.686	26	0.58	7
$Zn_{0.90}Mn_{0.10}O$	6.97 7.52×10^{20}	194.885 2.10×10^{22}	0.179	24	0.28	10
$Zn_{0.85}Mn_{0.15}O$	0.93 1.00×10^{20}	292.32 3.15×10^{23}	0.015	22	0.63	20

* Applied field is perpendicular to the *c*-plane.

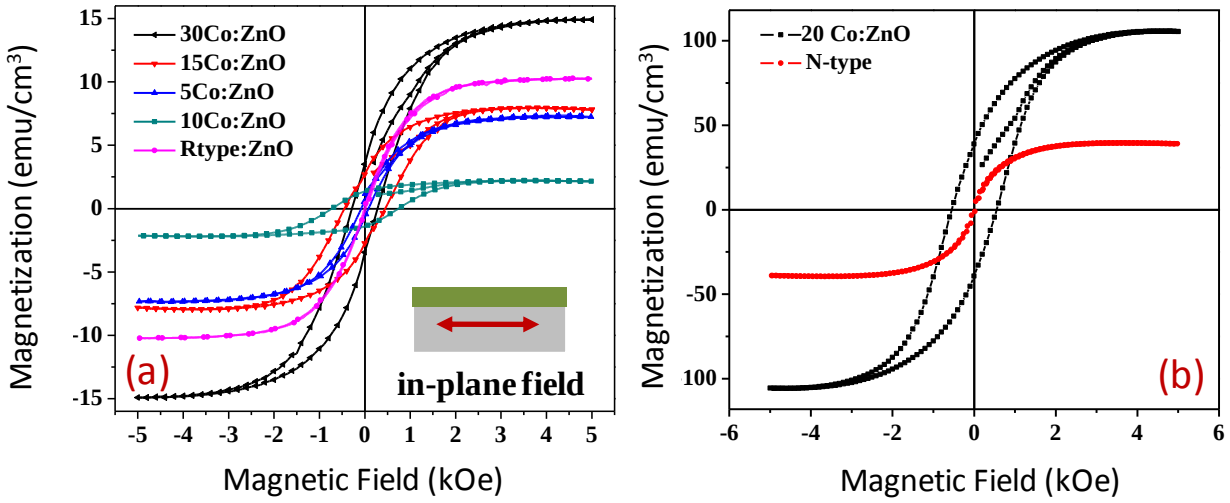

Figure 4.14. M vs H plots for various thin films Co:ZnO showing the composition dependent coercivity. Copyright (2013) by Elsevier [43].

The origin of this high coercivity (detailed explanation given in Chapter 5) may be explained in terms of the interaction between localized Co *d* electrons with the delocalized spin split defect band electrons to some extent. This may be quite possible as the charge state of Co is found to be close to +3, suggesting that charge transfer has taken place to some band possibly to the defect band formed by oxygen vacancy. Delocalized band electrons may be formed due to the oxygen defects in the lattice and are responsible for the *n*-type conduction in our films [11]. Density of states due to oxygen donor defects might satisfy Stoner's criteria and cause the defect band to be spin split. As single Co atom in ZnO show large anisotropy, thus this interaction may be responsible for the observed coercivity in our samples [29]. However, this type of interaction could not align Co *d* electron spins. Otherwise the net saturation magnetization would have been much higher for higher Co concentration according to the Bound Magnetic Polaron (BMP) model (column 2 in Table 4.2) [10]. This is probably due to the two different symmetry and energy level of electronic states of Co *d* electrons and band electrons corresponding to oxygen defects (*s* character).

Figure 4.15 shows the zero field cooled (ZFC) and field cooled (FC) M vs T curves at 4000 Oe applied field for 25 and 20 at. % Co:ZnO samples. No superparamagnetic behavior in terms of blocking temperature is observed in the ZFC curve confirming that there are no Co clusters in the film. At very low temperature paramagnetic Curie tail is observed. This is due to free spins present at the defect sites in the samples. The FC curve can be fitted by three

dimensional spin wave model along with paramagnetic component within it which is of the form $M(T) = CH/T + M_0 - 0.117\mu_B(k_BT/2SJd^2)^{3/2}$, where M_0 is the magnetization at zero temperature, H is the applied magnetic field, CH/T is the paramagnetic part, and d and J are the distance and exchange interaction between magnetic cations respectively [72]. This suggests that the samples have both ferromagnetic and paramagnetic phases. The values of coefficients obtained from the curve fitting are listed in Fig. 4.15. The fitting closely matches experimental curve till ~140.5 K and ~242 K for 25 and 20 at.% Co samples respectively. The difference between FC and ZFC curve at the low temperature side may be due to anisotropic effect of the crystal [73]. FC and ZFC curves can be related by the equation $M_{ZFC}/H = M_{FC}/H + H_c$ and the temperature dependent H_c part can be calculated, where H = 4000 Oe is the applied field and H_c is the coercive field. For example, the H_c value at 100 K is found to be higher (~186 Oe) for 25Co:ZnO compared to 20Co:ZnO (~39 Oe) specimen. This also agrees well with the observation of higher coercivity in room temperature M vs H curve for the 25Co sample compared to 20Co sample. At higher temperature moments are observed to be increasing both in ZFC and FC curve more significantly for 25Co sample (~140 K) than 20Co (~248 K) sample. This may be due to defect state ionization with increasing temperature and their participation in ferromagnetic response. This last feature is more prominent for 25 Co than 20Co sample. This region of the curve can be fitted with temperature dependent point defect formation of the form $n/N_{site} = M + B\exp(-E_f/k_BT)$ where, n/N_{site} is the fraction of point defect ionization, E_f is the formation energy of a particular point defect, M is the magnetization (2.2 emu cm^{-3} at the temperature (in this case ~140 K) at which moment value increases with temperature and B is a coefficient which will contain the information on the contribution of moments from such defects to the FC curve. In our case the dominant point defect may be Zn_i. Formation energy depends on the position of Fermi energy in the band gap of ZnO [74]. Considering typical value of E_f = 0.1 eV, the fitted curve results in B =1. The FC and ZFC curve for 25Co sample shows clear decrease in moments beyond 350 K indicating that the Curie temperature for this sample might be above 400 K. The difference in the behavior between FC and ZFC curve of these two samples could be due to the nature of the defect states and their interaction with Co atoms.

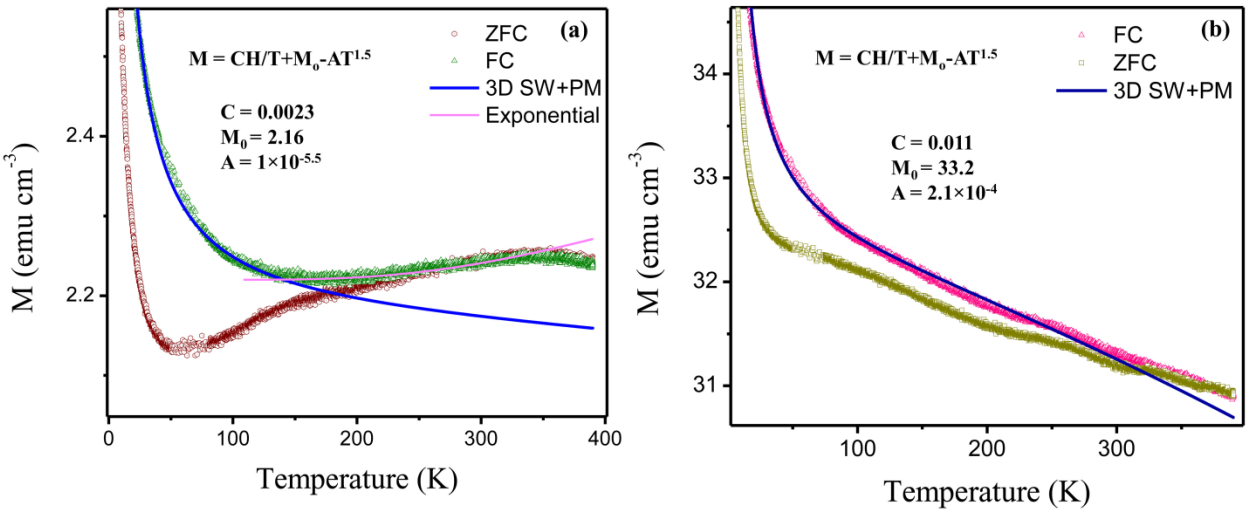

Figure 4.15. ZFC and FC M vs T relation for samples (a) 25 at. % Co and (b) 20 at. % Co. Low temperature side of the curve can be fitted with a 3D spin wave model after including paramagnetic component in it. High temperature side of the curves show increasing moments with temperature due to spontaneous ionization of defect levels and can be fitted with exponential equation as mentioned in the text. The values of the coefficients related to fitting are given within the figures. Copyright (2013) by Elsevier [43].

4.4 Conclusions

The pulsed laser deposition (PLD) of ZnO thin film on *c*-plane sapphire has been studied as a function of various growth parameters such as nucleation layer temperature, annealing duration, laser pulse frequency, number of steps of ZnO deposition, final growth temperature and pressure. Among various growth parameters, laser pulse frequency was found to have significant influence to form single crystal ZnO film on *c*-plane sapphire through elimination of misaligned crystal domains completely. Allowing relaxation to the seeding layer by slowing down laser pulse frequency to 1 Hz established the complete epitaxial relationship between ZnO and sapphire over large area, which is confirmed by plan view single crystal diffraction pattern.

We have investigated Co and Mn incorporation (up to 30 at. %) in ZnO single crystalline thin films grown by pulsed laser deposition technique. Results show that we can incorporate up to 30 at. % Co in single crystal ZnO films without formation of any secondary phase. For Mn:ZnO thin films, spinel Mn_3O_4 phase has been formed as an interlayer between sapphire substrate and Mn:ZnO films for Mn concentration 25% and above. This interlayer has resulted in

the unusual 30º rotation between the subsequent film and the substrate. Saturation magnetization remained the same within the range of 10^{20}-10^{21} μ_B cm^{-3} for undoped and Co:ZnO samples and only coercivity was observed to increase with higher Co concentration in the films. This may be explained in terms of spin split defect band magnetism due to oxygen vacancies and its possible interaction with individual Co *d* electrons to some extent. Therefore it is evident that the magnetism observed in this system originates from itinerant band magnetism due to oxygen point defects. The splitting of Co *d* electron level and their interactions with defect band electrons through charge transfer results in high coercivity. The result shows that it is possible to retain strong magnetization in ZnO semiconductor. High coercivity and remnant magnetization might be useful to fabricate non volatile digital circuits which might revolutionize the area of communication and computing. For Mn:ZnO samples the magnetism disappeared beyond 20 at.% Mn incorporation.

4.5 Bibliography

[1]. C. Jagadish, and S. J. Pearton, Zinc Oxide Bulk, Thin Films and Nanostructures: Processing, Properties and Applications (Elsevier, New York, 2006).

[2]. T. Dietl, H. Ohno, F. Matsukura, J. Cibert, and D. Ferrand, Science 287 (2000) 1019.

[3]. T. Dietl, Nat. Mater 9 (2010) 965.

[4]. P. Sharma, A. Gupta, K. V. Rao, F. J. Owens, R. Sharma, R. Ahuja, J. M. O. Guillen, B. Johansson, and G. A. Gehring, Nat. Mater. 2 (2003) 673.

[5]. J. R. Neal, A. J. Behan, R. M. Ibrahim, H. J. Blythe, M. Ziese, A. M. Fox, and G. A. Gehring, Phys. Rev. Lett. 96 (2006) 197208.

[6]. Q. Wang, Q. Sun, G. Chen, Y. Kawazoe, and P. Jena, Phys. Rev. B 77 (2008) 205411.

[7]. M. Khalid, M. Ziese, A. Setzer, P. Esquinazi, M. Lorenz, H. Hochmuth, M. Grundmann, D. Spemann, T. Butz, G. Brauer, W. Anwand, G. Fischer, W. A. Adeagbo, W. Hergert, and A. Ernst, Phys. Rev. B 80 (2009) 035331.

[8]. S. Mal, S. Nori, C. Jin, J. Narayan, S. Nellutla, A. I. Smirnov, and J. T. Prater, J. Appl. Phys. 108 (2010) 073510.

[9]. N. H. Hong, J. Sakai, N. Poirot, and V. Brizé, Phys. Rev. B, 73 (2006) 132404.

[10]. J. M. D. Coey, M. Venkatesan, and C. B. Fitzgerald, Nat. Mater. 4 (2005) 173.

[11]. J. M. D. Coey, P. Stamenov, R. D. Gunning, M. Venkatesan, and K. Paul, New J. Phys. 12 (2010) 053025.

[12]. J. H. Park, M. G. Kim, H. M. Jang, S. Ryu, and Y. M. Kim, Appl. Phys. Lett. 84 (2004) 1338.

[13]. P. Bobadova-Parvanova, K. A. Jackson, S. Srinivas and M. Horoi, J. Chem. Phys. 122 (2005) 014310.

[14]. M. A. Garcia, E. F. Pinel, J. D. L. Venta, A. Quesada, V. Bouzas, J. F. Fernández, J. J. Romero, M. S. M. González, and J. L. Costa-Krämer, J. Appl. Phys. 105 (2009) 013925.

[15]. C. B. Fitzgerald, M. Venkatesan, J. G. Lunney, L. S. Dorneles, and J. M. D. Coey, Appl. Surf. Sci. 247 (2005) 493.

[16]. K. Ueda, H. Tabata, and T. Kawai, Appl. Phys. Lett. 79 (2001) 988.

[17]. M. Ivill, S. J. Pearton, S. Rawal, L. Leu, P. Sadik, R. Das, A. F. Hebard, M. Chisholm, J. D. Budai, and D. P. Norton, New J. Phys. 10 (2008) 065002.

[18]. V. Jayaram, and B. S. Rani, Mater. Sci.Eng. A 304-306 (2001) 800.

[19]. S. K. Mandal, A. K. Das, T. K. Nath, and D. Karmakar, Appl. Phys. Lett. 89 (2006) 144105.

[20]. M. A. García, F. Jiménez-Villacorta, A. Quesada, J. D. L. Venta, N. Carmona, I. Lorite, J. Llopis, and J. F. Fernández, J. Appl. Phys. 107 (2010) 043906.

[21]. J. H. Kim, H. Kim, D. Kim, Y. E. Ihm, and W. K. Choo, J. Appl. Phys. **92 (**2002**)** 6066.

[22]. G. Gu, G. Xiang, J. Luo, H. Ren, M. Lan, D. He, and X. Zhang, J. Appl. Phys. 112 **(**2012**)** 023913.

[23]. T. Chanier, M. Sargolzaei, I. Opahle, R. Hayn, and K. Koepernik, Phys. Rev. B 73 **(**2006**)** 134418.

[24]. L. Li, Y. Guo, X. Y. Cui, R. Zheng, K. Ohtani, C. Kong, A. V. Ceguerra, M. P. Moody, J. D. Ye, H. H. Tan, C. Jagadish, H. Liu, C. Stampfl, H. Ohno, S. P. Ringer, and F. Matsukura, Phys. Rev. B 85 **(**2012**)** 174430.

[25]. C. N. R. Rao, and F. L. Deepak, J. Mater. Chem. 15 **(**2005**)** 573.

[26]. C. Song, K. W. Geng, F. Zeng, X. B. Wang, Y. X. Shen, F. Pan, Y. N. Xie, T. Liu, H. T. Zhou, and Z. Fan, Phys. Rev. B 73 **(**2006**)** 024405.

[27]. A. Zukova, A. Teiserskis, S. V. Dijken, Y. K. Gun'ko, and V. Kazlauskiene, Appl. Phys. Lett. 89 **(**2006**)** 232503.

[28]. M. Venkatesan, C. B. Fitzgerald, J. G. Lunney, and J. M. D. Coey, Phys. Rev. Lett. 93 **(**2004**)** 177206.

[29]. P. Sati, R. Hayn, R. Kuzian, S. Régnier, S. Schäfer, A. Stepanov, C. Morhain, C. Deparis, M. Laügt, M. Goiran, and Z. Golacki, Phys. Rev. Lett. 96 **(**2006**)** 017203.

[30]. P. Sharma, A. Gupta, K. V. Rao, F. J. Owens, R Sharma, R Ahuja, J. M. O. Guilen, B. Johansson, and G. A. Gehring, Nat. Mater. 2 **(**2003**)** 673.

[31]. T. Fukumura, Z. Kin, A. Ohtomo, H. Koinuma, and M. Kawasaki, Appl. Phys. Lett. 75 **(**1999**)** 3366.

[32]. T. Fukumura, Z. Jin, M. Kawasaki, T. Shono, T. Hasegawa, S. Koshihara, and H. Koinuma, Appl. Phys. Lett. 78 **(**2001**)** 959.

[33]. B. Straumal, B. Baretzky, A. Mazilkin, S. Protasova, A. Myatiev, and P. J. Straumal, Euro. Ceramic Society 29 **(**2009**)** 1963.

[34]. X. Z. Li, J. Zhang, and D. J. Sellmyer, Solid State Comm. 141 **(**2007**)** 398.

[35]. J. Jin, X. Y. Zhang, Y. X. Zhou, and G. S. Chang, Semicond. Sci. Technol. 27 **(**2012**)** 035012.

[36]. S. Kolesnik, and B. Dabrowski, J. Appl. Phys. 96 **(**2004**)** 5379.

[37]. S. Lee, H. S. Lee, S. J. Hwang, Y. Shon, D. Y. Kim, and E. K. Kim, J. Cryst. Growth 286 **(**2006**)** 223.

[38]. X. M. Cheng, and C. L. Chien, J. Appl. Phys. 93 **(**2003**)** 7876.

[39]. Q. Xu, H. Schmidt, L. Hartmann, H. Hochmuth, M. Lorenz, A. Setzer, P. Esquinazi, C. Meinecke, and M. Grundmann, Appl. Phys. Lett. 91 **(**2007**)** 092503.

[40]. D. C. Kundaliya, S. B. Ogale, S. E. Lofland, S. Dhar, C. J. Metting, S. R. Shinde, Z. Ma, B. Varughese, K. V. Ramanujachary, L. Salamanch-Riba, and T. Venkatesan, Nat. Mater. 3 **(**2004**)** 709.

[41]. D. Iuşan, B. Sanyal, and O. Eriksson, Phys. Rev. B 74 **(**2006**)** 235208.

[42]. D. S. Negi, B. Loukya, K. Dileep, M. Kesaria, N. Kumar, and R. Datta, Superlatt. Microstruct. 63 (2013) 289.

[43]. B. Loukya, D. S. Negi, K. Dileep, N. Kumar, J. Ghatak, and R. Datta, J. Magn. Magn. Mater. 345 (2013) 159.

[44]. P. Vénneguès, B. Beamont, S. Haffouz, M. Vaille, and P. Gibart, J. Cryst. Growth 187 (1998)167.

[45]. E. Frayssinet, B. Beamont, J. P. Faurie, P. Gibart, Z. Makkai, B. Pécz, P. Lefebvre, and P.Valvin, MRS Internet J. Nitride Semicond. Res. 7 (2002) 8.

[46]. R. Datta, M. J. Kappers, M. E. Vickers, J. S. Barnard, and C. J. Humphreys, Superlatt. Microstruc. 36 (2004) 393.

[47]. R. Datta, M. J. Kappers, J. S. Barnard, and C. J. Humphreys, Mater. Res. Soc. Symp. Proc. 831 (2004) E 8.8.

[48]. M. J. Kappers, R. Datta, R. A. Oliver, F. D. G. Rayment, M. E. Vickers, and C. J. Humphreys, J. Cryst. Growth 300 (2007) 70.

[49]. O. Maksimov, Rev. Adv. Mater. Sci. 24 (2010) 26.

[50]. V. Avrutin, D. J. Silversmith, H. Morkoc, Proc. IEEE 98 (2010) 1269.

[51]. G. Brauer, J. Kuriplach, C. C. Ling, and A. B. Djurisic, J. Phys.: Conf. Ser. 265 (2011) 012002.

[52]. M. K. Yadav, M. Ghosh, R. Biswas, A. K. Raychaudhuri, A. Mookerjee, and S. Datta, Phys. Rev. B 76 (2007) 195450.

[53]. P. Pant, J. D. Budai, R. Aggarwal, R. J. Narayan, and J. Narayan, J. Phys. D: Appl. Phys. 42 (2009) 105409.

[54]. E. M. Kaidashev, M. Lorenz, H. von Wenckstern, A. Rahm, H.-C. Semmelhack, K.-H. Han, G. Benndorf, C. Bundesmann, H. Hochmuth, and M. Grundmann, Appl. Phys. Lett. 82 (2003) 3901.

[55]. A. Janotti, and C. G Van de Walle, Rep. Prog. Phys. 72 (2009) 126501.

[56]. N. H. Nickel, and E. Terukov, Zinc Oxide - A Material for Micro- and Optoelectronic Applications (Springer, New York, 2004).

[57]. G. Koster, A. J. H. M. Rijnders, D. H. A. Blank, and H. Rogalla, Mater. Res. Soc. Symp. Proc. 526 (1998) 33.

[58]. G. Koster, G. J. H. M. Rijnders, D. H. A. Blank, and H. Rogalla, Appl. Phys. Lett. 74 (1999) 3729.

[59]. B. Loukya, P. Sowjanya, K. Dileep, R. Shipra, S. Kanuri, L. S. Panchakarla, and R. Datta, J. Cryst. Growth, 329 (2011) 20.

[60]. W. G. Waddington, P. Rez, I. P. Grant, and C. J. Humphreys, Phys. Rev. B 34 (1986) 1467.

[61]. L. Laffont, and P. Gibot, Material Characterization 61 (2010) 1268.

[62]. B. Gilbert, B. H. Frazer, A. Belz, P. G. Conrad, K. H. Nealson, D. Haskel, J. C. Lang, G. Srajer, and G. D. Stasio, J. Phys. Chem. A 107 (2003) 2839.

[63]. H. Kurata, and C. Colliex, Phys. Rev. B 48 (1993) 2102.

[64]. H. Tan, J. Verbeeck, A. Abakumov, and G. Van Tendeloo, Ultramicroscopy 116 (2012) 24.

[65]. M. Kobayashi, Y. Ishida, J. I. Hwang, T. Mizokawa, A. Fujimori, K. Mamiya, J. Okamoto, Y. Takeda, T. Okane, Y. Saitoh, Y. Muramatsu, A. Tanaka, H. Saeki, H. Tabata, and T. Kawai, Phys. Rev. B 72 (2005) 201201(R).

[66]. S. C. Wi, J. -S. Kang, J. H. Kim, S. -B. Cho, B. J. Kim, S. Yoon, B. J. Suh, S. W. Han, K. H. Kim, K. J. Kim, B. S. Kim, H. J. Song, H. J. Shin, J. H. Shim, and B. I. Min, Appl. Phys. Lett. 84 (2004) 4233.

[67]. M. Fonin, G. Mayer, E. Biegger, N. Janßen, M. Beyer, T. Thomay, R. Bratschitsch, Y. S. Dedkov, and U. Rüdiger, J. Phys.: Conference Series 100 (2008) 042034.

[68]. M. S. Moreno, T. Kasama, R. E. Dunin-Borowski, D. Cooper, P. A. Midgley, L. B. Steren, S. Duhalde, and M. F. Vignolo, J. Phys. D: Appl. Phys. 39 (2006) 1739.

[69]. Wang Z L, Yin J S, and Jiang Y D 2000 Micron 31 (2000) 571.

[70]. W. G. Waddington, P. Rez, I. P. Grant, and C. J. Humphreys, Phys. Rev. B 34 (1986) 1467.

[71]. A. Sundaresan, R. Bhargavi, N. Rangarajan, U. Siddesh, C. N. R. Rao, Phys. Rev. B, 74 (2006) 161306.

[72]. J.C.A. Huang, H.S. Hsu, Y.M. Hu, C.H. Lee, Y.H. Huang, M.Z. Lin, Applied Physics Letters 85 (2004) 3815.

[73]. P.A. Joy, P.S.A. Kumar, S.K. Date, Journal of Physics: Condensed Matter 10 (1998) 11049.

[74]. A. Janotti, C.G.V. Walle, Report on Progress in Physics 72 (2009) 126501.

Chapter 5

Origin of Magnetism in Co:ZnO Thin Films

This chapter discusses on the possible origin of magnetism and coercivity in Co:ZnO epitaxial thin films grown by Pulsed Laser Deposition. The observed magnetism is explained based on experimental EMCD results and density functional theory based calculations.

Part of this work has been published in Journal of Magnetism and Magnetic Materials, 325 (2013) 159. Copyright (2013) by Elsevier.

5.1 Introduction

As discussed in Chapter 4, though observation of room temperature ferromagnetism was reported in transition metal (TM) doped/undoped ZnO and several theories are proposed to explain the observed magnetism, the subject remained highly controversial. It has now been widely accepted that the atomic defects play a significant role in the observation of magnetism in these systems. Though there are several theories proposed to explain the magnetism in this system, defect based models are found to be more convincing, Among them, the Bound Magnetic Polaron (BMP) and Charge Transfer Ferromagnetism models proposed by J. M. D. Coey *et al.* are widely accepted [1,2]. Within the BMP model, the interaction between oxygen point defects and TM impurities form bound magnetic polaron (BMP) which mediate large scale ferromagnetism in this system. In the charge transfer model transition metal ions transfer electronic charges to the defect band help in spin splinting and weak itinerant ferromagnetism. In general, it is observed that the ferromagnetic hysteresis loop width or coercivity is narrow and magnetism is generally soft in this system except in a few cases where authors did not discuss this aspect [3,4].

In this Chapter, possible explanation for the origin of composition dependent large coercivity (~ 1149 Oe) in Co doped ferromagnetic ZnO thin films which might open up possible applications in novel computer logic systems is discussed. This enhancement in coercivity without significantly altering saturation magnetization also demonstrates the clear interaction between itinerant carriers at defect band with localized *d* electrons in TM-doped ZnO to some extent. This interaction is explained by charge transfer from Co *d* electronic state to defect levels as confirmed from Co $L_{3,2}$ white line ratio.

5.2 Magnetization Measurements: Giant Coercivity in Co doped ZnO Thin Films

The most interesting aspect of Co:ZnO sytem in our study is the composition dependent coercivity and we observed highest coercivity for 25% Co:ZnO system [5]. Magnetic hysteresis study was performed at room temperature in a superconducting quantum interference device (SQUID) Quantum Design, USA. The saturation magnetic moment we see is extremely weak (3.6 emu/cm^3 for 25% Co:ZnO) even for ZnO without any Co (39 emu/cm^3) in it and is the response of net charge carriers from spin split up and down defect band. The magnetism is soft (but not negligible) because free carriers or conduction electrons are not bound to the lattice

rigidly or there is no significant influence of crystallographic anisotropic energy on these defect band carriers. However, we see increase in coercivity (anisotropy) and remnant magnetization with the increase in Co doping from 10% and reaches maximum at 25% doping concentrations. The coercivity reaches ~860 Oe for 25 at.% Co:ZnO and increase further to 1149 Oe when field is switched along *c* direction of thin film as shown in Fig. 5.1. This value of 1149 Oe is the highest among any coercivity reported in this system. The applied field required to saturate moments along *c* direction is 1864 Oe compared to 1262 Oe along in plane direction. Remnant magnetization is ~2.14 emu/cm^3 for this sample and 39.13 emu/cm^3 for 20 at. % Co:ZnO sample. This value is much higher than that required for magnetic memory applications.

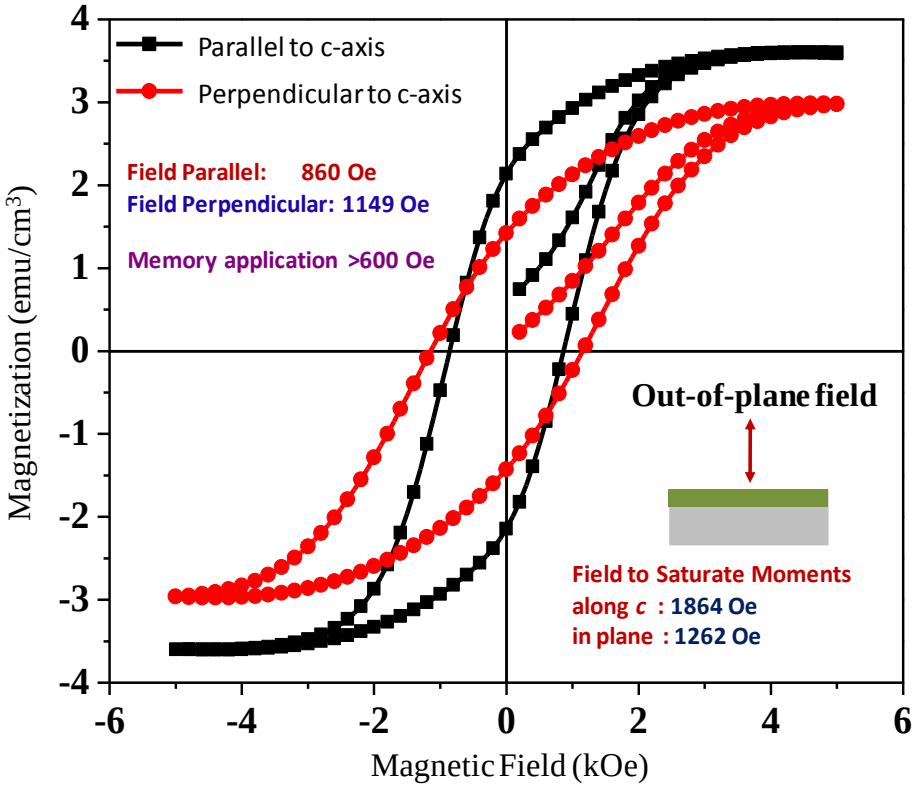

Figure 5.1. Magnetic hysteresis plots for 25Co:ZnO sample showing maximum coercivity ~860 Oe. For the applied field perpendicular to c-direction, the coercivity increases to ~1149 Oe. Copyright (2013) by Elsevier [5].

5.3 Origin of Magnetism: Possible Explanation

Single ion anisotropy of Co atom (in a paramagnetic state) in ZnO (doped with very small amount of Co, ~ 0.005 at. %) due to the crystal field of wurtzite ZnO lattice is already

reported [6]. This aspect has been discussed in the case of Nd doped ZnO nanowires [7], where observation of giant anisotropy has been ascribed to the orbital anisotropy of Nd atoms. The commonly encountered soft nature in hysteresis was explained in terms of origin of moments at the crystal defects, boundaries, and interfaces etc., where spin-orbit coupling is weak and local magneto-crystalline anisotropy at individual defect environment cancels out at macroscopic scale. These moments at defects align under the applied magnetic field, but can easily switch their direction without experiencing any resistance from the host lattice [2]. Once the magnetic field is removed, the residual magnetization observed in this system is negligible. In the applications related to non-volatile digital circuits [8], it will be useful to retain the magnetization in the system even after the removal of the field or in other words, increasing the coercivity of the material by anchoring the moments in the host lattice. The composition dependent large coercivity (~ 1149 Oe) in Co doped ferromagnetic ZnO thin films might open up possible applications in novel computer logic systems. This enhancement in coercivity without significantly altering saturation magnetization also demonstrates the clear interaction between itinerant carriers at defect band with localized *d* electrons in TM-doped ZnO to some extent. This interaction is explained by charge transfer from Co *d* electronic state to defect levels as confirmed from Co $L_{3,2}$ white line ratio. Cathodoluminescence (CL) spectra from different samples shows clear blue emission peak with long tail confirming the formation of extended defect levels in the host lattice band gap.

Another support that the magnetism is now connected with lattice through Co impurity sites is that coercivity increases along *c* (hard axis for *hcp* structure) direction compared to *a* (easy axis for *hcp* structure) direction. The increase in coercivity in not systematic with increasing Co concentrations, e.g., for 10% Co it is higher (730 Oe) than 15 and 20% Co and for 30% Co film it is small (281 Oe). This may be because of distribution of Co atoms and their proximity with a certain type of defects in the lattice. A Co atom *d* level undergoes splitting (e_g and t_{2g}) around the band gap of ZnO host lattice due to tetrahedral crystal field and gives rise to well known green coloration. The t_{2g} level lies higher in the energy scale with three electrons of similar spin states and may be responsible for interaction between *d* electrons of Co atoms and conduction band electrons of ZnO via charge transfer [5].

5.3.1 Emission Band and Defect Related States at the Fermi Level

Cathodoluminescence (CL) measurements were done using Gatan mono CL (serial mode) in FEI quanta 3D FE-SEM with 20 keV electron beam. All spectra have been collected with peltier cooled (-25 ºC) Photo multiplier tube (PMT) with step of 1 nm and accusation time of 0.6 s per step. Entrance and exit slit for the spectrometer were at 1 mm. CL spectra from different samples shows clear blue emission peak with long tail confirming the formation of extended defect levels in the host lattice band gap.

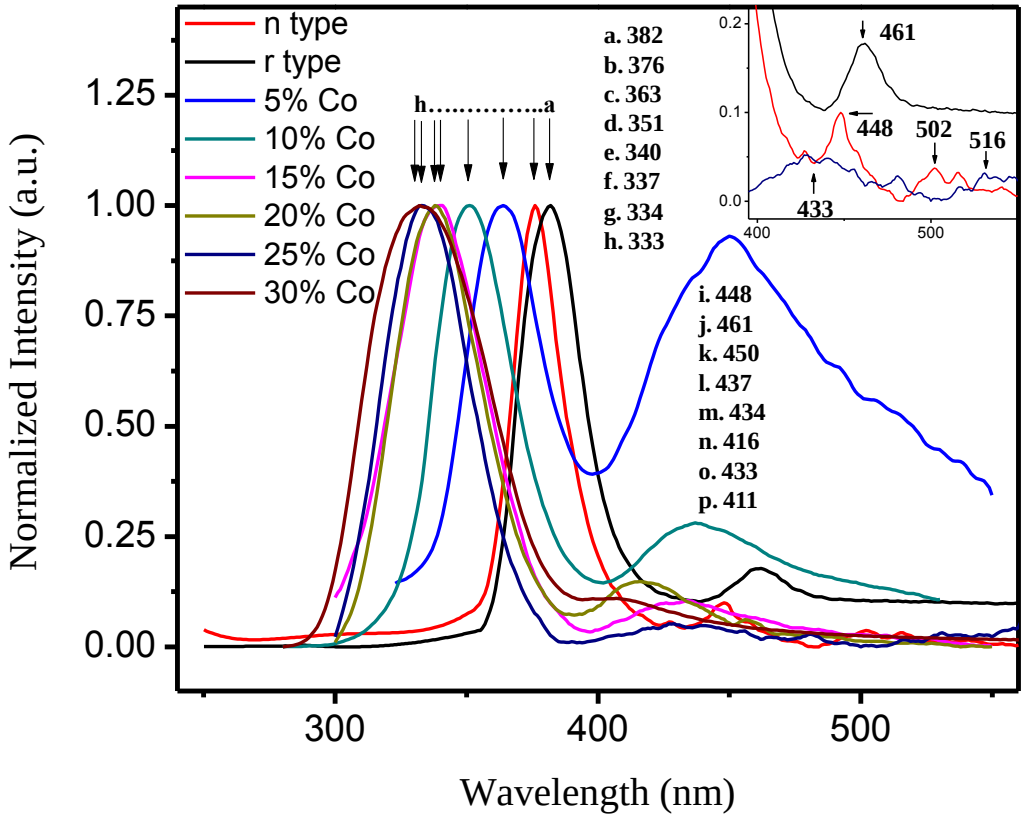

Figure 5.2. CL data for various Co:ZnO and undoped samples. Co:ZnO samples show increase in band gap with strong blue emission peak with extended tail towards green region. For undoped samples, both blue and green emissions are observed for n-type sample and obly blue emission for r-type sample. Copyright (2013) by Elsevier [5].

Figure 5.2 shows the room temperature cathodoluminesce (CL) data from various Co:ZnO films. It is clear that the band gap values increases with Co doping as already reported in various publications [9]. Though we are identifying each sample with targeted Co concentration,

however, the actual composition for each film can be found from Table 4.2 (column 7). The composition difference between targeted and resulting film is due to the dependency of Co atom incorporation on thin film growth condition. For 30Co:ZnO band gap value is 333 nm and this gradual increase in band gap is due to the increase in binding energy of O 2*p* valence band peak through *p*-*d* and *s*-*d* exchange with Co *d* electrons [9]. CL spectra for *n*-type sample shows emission peak at 382 nm compared to 376 nm for *r*-type sample. *n*-type samples shows both blue and green emission peaks around 450 nm and 502 nm which have been ascribed to extended or doubly ionized zinc interstitial (Zn_i) and vacancy oxygen (V_O) states in the ZnO band gap respectively (inset Fig. 4.18). It has already been shown that under certain annealing condition both type of defects can coexist in the structure [10,11]. For *r*-type sample green emission is completely quenched and only blue emission peak is observed. This may be because of higher oxygen partial pressure during film growth. For Co:ZnO films only blue emission peak is observed. Blue emission peak is observed to be decreasing in intensity and shifting towards smaller wavelength with increasing Co incorporation except 25 Co:ZnO sample. From both temperature dependent magnetic data and CL emission peaks, it is clear that Co:ZnO samples have defect levels in the band gap in addition to the usual exciton emission peak across the band gap.

The most surprising aspect in the magnetism of ZnO is to observe ferromagnetism even without transition metal doping. Another noticeable point is that the saturation magnetization does not improve significantly with various condition of film growth and with doping concentration. This strongly suggests that the Co *d* electrons remain localized and the magnetism observed in this system is itinerant in character. This band magnetism has the origin at either Zn_i or oxygen defect band (for Co:ZnO samples, CL spectra of blue emission has a broad tail extending to the green region) and charge transfer occurs from donor defects. The defect band originating from Zn_i or oxygen vacancies (V_O) can be spin split according to Stoner's criteria $I N_{\uparrow,\downarrow}(\varepsilon_F) > 1$, where I is the Stoner's parameter and $N_{\uparrow,\downarrow}(\varepsilon_F) = D(\varepsilon_F)/2n$, density of states (DOS) per atom for each spin state [12,13].

We performed Density Functional Theory (DFT) calculations in Wien2k to plot the density of states at the Fermi level for the case of pure ZnO, Co doped ZnO with 6.25 % and 25% O Vacancy. The calculation is performed using Wien2k code which is based on a self-

consistent scheme by solving Kohn-Sham equations using Full Potential Linearized Augmented Plane Wave (FP-LAPW) method within Generalized Gradient Approximation (GGA) [14]. A super cell of 32 atoms (2×2×2) that allows us to create a maximum V_O or Zn_i (at the octahedral interstices) defect density of 6.25% is considered and the structure is relaxed. This concentration of defect is not realistic and actual concentration corresponding to carrier density i.e. 0.01 % (~10^{19} cm^{-3}) requires consideration of very large supercell with extremely large computational time. The self-consistent calculations of the system are converged to an energy less than 10^{-4} Ry. A dense K-mesh of 1000 points is used to calculate the density of states of the relaxed structure. Tetrahedral method is used for the Brillouin Zone integration. DFT calculation does not predict magnetization due to either V_O or Zn_i. In order to calculate the exact excited state properties and correct for the band gap, 'modified Becke-Johnson' exchange correlation potential (mBJLDA) has been used [15-17] and is also discussed in Chapter 3.3.

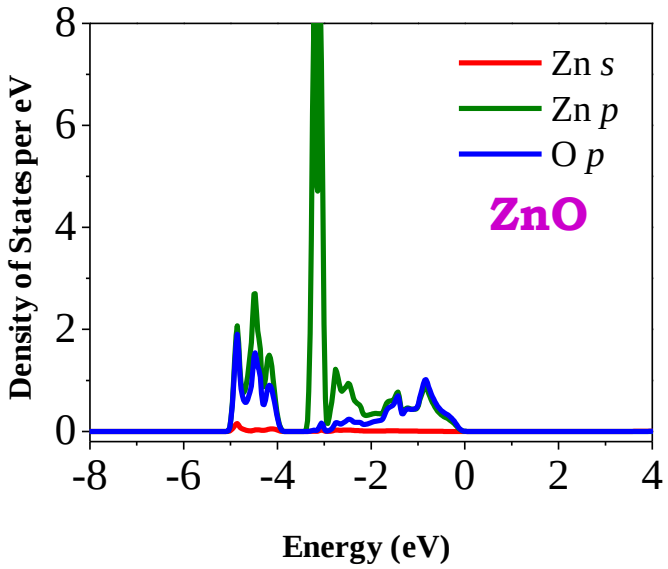

Figure 5.3. Calculated density of states for the case of pure ZnO showing the Zn p and O p states. For pure ZnO case, we do not observe any appreciable density of states due to Zn p or O p at the Fermi level.

Figure 5.3 shows the density of states plot for pure ZnO plotted for comparison with Co doped ZnO with and without V_o cases as shown in Fig. 5.4. We find that the density of states due to the dopant Co atoms i.e., Co *d* and states due to the V_o, i.e., O *p* are increasing with the defect and dopant concentration while Zn *d* and Zn *s* were suppressed and negligible at the Fermi level. The Co *d* and O *p* states are appearing the same energy range near the Fermi level and this

indicates the possible interaction between the two states. We also found that the defect band at the Fermi level is spin split according to the Stoner Criterion [13] making makes $I\,N_{\uparrow,\downarrow}(\varepsilon_F) > 1$. This has been verified for the cases of both oxygen vacancy and Zn interstitial [5].

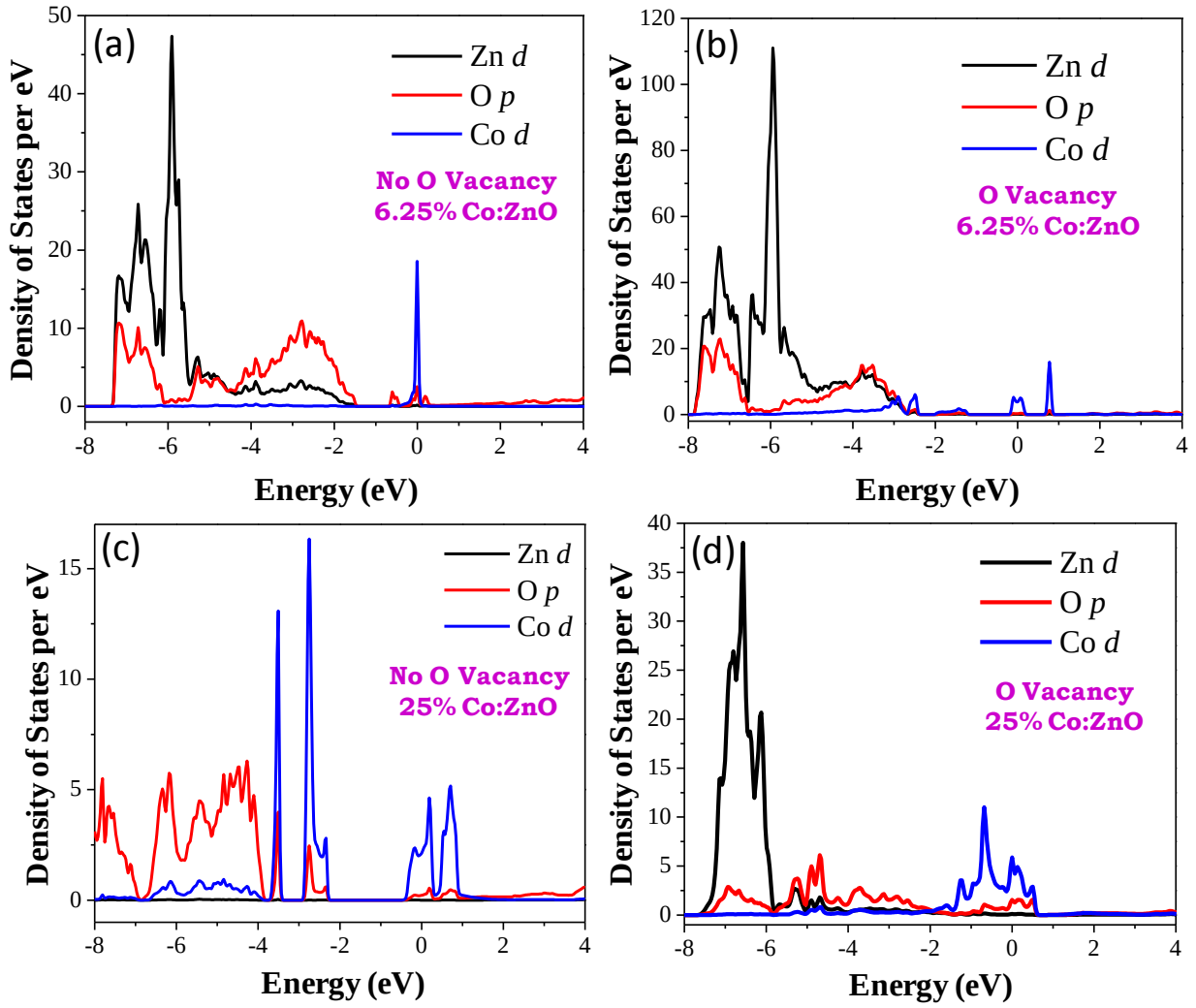

Figure 5.4. Calculated denstiy of states for the case of (a) 6.25 % Co doping without oxygen vacancy, (b) 6.25 % Co doping with oxygen vacancy, (c) 25 % Co doping without oxygen vacancy and (d) 25 % Co doping with oxygen vacancy in ZnO. We observe the appearance of Co d and O p states due to the dopant and defects respectively, occurring at the same energy range around the Fermi level indicating the possible interaction between the two states that results in the experimentally observed ferromagnetism and coercivity in these systems. Moreover, the density of Co d and O p states at the Fermi level increases with the dopant and defect concentrations in the lattice.

Under this scenario only small fraction of carriers will be with one type of spin and with increasing number of carrier concentration both types of spins will start filling bands and there would not be any significant increase in magnetism as opposite spins will cancel each other's moments. This notion has already been used by Coey *et al.* to explain defect band magnetism in oxides doped with mixed valence TM impurities which serves as charge reservoir [2]. Bound magnetic polaron model (BMP) is not operative otherwise the saturation moment would have been very high (column 3, Table 4.2 except 20Co:ZnO sample) had TM impurities been aligned through interaction with hydrogenic orbital formed due to V_O or Zn_i. Presence of carriers cannot be ruled out even in resistive ZnO samples due to spontaneous formation of defects depending on Fermi level [18].

5.3.2 Charge Transfer Ferromagnetism: Co *d* and Defect Band Interaction

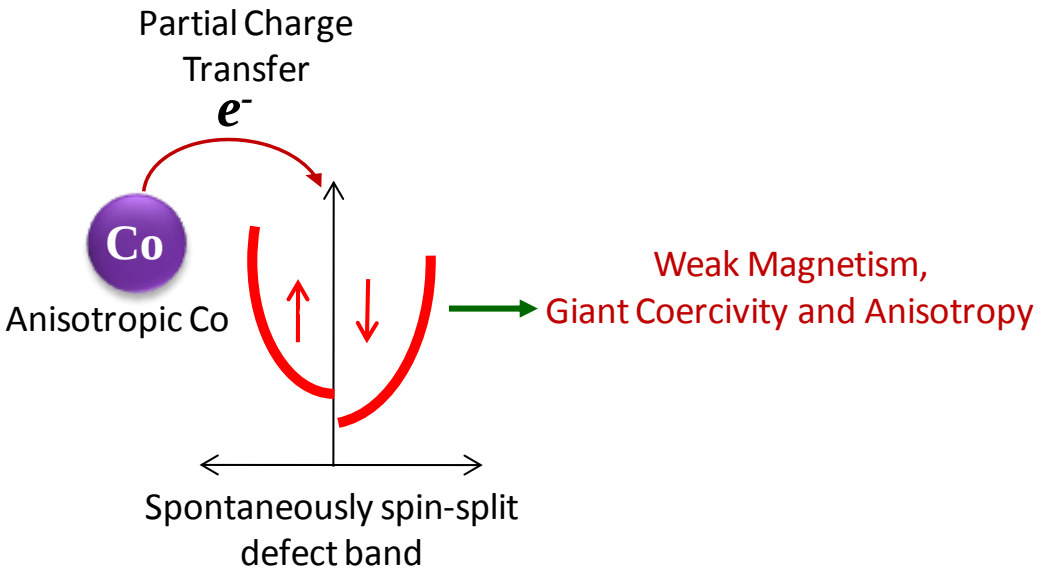

Figure 5.5. Schematic drawn to explain the origin of weak ferromagnetism and giant coercivity in 25% Co:ZnO. This is showing the partial charge transfer from anisotropic Co d to the spin-split defect band resulting in magneto-crystalline anisotropy and coercivity.

This increase in coercivity is explained by the establishment of interaction between defect band conduction electrons and localized *d* electrons of Co atoms to some extent. This may be quite possible as the charge state of Co is found to be close to +3 from Co $L_{3,2}$ white line ratio (see Chapter 4.3.2), suggesting that charge transfer has taken place to some band possibly to the

defect band formed by both V_O and Zn_i. Delocalized band electrons may be formed due to oxygen vacancies (V_O) or Zn interstitials (Zn_i) in the lattice and are responsible for the *n*-type conduction in our films. CL data is clearly supporting the formation of such defect states. Density of states due to Zn_i donor defects (or V_O) satisfy Stoner's criteria and cause defect band to be spin split. As single Co atom in ZnO show large anisotropy, thus this interaction may be responsible for the observed large coercivity in our samples [6]. Fig. 5.5 is the schematic drawn to explain the weak ferromagnetism and large anisotropic coercivity in this system. The partial charge transfer by the anisotropic Co *d* to the spin-split defect band (according to the Stoner Criterion) leads to large anisotropic coercivity and weak ferromagnetism.

5.3.3 Element Specific Magnetism from Co:ZnO by EMCD

Electron Magnetic Circular Dichroism (EMCD) is a tool to probe nanoscale magnetism and this could be an ultimate technique as of now tool to provide evidence on the element specific magnetism in this system. Once can also quantify the magnetic moments. The 25 at.% and 20 at.% Co:ZnO thin films were studied with Electron Magnetic Circular Dichroism (EMCD) as a probe to investigate the origin of magnetism. The experiment is performed with gun monochromator excitation at 300 kV following the procedure as described in Chapter 2. The experimental EMCD spectra are acquired selecting *g*=(0004) and *g*=(11-20) reflections. The energy-filtered diffraction patterns acquired to scan Co $L_{2,3}$ energy range (765-810 eV) are processed using FORTRAN program. The dichroic signal is plotted by taking the difference of the $L_{2,3}$ spectra obtained from the two symmetric positions on the diffraction plane [19].The experimental spectra are background subtracted and peak fitted using Eq. 3.7 using asymmetric Lorentzian and Gaussian functions. There is also a previous report performing the EMCD to illustrate intrinsic ferromagnetism in Co doped ZnO nanostructures [20]. We could obtain a clear and weak magnetic dichroic signal from both the films as shown in Fig. 5.6, indicating that the Co atom is indeed weakly magnetic in this system due to charge transfer to the defect band. Further work need to be done in quantifying the moments to compare with the resultant total magnetization from these samples.

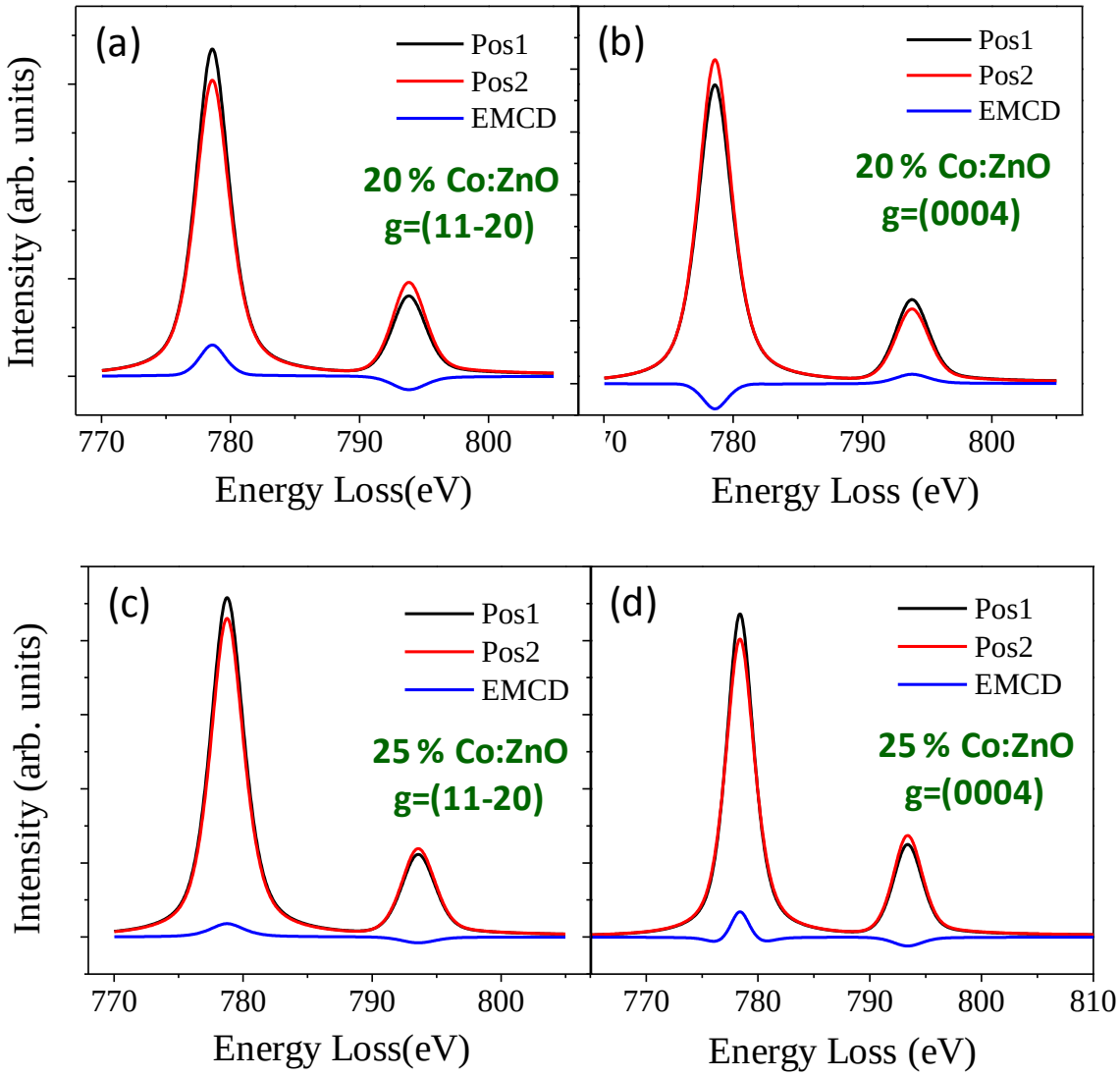

Figure 5.6. Co $L_{2,3}$ EMCD spectra obtained from 20 % and 25 % Co doped ZnO thin films for two different excitations. The film is tilted to excite g=11-20 and g=0004 reflections in the diffraction plane. We observed dichroic signal from both the films indicate that the magnetism in these films has the origin at the Co atom.

5.4 Conclusions

In conclusion, we explained the origin of magnetism and giant coercivity in 25% Co doped ZnO based on the partial charge transfer from the Co *d* to the spontaneously spin-split defect band resulting in the magneto-crystalline anisotropy due to the Co atom in the lattice. The splitting of Co *d* electron level and their interactions with defect band electrons results in high

coercivity. Element specific EMCD at Co $L_{2,3}$ reveals weak ferromagnetism at the Co atom supporting our view on the charge transfer from Co atom to the defect band and the interaction between them. Density functional theory based calculations shows the Co *d* states and defect band states overlapping at the Fermi level indicating the possible interaction via charge transfer and also these states increases with the increase in the Co and defect concentration in the system.

5.5 Bibliography

[1]. J. M. D. Coey, M. Venkatesan, and C. B. Fitzgerald, Nature Materials, 4 (2005) 175.

[2]. J. M. D. Coey, P. Stamenov, R. D. Gunning, M. Venkatesan, and K. Paul, New Journal Physics, 12 (2010) 053025.

[3]. J. H. Park, M. G. Kim, H. M. Jang, and S. Ryu, Applied Physics Letters, 84 (2004) 1338.

[4]. X. Su, L. Wang, J. Chen, X. Wan, X. P. Zhang, and R. P. Wang, Journal of Physiccs D: Applied Physics, 44 (2011) 265002.

[5]. B. Loukya, D. S. Negi, K. Dileep, N. Kumar, J. Ghatak, and R. Datta, J. Magn. Magn. Mater. 345 (2013) 159.

[6]. P. Sati, R. Hayn, R. Kuzian, S. Régnier, S. Schäfer, A. Stepanov, C. Morhain, C. Deparis, M. Laügt, M. Gorian, and Z. Golacki, Physical Review Letters, 96 (2006) 017203.

[7]. D. Wang, Q. Chen, G. Xing, J. Yi, S. R. Bakaul, J. Ding, J. Wang, and T. Wu, Nano Letters, 12 (2012) 3994.

[8]. K. Ando, Science, 312 (2006) 1883.

[9]. S. J. Gilliland, J.A. Sans, J. F. S. Royo, G. Almonacid, B. G. Domene, A. Segura, G. Tobias, and E. Canadell, Physical Review B, 86 (2012) 155203.

[10]. H. Zeng, G. Duan, Y. Li, S. Yang, X. Xu, and W. Cai, Advanced Functional Materials, 20 (2010) 561.

[11]. K. Dileep, L. S. Panchakarla, K. Balasubramanian, U. V. Waghmare, and R. Datta, Journal of Applied Physics, 109 (2011) 063523.

[12]. J. M. D. Coey, Magnetism and Magnetic Materials. Cambridge University Press, Cambridge, 2010.

[13]. S. Blundell, Magnetism in Condensed Matter, Oxford University Press, New York, 2001.

[14]. P. Blaha, K. Schwarz, G. K. H. Madsen, D. Kvasnicka, and J. Luitz, WIEN2k, Vienna University of Technology, Vienna, Austria, 2001.

[15]. F. Tran, and P. Blaha, Phys. Rev. Lett. 102 (2009) 226401.

[16]. D. Koller, F. Tran, and P. Blaha, Phys. Rev. B 85 (2012) 155109.

[17]. V. Avrutin, D. J. Silversmisth, and H. Morkoç, Proceedings of IEEE, 98 (2010) 1269.

[18]. B. Loukya, D. S. Negi, K. Dileep, N. Pachauri, A. Gupta, and R. Datta, Phys. Rev. B, 91 (2015) 134412.

[19]. B. Loukya, X. Zhang, A. Gupta, and R. Datta, J. Magn. Magn. Mater. 324 (2012) 3754.

[20]. Z. H. Zhang, X. Wang, J. B. Xu, S. Muller, C. Ronning, and Q. Li, Nat. Nanotech. 4 (2009) 523.

Chapter 6

Conclusions and Future Perspectives

This chapter gives note on the important conclusions drawn from the present thesis along with an overview on the future experimental perspectives and capability of electron magnetic circular dichroism technique in nano and atomic scale magnetic studies.

6.1 Summary of the Thesis

The main aim of this thesis was the experimental application, theoretical understanding and development of Electron Magnetic Circular Dichroism (EMCD) technique in a Transmission Electron Microscope (TEM). We have shown that EMCD is a powerful tool for obtaining quantitative element and site-specific orbital and spin magnetic moment information at nanoscale.

We successfully obtained high signal over noise ratio at nanoscale with gun monochromator excitation from CrO_2 epitaxial thin films by EMCD. Magnetic dichroic signal obtained from <10 nm region in these films prove EMCD as a nanoscale magnetism characterization tool [1]. Quantitative and site-specific magnetic information is obtained from $NiFe_2O_4$ (NFO) and $CoFe_2O_4$ (CFO) epitaxial thin films. '*K*' parameter in the EMCD sum rules is evaluated. We observed that thickness averaged *K* as well as thickness averaged dichroic signal need to be considered for quantitative EMCD analysis which is also the reason for the experimentally observed low dichroic signal. Experimental magnetic dichroic signal is obtained from regular inverse spinel, cation vacancy and cation mixing regions of NFO and CFO. A simple Bloch wave model based on phenomenological absorption is proposed to calculate the site-specific signal contributions to the total signal for the inverse spinel structure [2-5].

Epitaxial thin films of ZnO and Co/Mn alloyed ZnO with varying dopant percentages upto 30 % were grown on *c*- plane sapphire substrate using Pulsed Laser Deposition (PLD) technique. Composition dependent coercivity was observed in Co doped ZnO while the observed magnetism was feeble and soft in the case of Mn doped ZnO. We obtained ~ 860 Oe coercivity for the case of 25 at.% Co:ZnO thin film and this value increased to ~1149 Oe for the applied field along perpendicular to *c*-plane. Co charge state in Co:ZnO was found to be +3 as calculated from the L_3/L_2 white line ratio by electron energy loss spectroscopy. Observed magnetism and giant coercivity in these films are explained based on the partial charge transfer from the Co *d* to the spontaneously spin-split defect band resulting in the magneto-crystalline anisotropy due to the Co atom in the lattice. Density of states calculated using Density Functional Theory showed the increase in the density of Co *d* and O *p* states at the Fermi level with the increase in the oxygen defect concentration indicating the possible interaction between Co *d* and defect band.

Element specific Co $L_{2,3}$ magnetic dichroic signal obtained from Co:ZnO system proves that magnetism in this system is originating from Co atoms [6-8].

6.2 Future: Quantitative Magnetic Information at Atomic Scale

In the recent years, there has been a tremendous development in the field of transmission electron microscopy resulting in various advanced microscopy techniques to be able to provide atomic scale information on the type, position and charge state of atoms [9]. Development of aberration-corrected electron optics in the recent years plays significant role in attaining such atomic scale information. Moreover, working with energy-filtered diffraction patterns measured on core-level edges gives access to a wealth of magnetic information originating from spin moment, orbital moment, spin-orbital interaction, and individual components of magnetic and spin-orbital anisotropy tensors [10]. Electron Microscopes are currently being built with spin polarized electron beams [11]. However, several theoretical approaches were proposed to obtain atomic scale magnetic information and some of them are discussed in the following sections.

6.2.1 Mapping Spin-polarized Transitions at Atomic Scale

The theoretical possibility of mapping spin-polarized chiral transitions on the atomic scale is a crucial question related to EMCD. This would result in a unique method to visualize the change in the angular momentum of single electrons during an electronic transition.

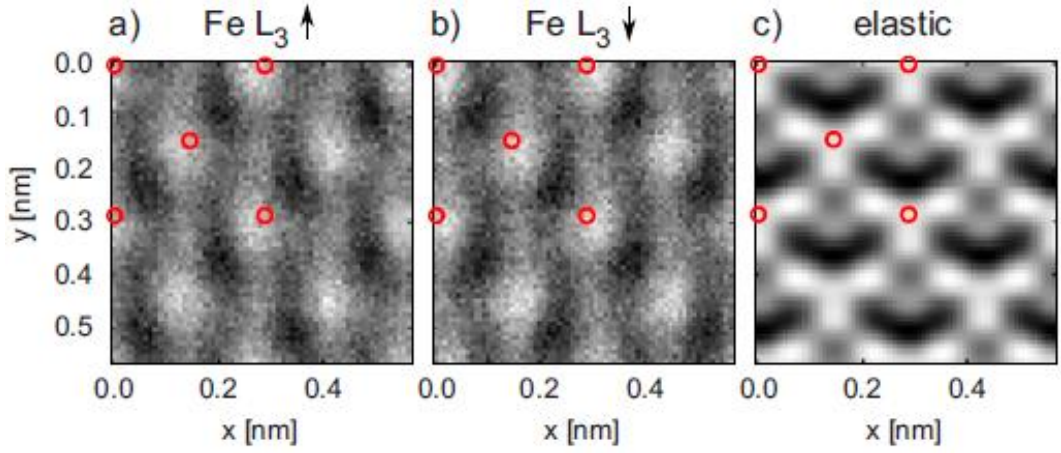

Figure 6.1. Simulated High resolution (EMCD) image of 12 nm thick ferromagnetic bcc Fe L_3 signal along [001] zone axis orientation at 200 kV for complete orbital magnetization in (a) positive and (b) negative zone axis direction. (c) is the elastic image. Red circles denote the atom positions. Copyright (2010) by American Institute of Physics [12].

The dichroic signal is calculated from a single magnetic transition as a function of position of the hypothetical ionized atom in the crystal based on density matrix approach. The total dichroic signal is then calculated by integrating over all possible scattering centers of the specimen to account for the experimental signal [12]. Atomic resolution images of Fe L_3 system with spin magnetic moments are constructed based on the density matrix approach for inelastic electron scattering. The simulated high resolution image shows a shift in the image of ~ 50 pm with respect to the centre of the atom to the left/right indicating an up/down magnetic moment of the atom. C_s should be able to pick up this faint shift. Fig. 6.1 shows the simulated high resolution TEM image considering the experimental parameters that one would easily obtain using an aberration corrected microscope [12-15] showing that in principle it is possible to map individual spins in a ferromagnet by means of a conventional TEM.

6.2.2 EMCD with Vortex Electron Beam

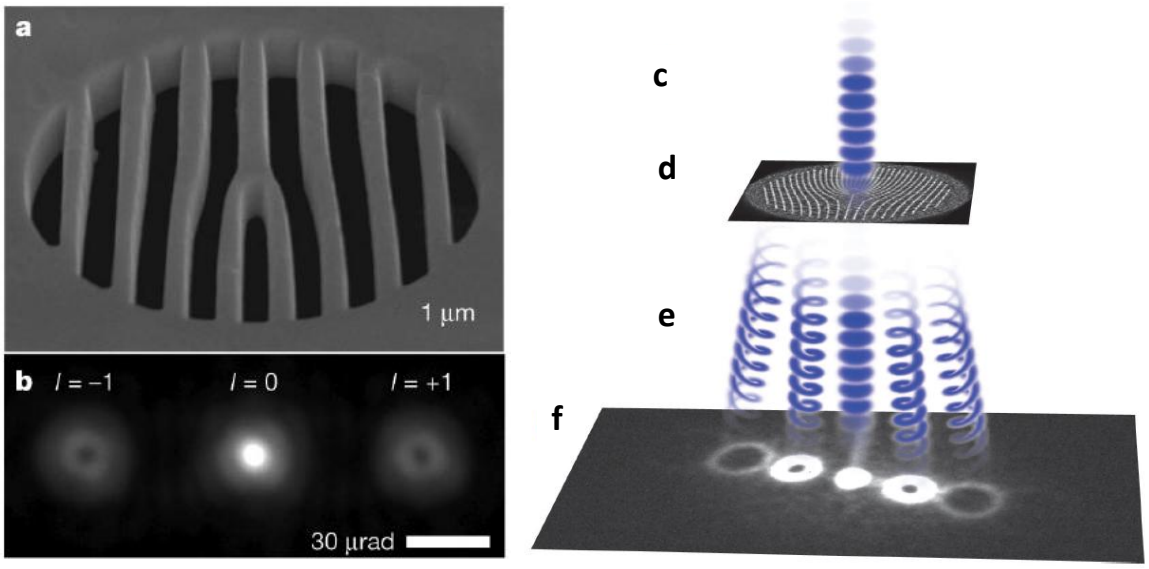

Figure 6.2. (a) Scanning electron microscope image of a dual-beam focused ion beam thinned Pt foil that acts as a phase dislocation aperture. (b) Diffraction pattern of the vortex aperture illuminated with a plane wave of 300 kV. Copyright (2010) by Nature Publishing Group [16]. Formation of electron vortices by a spatially coherent plane wave of electrons (c) illuminates a nanofabricated hologram (d) and then diffracts into multiple electron vortex beams (e) which are then imaged (f) using a CCD (charge-coupled device). The beam cross section shown in (f) is a measured diffracted electron intensity distribution. Copyright (2011) by American Association for the Advancement of Science [17].

Experimental realization of production methods to generate electron vortex beams using nanofabricated diffraction holograms [16-18] started after their first theoretical introduction by Bliokh *et al*. [19]. Fig. 6.2 is showing the scanning electron microscope image of holographic aperture designed on a thinned Pt foil and the schematic of vortex electron beams produced after being the aperture being illuminated by plane wave electron beam at 300 kV. It has been theoretically proposed that such electron vortex beams carrying high angular momentum can detect magnetic dichroic signals indicating their applications in EMCD experiments [20-22]. Indeed it was shown computationally that electron vortex beams carrying a large orbital angular momentum can detect magnetic signal in a scanning mode only at atomic resolution as suggested by selection rules for magnetic quantum number [22,23] and that appreciable EMCD signal can only be detected when vortex beam passes directly through or very close to column of magnetic atoms.

6.2.3 Atomic Scale Magnetic Information by Controlling the Phase Symmetry

The recent report [24] indeed proved theoretically that atomic resolution magnetic dichroism signal can be achieved without the need of electron vortex beams. It is possible to obtain atomic resolution EMCD signal by breaking the symmetry of the electron probe phase distribution using aberration-corrected optics of a scanning transmission electron microscope. Strongly hoping that such theoretical proposals will experimentally be successful and the future magnetic studies would aim at probing magnetic dichroism, optical dichroism, valley polarization etc., with excellent spatial resolution by tailoring electron probe phase distributions. Magnetic thin films and nanostructures have diverse applications ranging from data storage to those related to medical diagnostics and treatment. Therefore experimental realization of theoretical proposals to access atomic scale magnetic information would help in understanding and enhancing the applications of advanced magnetic materials.

6.3 Bibliography

[1]. B. Loukya, X. Zhang, A. Gupta, and R. Datta, J. Magn. Magn. Mater. 324 (2012) 3754.

[2]. R. Datta, S. Kanuri, S. V. Karthik, D. Mazumdar, J. X. Ma, and A. Gupta, Appl. Phys. Lett. 97 (2010) 071907.

[3]. R. Datta, B. Loukya, N. Li, and A. Gupta, J. Cryst. Growth 345 (2012) 44.

[4]. K. Dileep, B. Loukya, N. Pachauri, A. Gupta, and R. Datta, J. Appl. Phys. 116 (2014) 103505.

[5]. B. Loukya, D. S. Negi, K. Dileep, N. Pachauri, A. Gupta, and R. Datta, Phys. Rev. B 91 (2015) 134412.

[6]. B. Loukya, P. Sowjanya, K. Dileep, R. Shipra, S. Kanuri, L. S. Panchakarla, and R. Datta, J. Cryst. Growth 329 (2011) 20.

[7]. B. Loukya, D. S. Negi, K. Dileep, N. Kumar, J. Ghatak, and R. Datta, J. Magn. Magn. Mater. 345 (2013) 159.

[8]. D. S. Negi, B. Loukya, K. Dileep, M. Kesaria, N. Kumar, and R. Datta, Superlatt. and Microstruct. 63 (2013) 289.

[9]. G. Van Tendeloo, S. Bals, S. Van Aert, J. Verbeeck, and D. Van Dyck, Adv. Mater. 24 (2012) 5655.

[10]. J. Rusz, S. Rubino, O. Eriksson, P. M. Oppeneer, and K. Leifer, Phys. Rev. B 84 (2011) 064444.

[11]. M. Kuwahara, Y. Takeda, K. Saitoh, T. Ujihara, H. Asano, T. Nakanishi, and N. Tanaka, J. Phys.: Conf. Ser. 298 (2011) 012016.

[12]. P. Schattschneider, I. Ennen, S. Löffler, M. Stöger-Pollach, and J. Verbeeck, J. Appl. Phys. 107 (2010) 09D311.

[13]. P. Schattschneider, I. Ennen, M. Stöger-Pollah, J. Verbeeck, V. Mauchamp, and M. Jaouen, Ultramicroscopy 110 (2010) 1038.

[14]. P. Schattschneider, J. Verbeeck, V. Mauchamp, M. Jaouen, and A. –L. Hamon, Phys. Rev. B 82 (2010) 144418.

[15]. P. Schattschneider, B. Schaffer, I. Ennen, and J. Verbeeck, Phys. Rev. B 85 (2012) 134422.

[16]. M. Uchida, and A. Tonomura, Nature 464 (2010) 737.

[17]. J. Verbeeck, H. Tian, and P. Schattschneider, Nature 467 (2010) 301.

[18]. B. J. McMorran, A. Agarwal, I. M. Anderson, A. A. Herzing, H. J. Lezec, J. McClelland, and J. Unguris, Science 331 (2011) 192.

[19]. K. Y. Bliokh, Y. P. Bliokh, S. Savel'ev, and F. Nori, Phys. Rev. Lett. 99 (2007) 190404.

[20]. S. Lloyd, M. Babiker, and J. Yunan, Phys. Rev. Lett. 108 (2012) 074802.

[21]. L. Clark, A. Béché, G. Guzzinati, and J. Verbeeck, Phys. Rev. A 89 (2014) 053818.

[22]. J. Rusz, S. Bhowmick, M. Eriksson, and N. Karlsson, Phys. Rev. B 89 (2014) 134428.

[23]. P. Schattschneider, S. Löffler, M. Stöger-Pollach, and J. Verbeeck, Ultramicroscopy 136 (2014) 81.

[24]. J. Rusz, J. Idrobo, and S. Bhowmick, Phys. Rev. Lett. 113 (2014) 145501.